**University of Bath**

**PHD**

**Electrical impedance tomography: algorithms and applications**

Yang, Chuan Li

*Award date:*
2015

*Awarding institution:*
University of Bath

[Link to publication](#)

# Electrical impedance tomography: algorithms and applications

Chuan Li Yang

A thesis submitted for the degree of Doctor of Philosophy

University of Bath

Department of Electrical and Electronic Engineering

September 2014

# Abstract

Electrical impedance tomography (EIT) is an imaging technique for detecting the internal conductivity distribution of an object by voltage measurements taken by an exterior electrode. EIT has been researched in many different application areas in the world as a simpler, cheaper alternative to many other imaging methods. The topic of this PhD study is mainly focused on a number of key developments in both hardware and software implementation. The basic theories of EIT, including forward problem, inverse problem of EIT and the sensor design have been described. Major contributions of the thesis are in computational and experimental aspects of EIT in a wide variety of geometries. A sparse and memory efficient method has been presented to solve large scale 3D EIT problems. A parallel conjugate gradient (PCG) has been applied to demonstrate computational improvements using synthetic and experimental data. 3D EIT has been implemented for planar array geometry for limited access tomography. Furthermore, multiple frequencies with complex conductivity reconstruction are presented and applied to an EIT-based fabric pressure mapping sensor. A comparative study with traditional tank phantom is presented to provide a context for a fabric pressure mapping sensor. As the motivation for different frequency response with different conductivity inclusions, frequency difference EIT has been implemented to overcome problems of time difference EIT.

# Content

# Acknowledgements

# List of Symbols

$\phi$    -   Electric potential

$\phi*$   -   The complex-valued electric potential

$\sigma$   -   The complex conductivity of the medium

$\nabla$   -   Divergence operator

$z_l$   -   The effective contact impedance between the $l^{th}$ electrode and the tissue

$\eta$   -   The outward normal to the surface electrodes

$U$   -   The complex-valued voltage

$I$   -   The complex-valued current

$e_l$   -   The electrode $l$

$\Delta V$   -   The voltage measurement

$J$, $H$ -   The Jacobian matrix

$I$   -   The Identity matrix

$n$   -   Number of electrodes

M   -   Number of measurements

N   -   Number of voxels

$\Gamma$   -   Tikhonov matrix

$\alpha$   -   Regularization parameter

$L$   -   Regularization matrix

$D$   -   Diagonal matrix

# Chapter.1 Introduction

Electrical impedance tomography (EIT) is an imaging technique that provides a tomographic conductivity image of a subject from exterior current-voltage measurement [1]. A typical EIT system is built by connecting a current source and voltage measurement unit and an array of electrodes [2-4]. In an EIT measurement, a set of small signal currents is applied to pair of electrodes, then the resulting voltages are measured. A control computer is used to calculate the conductivity distribution from the voltage measurement and visualize the conductivity image.

EIT is a new and emerging tomographic imaging technique with great potential in many application areas. EIT is geometrically flexible allowing imaging for almost any possible geometry. The spectral information in electrical properties in many applications makes multi-frequency EIT a new frontier for EIT research. This thesis addresses these challenges through computational enhancements and verification through experimental studies. The work involves modelling of multi-frequency EIT and development of sensors and phantoms in a wide range of geometries including circular array, rectangular array, planar array, cylindrical array and thin-plane EIT in a fabric pressure mapping sensor.

## 1.1. Aims and Objectives

This research involves several EIT software and hardware developments, which include multi-frequency imaging for different sensors as well as solving EIT large data processing problems by improving both software and hardware performances. A wide range of EIT geometries are aim to be studied in order to discover potential application areas. Specific targets are set to ensure the research is done smoothly and successfully:

- Research the background and basics of electrical impedance tomography including history, forward problem, inverse problem, etc. Understand the current state of EIT research around the world and investigate the advantages and weaknesses of EIT.

- Characterise experimental EIT data acquisition systems.

- o Redesign multiplexer board for 32 channel EIT system use.

- o Build various types of experimental EIT phantoms (16 electrodes, 32 electrodes, plane array and fabric pressure mapping sensor).

- Develop algorithms that can deal with sparse Jacobian and multiple uses of a computer central processing unit (CPU). These will operate better than the existing programs in terms of computer memory storage and time consumption.

- A subsurface EIT study by using planar array EIT sensors.

- Implement a MATLAB program that can be tested on different types and geometries of fabric sensor. The program needs to be able to reconstruct complex conductivity images.

- Develop a frequency difference algorithm that includes optimising the regularisation parameters and localisation method to improve resolution and reduce computational costs.

The progress takes large amount of effort and time on MATLAB code generating and error solving as well as many laboratory experiments.

## 1.2. Thesis organisation

A general background of EIT is given in the thesis and specific focuses on the objectives of the PhD study are given in other chapters of the thesis.

This chapter presents a general introduction to EIT and the aims and objectives of this PhD research.

The second chapter gives an overall of EIT's background, history and developments.

Chapter 3 explains how EIT hardware works, including the installation of the system and the data acquisition method. Two different EIT systems used throughout the thesis are described in detail. A relative mathematical model of the forward and inverse problem of 3D EIT is introduced. The most commonly used regularization scheme, Tikhonov regularization, is explained.

In Chapter 4, methods of FEM meshing are described. A wide range of EIT phantom fabrications have been made and their performance has been tested using a reconstruction algorithm.

Chapter 5 introduces a reconstruction algorithm called Block-wise CGLS reconstruction using Sparse Jacobian. It overcomes problems such as large computer memory usage in inverse calculations.

Chapter 6 shows an experimental study of subsurface EIT imaging. Simulations are done by using a computer model. Experiment phantoms are designed to test the performance.

Chapter 7 is a comprehensive work on multiple frequencies EIT with complex conductivity reconstruction while applying on an EIT-based fabric pressure mapping sensor. This gives an understanding of how doing a complex conductivity reconstruction with a range of frequencies could possibly benefit the image outcome.

In Chapter 8, a frequency difference EIT reconstruction method is used to separate a low frequency response object from a high frequency one. This could potentially be used in a lung tumour monitoring process.

Chapter 9 provides the conclusion and future developments of the PhD research.

# Chapter.2 EIT background

In this chapter a general introduction to electrical impedance tomography is presented. A brief history of EIT imaging will be given as well as a basic introduction to bio-impedance and its application in medical imaging.

## 2.1. Motivation

Impedance imaging using EIT has three primary applications: medical, geophysical and industrial [5]. Process tomography uses EIT to detect conductive fluids in flowing pipes. The petrochemical industry uses EIT to determine liquid quantity, mixing behaviour and to measure the flow rate. In geophysics it can be used for mineral detection over the earth's surface or for borehole scanning. For medical applications there are some challenging and promising applications of EIT, such as monitoring brain or lung functions [6, 7]. Conventional tomography techniques are expensive, requiring large hospital spaces, and emit radiation. EIT appears to be an attractive alternative as it is non- invasive, portable, inexpensive and easy to use.

## 2.2. Brief history

The first reported use of EIT can be traced back to 100 years ago in geological studies [8]. An identical technique named industrial process tomography (IPT) has been used today by industrial groups for detection of air bubbles in process pipes or for monitoring pipe flows [9]. Before 1978, EIT was developed for nonclinical applications until Henderson and Webster introduced the first published impedance image for human tissue [10]. They had produced a transmission map of the tissues directly from current-voltage data by using a rectangular array of 100 electrodes on one side of the chest earthed with a single large electrode on the other side. Low conductivity areas in the image were claimed to correspond to the lungs.

The first attempt at EIT began as an offshoot of X-ray computed tomography and was flawed in its theoretical assumption that electric currents flow in straight lines [11]. A wide range of image reconstruction techniques have been developed specifically to capture the behaviour of electrical current. An

impedance tomography system for imaging brain tumours was proposed by Benabid [12]. It was a prototype impedance scanner which had two parallel arrays of electrodes attached in a saline filled tank, and which was able to detect an impedance change inserted between the electrode arrays [7]. The first clinical impedance tomography system was developed by Baber and Brown in the Department of Medical Physics in Sheffield in 1987 [13, 14]. It was a commercially available prototype called the Sheffield Mark 1 system, which has been widely used to perform various clinical studies and is still being used by many EIT research centres today. It was a 16 channel system which was able to make multiple impedance measurements and could obtain 10 images per second. As for its advantages, the Sheffield Mark 1 [15] was portable and relatively inexpensive compared with ultrasound, CT and MRI scanners.

By the mid 1990s, Hellige and Hahn from the research group in Gottingen had developed a predominantly digital EIT system called GOE MF 2 [16], which was a further development step beyond the Sheffield Mark 1 system. They used the system to perform experimental validation studies of EIT on animals, physiological studies in volunteers and clinical research. It was specifically designed for evaluating the capability of EIT to monitor regional lung function.

In 2001, a company named Drager, together with the Gottingen EIT group, initiated a cooperation strategy on the development of EIT with the mutual objective of improving the technology, design and software. The company was willing to make EIT not only for experimental research but also for daily clinical practice. They have introduced a new commercial device named Pulmo Vista 500 [17], which is one of the most successful commercial EIT systems in the world today.

EIT has been very successful in industrial process tomography applications. Industrial Tomography Systems (ITS) is a lead supplier of industrial electrical impedance tomography systems [18].

## 2.3.   Clinical applications

EIT has shown promising results in a wide range of clinical applications including thoracic, gastrointestinal function, breast cancer, lung and brain function [8, 17, 19]. Here is presented an overall progress on these applications.

### 2.3.1.  Electrical properties of biological tissues

When EIT is applied in clinical applications it uses the electrical properties of tissues and their cellular structure, including blood, to reconstruct an image which represents human organs or physiology mechanisms associated with cell structures [20]. There is a large resistivity contrast (up to about 200:1) between a wide range of tissue types in the body. Therefore it is possible to use resistivity to form anatomical images. Furthermore, there is often a significant contrast between normal and pathological tissue [21]. To measure resistivity, a current must flow in the tissue and the resulting voltages be measured. Although cell layers are rather complex biological systems, their electronic characteristics integrated over a large collective of cells can to a good approximation be modelled by basic elements [22]. Tissues and tumours both consist of cells and membranes which have high resistivity and also can be seem as small capacitors. In tumours, the cell density is often higher than normal cells, which results in a rise in impedance. Figure 1 shows an equivalent circuit diagram for bioimpedance cell structure. The impedance properties of tissue comprise two components: the resistance $TER$ and reactance. The conductive characteristics of body fluids provide the resistive component $R_{med}$, whereas the cell membranes act as imperfect capacitors $C_{cl}$. The electrodes and in particular the interface between the electrodes and the culture medium exhibit a more complex impedance behaviour, which is called constant phase element ($CPE$). The CPE model is suited to mathematically describe the characteristic frequency-dependence of the electrode-medium interface's impedance.
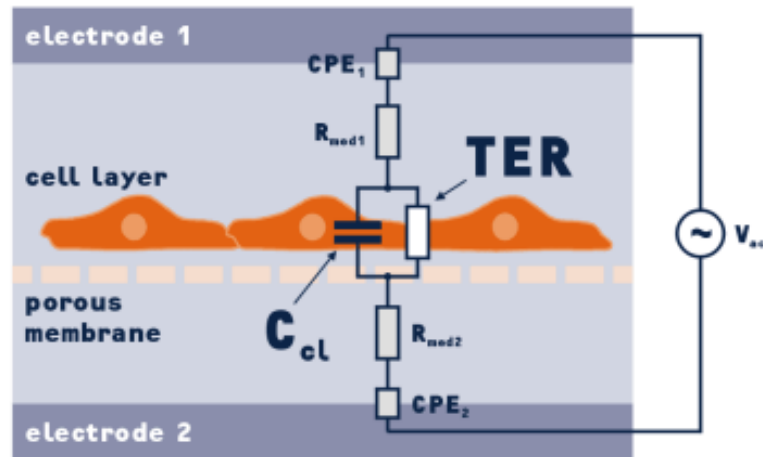
*Figure 1: Cell impedance model (Adapted from [22])*

The biological tissue impedance measurements can be made over a range of frequencies from low (20Hz) to high (10MHz). The impedance properties of biological tissues vary within a whole frequency spectrum (Figure 2). The step changes in impedance are called dispersions and are due to the loss of particular polarization processes as frequency increases [23].



*Figure 2: Idealized spectra of the dielectric properties of tissues [24]*

As shown in Figure 3, while high frequency measurements are applied, the current passes right through membranes, and the result is dependent on tissue and liquids both inside and outside the cells. At low frequencies the membranes

impede current flow. Therefore, bioimpedance can be used to measure volumes, shapes or electrical properties of tissue.



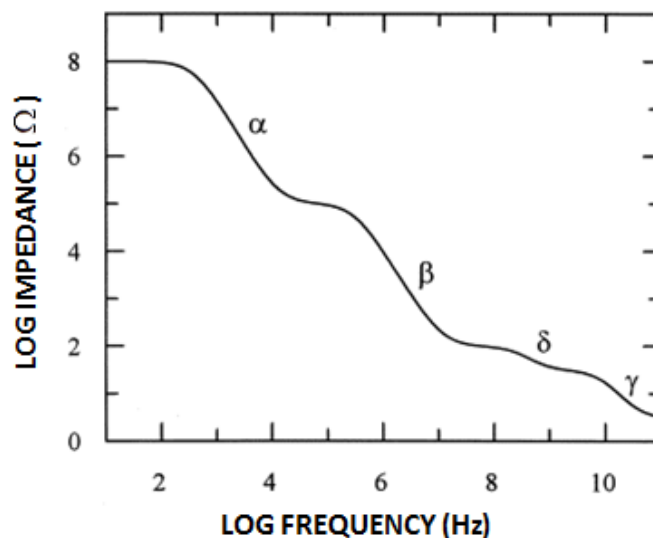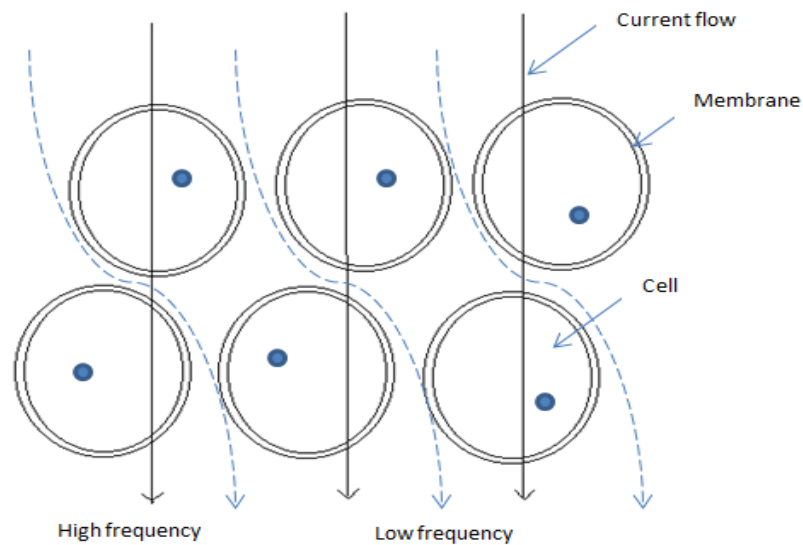*Figure 3: Impedance properties of tissue*

### 2.3.2. Lung EIT

There are many traditional imaging modalities for monitoring pulmonary function, such as X-ray, CT and MRI scanners. These techniques are relatively mature and provide high spatial resolution images. However, to image ventilation and perfusion with these methods, patients must be brought to the device and repeatedly exposed to ionising radiation (in the case of X-ray and CT scanners), which is undesirable. Also the systems are required to be stationary, and with high capital and maintenance cost. EIT provides an alternative solution for these disadvantages in lung function monitoring. One of the most promising areas that thoracic EIT [7] is focusing on is detection of blood clots in the lungs or pulmonary emboli, a common and often serious complication of surgery. There is also potential in using EIT for bedside monitoring of lung gestation of pre-term neonates [25]. Premature birth is often accompanied by complications due to lung immaturity. Lung disease in infancy can cause long-term health problems. Therefore, it is important to monitor lung maturity and development of pre-term neonates [26]. EIT has made lung function testing available for this age range and provides a safe and non-invasive observing environment. This

may improve the quality of clinical care of infants and of those with lung and heart diseases.

Lung EIT is becoming a major clinical diagnosis area of medical EIT imaging [26, 27]. In the clinical field, patients with acute lung injury in respiratory require positive pressure ventilation to ensure adequate gas exchange. Mechanical ventilation (MV) represents the main support to maintain acceptable pulmonary gas exchange whilst treating the underlying disease [28]. However, with high pressure applied to obtain a sufficient tidal volume for specific patients, MV could lead to lung injury due to over distension. Damage caused by MV to the lungs has been termed ventilator-induced/associated lung injury (VILI/VALI). This awareness triggered extensive research into potential solutions, the most important ones being lung protective ventilation (LPV) strategies [29]. Implementing LPV strategies requires an online monitoring tool capable of providing information on the regional behaviour of lungs and which EIT potentially offers. Therefore, the increasing awareness of LPV strategies leads to the motivation of driving EIT research into a useful tool to help in optimizing LPV strategies.

To show the progression of interest in the clinical application of EIT monitoring, Figure 4 indicates the number of publications on lung EIT compared with those on VILI/VALI and on LPV over 50 years. Interest in lung EIT increased when more work was done in VILI and VALI in clinical study.
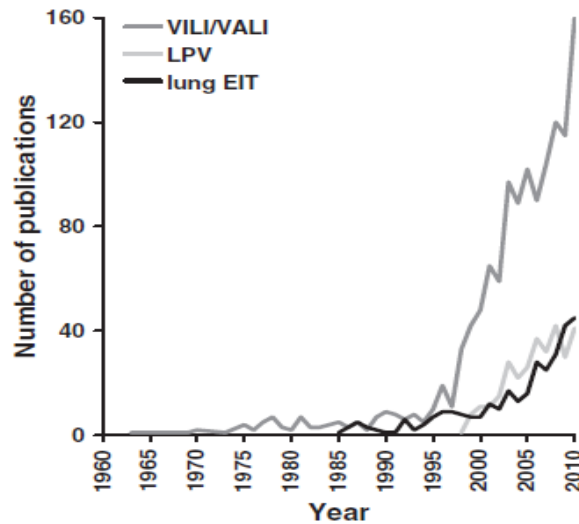
*Figure 4: Number of publications on VILI/VALI, LPV and lung EIT in peer-reviewed journals (Adapted from [29])*

It can be observed that the publication number increased significantly in recent years, which proved the increasing interest and potential development of lung EIT.

### 2.3.3. Breast tumour

As the cell density of tumours is higher than normal tissues, different impedance properties could be detected by using EIT when monitoring the common condition of breast cancer [30-32]. X-ray mammography is being used for women breast cancer imaging at the moment. The limitation of this is that during the procedure the patient's breast has to be compressed flat in order to visualize all the tissue and minimize the required radiation dose; this could cause discomfort or pain for the patient. The research groups in Dartmouth [33, 34] and Moscow [35] have made preliminary clinical tests of breast tumour imaging using EIT, but a satisfying result has not as yet been proved.

### 2.3.4. Brain function

There are two main potential areas of imaging brain function in clinical applications, which are epileptic activity and stroke. Traditional scanners like X-ray CT and MRI are well-developed for the job, although it is not practicable to operate serial or rapid imaging. The problem occurs when immediate

thrombolytic drugs are required for a stroke due to haemorrhaging. It is not possible for a CT scan to obtain images and report the situation in 30 minutes. EIT is able to apply continuous monitoring which enables distinction of haemorrhagic from ischaemic stroke, thus enabling the rapid use of thrombolytic drugs. One of the difficulties faced by brain EIT imaging is that current is hard to inject through the resistive skull. The EIT group in University College London have been developing an optimized brain imaging EIT system. They have achieved satisfactory image quality through the resistive skull by using widely spaced electrodes for current injection [6]. Using the Sheffield Mark 1 system, a series of pilot studies have been performed in animals with electrodes placed directly on the brain, and observations show that suitable impedance changes could be detected in stroke, epilepsy and evoked activity [36-38].

## 2.4. Industrial process tomography

Electrical resistance tomography (ERT) is the most popular solution for industrial process applications [39, 40]. EIT has also been developed for on-line imaging of two-phase flows as a new high speed tomography [39, 41]. It has been proved to be a powerful tool for mapping the concentration and velocity distributions of the second phase in two-phase flows, where conductivity difference exists between the two-phase fluids [42]. For instance, EIT has been used to visualize the bubble distribution in a two-phase flow field and it provides a simpler and cheaper solution than other existing techniques [18, 43].

## 2.5. EIT-based fabric pressure mapping sensor

Apart from conventional applications like Industrial EIT, geophysical EIT and medical EIT, EIT as a pressure mapping imaging method is relatively new in the research field [44].

When pressure is applied to a fabric patch whose boundary is clamped, its conductivity decreases with increasing pressure. Pressure-induced shape change over the sensor area creates a change in the conductivity distribution, which leads to the change in current-voltage data in the EIT system. The EIT system displays the image of the conductivity changes from current-voltage

data measured at the boundary of the fabric patch. Finally, the pressure distribution is estimated from the conductivity images. In terms of application, this particular technology enables pressure monitoring applications such as pressure ulcer prevention in clinical care. Additionally, potential touch sensitive applications to robotic skin can be considered since conventional point-based sensor mapping is almost impossible to implement for complex geometries like hand and face [45-47].

The original idea of applying EIT-based pressure sensing for pressure ulcers was initially introduced by Fulton and Lipczynski in 1993 [48]. However, experimental trials failed to identify a suitable conductive material for an EIT pressure sensor. At that time, they did not take advantage of the enhanced flexibility and stretch potential of a fabric-based EIT sensor. So the work was eventually dropped. Recently, Alirezaei [49] has shown promising results with regard to flexibility and stretch potential of these sensors and their integration in robotics as an artificial skin interface. Together with various new conductive materials, such as pressure sensitive and conductive rubber as well as many other fabric-based materials developed over the years, the EIT-based pressure mapping imaging has progressed rapidly and has become a promising technique.

## 2.6. Theory

In practice most EIT systems use constant current sources and measure voltage differences between adjacent pairs of electrodes. To obtain an image with good spatial resolution, a number of such measurements are required. This can be achieved by applying different current distributions to the body, and repeating the voltage measurements. From the set of measurements, an image reconstruction technique generates the tomographic image. Mathematically, the known quantities are the voltages and currents at certain points on the body; the unknown is the resistivity within the body, which is the inverse problem [39, 50]. In order to solve the inverse problem the forward problem needs to be solved. At low frequencies, these quantities are related by Laplace's equation:

$$\nabla \cdot \sigma \nabla \phi = 0$$

where $\sigma$ is the conductivity (admittivity may be represented by a complex $\sigma$) and $\phi$ is the potential.

With suitable boundary conditions the above forward problem can be solved. Most in-vivo images have been produced using linearised, approximating techniques. These attempt to find a solution for a small change in resistivity from a known starting value. Until recently, the change in resistivity was measured over time, and EIT images were inherently of physiological function. Time difference 2D imaging is widely used in lung EIT. It is now possible to produce anatomical images using the new reconstruction technique, by imaging changes with frequency (frequency difference imaging).

Three dimensional EIT (using multiple rings of electrodes and designed to create a 3D image of conductivity changes in a larger section of lungs) [51] has not yet been widely studied considering the difficulties caused by an increase of electrode numbers, a complicated reconstruction process, etc. Some people have done simulation studies on 3D EIT, such as 3D image reconstruction based on a complete electrode model [52], and a finite element method of solving the 3D EIT forward model [53]. However, proper hardware design and experimental validation are lacking. For the advantages of acquiring better information, it is considered to be a potential benefit for clinical use. Also the idea of taking multiple frequency measurements to detect the characteristic differences between tissue types [54, 55] is a potential improvement for monitoring tumour in clinical use.

## 2.7    Introduction to frequency difference EIT

EIT has various potential applications in the medical area, such as function monitoring in lung EIT imaging. In traditional lung EIT imaging, dynamical images of the entire lung are generated to clinically investigate aspects of respiratory functions. Lung tumour imaging using EIT is proposed during cancer treatment processes such as radiation therapy. This poses some major challenges including: spatial resolution for lung tumour imaging is far more challenging than imaging entire lung itself; time difference imaging that may not work as the reference image of the patient without lung tumour may not exist.

Additionally, imaging a lung interior may become very challenging due to its low electrical conductivity, so a complex impedance imaging may be needed. Traditional EIT reconstruction uses a time difference imaging technique. However, time difference EIT may not be useful for monitoring lung tumour behaviour as it is difficult to obtain background data of the lung while the tumour has already existed in the region [33, 56, 57]. This problem may be solved by using frequency difference reconstruction [58-61] as it only requires measurement data at two different frequencies. In early frequency difference EIT (fdEIT) methods, frequency-difference images were formed by back-projecting the algorithm of the ratio of two voltages at two frequencies [58, 62-65]. More recent studies adopted the sensitivity matrix with a voltage difference at two frequencies [31, 66]. This will work in clinical cases only if two frequencies at which the tumour has a different electrical conductivity (or permittivity) compared to normal tissues can be found [67, 68]. From Figure 5 it can be observed that the average conductivity of tumour tissue is significantly higher than normal tissue over the entire frequency range (from 10Hz to 1MHz). The difficulty is that lung itself has a different frequency response compared to chest tissues [69]. In this case, EIT for lung tumour monitoring can take advantage of a priori information from diagnostic X-Ray CT images; both data from thorax and lung are treated as background data. When a lung tumour is moving or changing, conductivity changes due to frequency change can produce a conductivity image of the lung tumour.
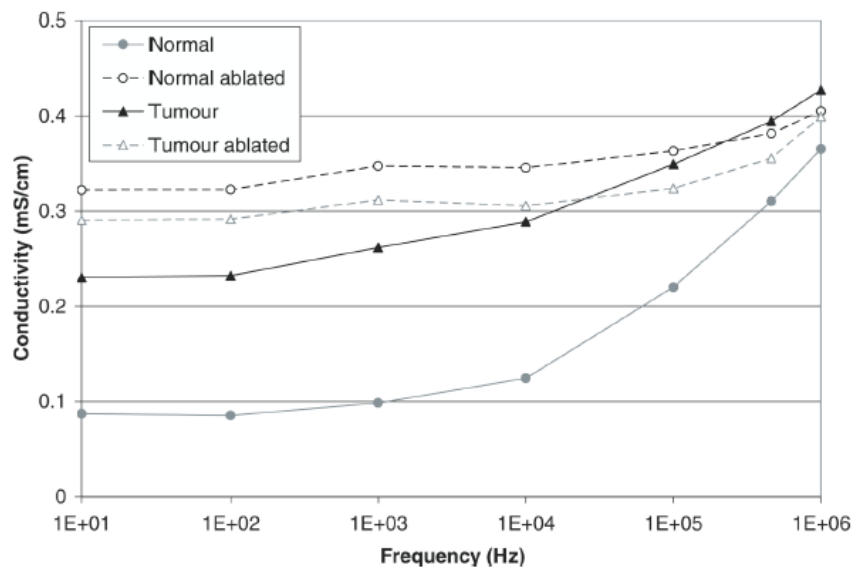
*Figure 5: Spectral behaviour of normal and tumour tissue (adapted from [21])*

## 2.8 State of technology

### 2.8.1. Hardware

Many versions of EIT systems have been developed by academic research groups all over the world, including commercial clinical EIT systems [70]. Table 1 shows specifications of a list of recent EIT systems.

Table 1: Specifications of EIT systems used throughout the world

| Protocol | Number of channels | Speed | Resolution | Bandwidth | SNR |
|---|---|---|---|---|---|
| Two-terminal voltage source | 64 parallel | Dartmouth 30 frames s-1 30 meas s-1 | 16bits | 10kHz- 10mHz | 100dB |
| Four terminal current source | 32 channel semi parallel | Kyung Hee (IIRC) 1 frames s-1 32 meas s-1 | 12 bits | 10Hz- 500 kHz 10 frequencies | 100dB |
| 2/4 terminal current source | Current and volt semi parallel | Oxford Brookes OXBACT 5 25 frames s-1 25 meas s-1 | 16 bits | 26kHz– 56kHz Single frequency | n/a |
| Two-terminal voltage/ current | 72 channel parallel | Rensselaer ACT4 2.1 frames s-1 | 16 bits | 300Hz- 1MHz 8 frequencies | 90dB |
| Four | 8 channel | Sheffield Mk 3.5 | 12 bits | 2kHz- 1.6MHz | 40dB |

| terminal current source | semi parallel | 25 frames s-1 25 meas s-1 | | 30 frequencies | |
|---|---|---|---|---|---|
| Four channel current source | 64 channel serial | UCL Mk2.5 0.12 frames s-1 33 meas s-1 | 12 bits | 20Hz-1MHz 30 frequency | 40dB |
| Four terminal current source | 64 channel serial | UCL mk1b 3 frames s-1 774 meas s-1 | 12 bits | 225Hz- 77Khz Single frequency | 50 – 30 dB |

All current EIT systems are configured similar to the Sheffield Mark 1 system [15] with a small number (16-32) of electrodes either suited with a belt or attached to the thorax like a ring of electrodes. Current is driven across electrode pairs and differential voltages are measured. Current EIT systems have greatly improved noise and interference issues. The updated reconstruction algorithms provide much better image resolution and robustness to electrode errors with reduced image artefacts [71]. Furthermore, sampling rates become much higher, like the KCHU MARK system have up to 30 frames per second, which makes continuous analysis of lung ventilation and perfusion sufficient.

### 2.8.2. State of algorithms

The majority of EIT reconstructions are based on linear, one-step reconstruction algorithms known as back projection. More recently, the application of image reconstruction to a specific tomography problem has become simplified by the introduction of user-defined functions implemented from Electrical Impedance and Diffuse Optical Reconstruction Software (EIDORS). This is a tomography tool-suite written in MATLAB script and was first introduced in 2D form by Vauhkonen in 2000. More recently, EIDORS has been further enhanced into a

3D version [72]. It provides algorithms for forward and inverse modelling and also shares data and promotes collaboration between groups working in the field.

The most common EIT algorithms deal with static (time difference) EIT. In order for a static EIT image reconstruction algorithm to be reliable, a forward model that includes every aspect of the imaging object has to be constructed. This requires knowledge of the boundary geometry, electrode positions and other sources of systematic artefacts in measured data. However, in practice, it is difficult to obtain such information with a reasonable accuracy and cost. Since static EIT imaging is sensitive to these errors, it has a limited applicability so far. Even though numerous time-difference EIT (tdEIT) methods have been applied to image lung functions, stomach emptying, brain functions and others, there are cases where time-referenced data are not available. For example, in all applications of EIT for tumour imaging, including breast tumours, time-referenced data do not exist at the time of imaging since the patient either has a tumour or not at that time. Stroke-type detection using EIT is another example. In these cases, static EIT imaging has been tried but reconstructed images suffered from all kinds of technical difficulties.

In medical problems conductivity contrasts can be large. Using the linearised method to calculate a change in conductivity between two states, measured either at different times (dynamic imaging) or with different frequencies is considered to be useful. Complex conductivity spectra of numerous biological tissues show frequency dependent changes [5, 40, 68]. This indicates that a complex conductivity distribution inside an imaging object can be viewed as a function of frequency. Based on this observation, there have been attempts to perform frequency-difference image reconstructions [62, 73-75]. However, there has been not much study on its theory and reconstruction algorithm, as well as on experimental results.

More mature algorithm developments on frequency difference EIT (fdEIT) were established by the EIT group from South Korea in recent years. A weighted frequency difference solver has been proposed and it suggests that images can be shown by utilizing differences of measured boundary voltages between

chosen frequencies. This creates a great interest on further fdEIT experiments for future potential applications that tdEIT cannot solve.

## 2.9.    Conclusion

The chapter has shown an overview of electrical impedance tomography. A background study and recent developments of technology have been introduced. The fundamental knowledge of how EIT can be applied to clinical applications has been described. Evidence has shown that EIT is reliable and can possibly be an alternative solution for a whole range of clinical problems. There is now a large and growing interest in the technology and commercial devices have been introduced to the market recently. However, there are still many issues that have not been solved, such as relatively low spatial resolution and electrode position errors, which could slow down the development progress. Overall, the author believes that there are still many improvements can be made including both software and hardware design for EIT systems. Therefore, this study is motivated and can potentially make a contribution to the clinical and other fields.

# Chapter.3 EIT Hardware and software

This chapter introduces EIT hardware and software. Two EIT systems are being using in the research laboratory. The first one is a LabVIEW based EIT system with 16 channels built by Mehmet Emre [76]. For experiments with more measurements and accuracy, a 32 channel system would work better than the 16 channel one. This chapter describes the task to extend the original design to a 32 channel system. The other system being used is the KCHU Mark2.5 commercial EIT system from Yonsei University Korea. EIT reconstruction software is briefly introduced in this chapter.

## 3.1. LabVIEW based EIT system

### 3.1.1. Hardware set up

EIT systems apply current to a medium or a body and the resulting voltage created by the electric field is measured by electrode sensors [77]. The number of electrodes can vary depending on the system. A larger number of electrodes will yield higher resolution but will increase the processing time. 16 electrode systems are commonly used by many institutions, such as Sheffield and Manchester. Figure 6 indicates the block diagram of an EIT hardware design. The desired measurement protocol can be achieved by adopting a suitable switching pattern for the multiplexer. The multiplexer enables excitation sequence of the current injection and voltage measurement pattern to be applied onto the sensor electrodes. The data acquisition system collects differential voltage values from the multiplexer, converts them into binary form and transfers the data to the PC. The received data is used to produce images by using image reconstruction algorithms. The data acquisition system is also capable of acting as the current source.
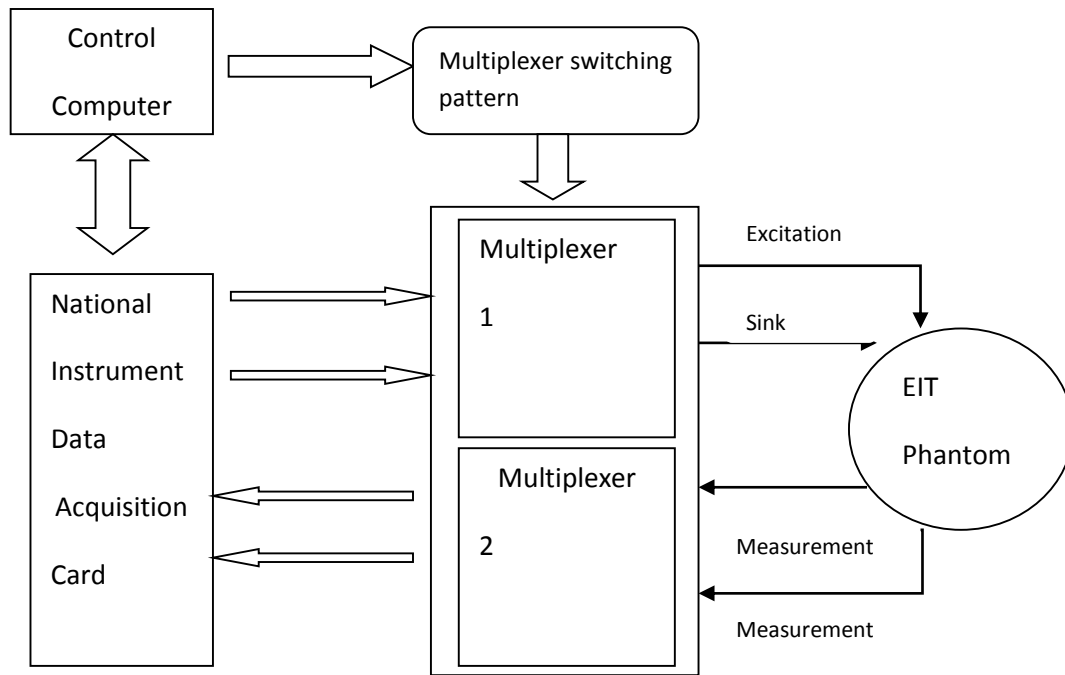
*Figure 6: Block diagram of 32 electrode EIT system hardware*

The system built is LabVIEW based, using the National Instruments DAC for data acquisition and multiplexers for channel switching. Figure 7 is a picture of the whole system including the power supply, data acquisition card, multiplexer and the EIT test phantom. Two multiplexers are used to control the DAC switching; one supplies excitation to the electrodes and second acquires the measurements. There are 32 different current excitation patterns and each arrangement has 29 differential voltage measurements, so 32*29=928 measurements.
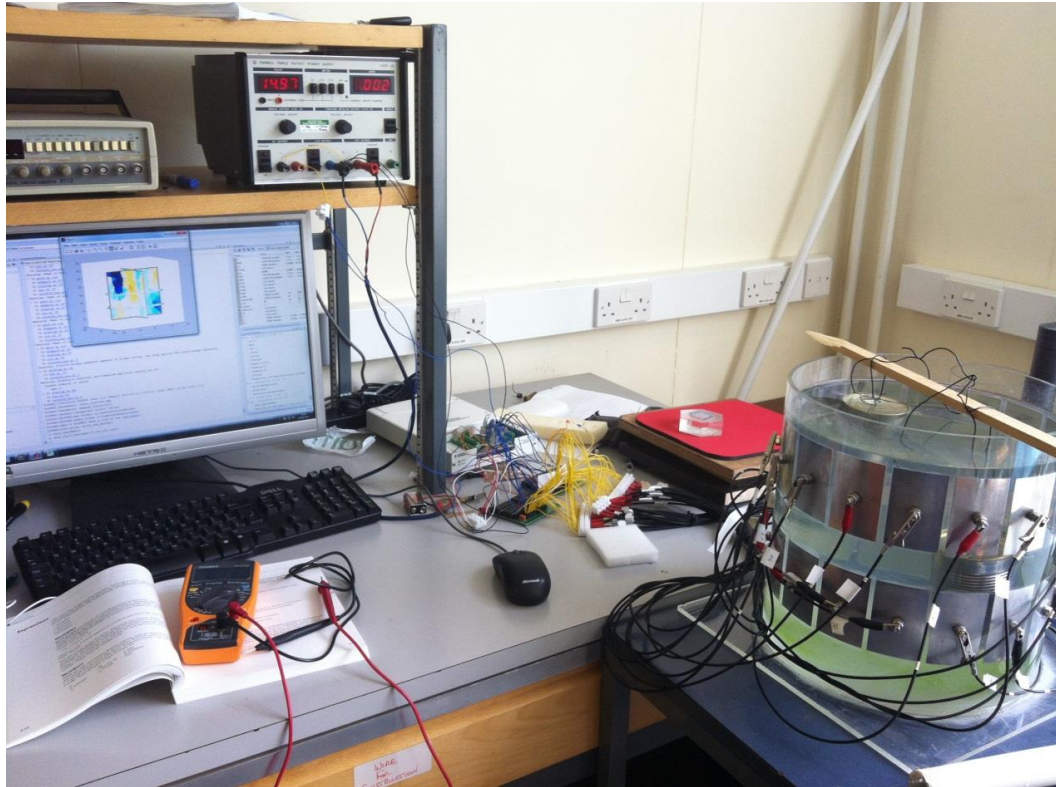
*Figure 7: Picture of a 32 channel 3D EIT system*

### 3.1.2. Data acquisition

The data acquisition system collects the measured voltage from electrode and then the data is processed by a PC [78]. The EIT system requires a high speed computer with sufficient memory to acquire the data. A data acquisition card minimises the use of hardware as it is capable of collecting measured data accurately at high sampling rate. Conventional data acquisition systems require hardware to measure voltage, to filter, demodulate and convert to digital form, and a signal processing unit to transfer the data to PC. The National Instruments data acquisition card has a built-in data pre-processing unit; hence it receives data, converts to digital signal and transfers to the PC without having to use additional hardware, so the use of hardware is minimised. The system is also compatible with LabVIEW, which enables control of the sensor's switching pattern during the measurement process.

### 3.1.3. Multiplexer switching

The upgrade requires the designing of a 32 channel multiplexer and the revised switching patterns' binary codes. There are two feasible approaches for the

multiplexer design. One is to redesign a 32 channel multiplexer by using a 1 to 32 channels multiplexer. This is low cost, efficient and consists of minimal circuitry and hence reduced measurement errors due to stray capacitance. However, there is very limited number of 32 channel multiplexers available in the market and most of these multiplexers are not suitable for an EIT application. The second approach is to use an existing 16 channels multiplexer circuit with inverters to develop 32 channel systems. This second system requires twice as much circuitry but it will save time on designing an entirely new system and it is also proven to be suitable for an EIT application; therefore an existing 16 channel multiplexing system would be adapted to operate on a 32 channel system. The diagram below shows the current excitation and voltage measurement circuit diagrams for the 32 channel multiplexer. Channels 1-16 can be measured from the multiplexer 1.1 and then channels 17-32 can be made operational by switching enable pin high, which switches off multiplexer 1.2 ON and 1.1 OFF [51]. The same principles apply for the remaining 8 multiplexers. Figure 9 is the designed circuit diagram of the multiplexers. Figure 8 below demonstrates the first measurement pattern for current excitation on electrodes 1 and 2. A similar table can be used to create the switching pattern for the remaining excitation and measurement patterns. There are 32 different current excitation patterns and each arrangement has 29 differential voltage measurements, so 32*29=928 channels.

| channels | current 1 Channel | 2 channel | voltage 1 channel | voltage 2 Channel | current excitation | current sink | measurement 1 | measurement 2 |
|---|---|---|---|---|---|---|---|---|
| 1 | 1 | 2 | 3 | 4 | 00000 | 00001 | 00010 | 00011 |
| 2 | 1 | 2 | 4 | 5 | 00000 | 00001 | 00011 | 00100 |
| 3 | 1 | 2 | 5 | 6 | 00000 | 00001 | 00100 | 00101 |
| 4 | 1 | 2 | 6 | 7 | 00000 | 00001 | 00101 | 00110 |
| 5 | 1 | 2 | 7 | 8 | 00000 | 00001 | 00110 | 00111 |
| 6 | 1 | 2 | 8 | 9 | 00000 | 00001 | 00111 | 01000 |
| 7 | 1 | 2 | 9 | 10 | 00000 | 00001 | 01000 | 01001 |
| 8 | 1 | 2 | 10 | 11 | 00000 | 00001 | 01001 | 01010 |
| 9 | 1 | 2 | 11 | 12 | 00000 | 00001 | 01010 | 01011 |
| 10 | 1 | 2 | 12 | 13 | 00000 | 00001 | 01011 | 01100 |
| 11 | 1 | 2 | 13 | 14 | 00000 | 00001 | 01100 | 01101 |
| 12 | 1 | 2 | 14 | 15 | 00000 | 00001 | 01101 | 01110 |
| 13 | 1 | 2 | 15 | 16 | 00000 | 00001 | 01110 | 01111 |
| 14 | 1 | 2 | 16 | 17 | 00000 | 00001 | 01111 | 10000 |
| 15 | 1 | 2 | 17 | 18 | 00000 | 00001 | 10000 | 10001 |
| 16 | 1 | 2 | 18 | 19 | 00000 | 00001 | 10001 | 10010 |
| 17 | 1 | 2 | 19 | 20 | 00000 | 00001 | 10010 | 10011 |
| 18 | 1 | 2 | 20 | 21 | 00000 | 00001 | 10011 | 10100 |
| 19 | 1 | 2 | 21 | 22 | 00000 | 00001 | 10100 | 10101 |
| 20 | 1 | 2 | 22 | 23 | 00000 | 00001 | 10101 | 10110 |
| 21 | 1 | 2 | 23 | 24 | 00000 | 00001 | 10110 | 10111 |
| 22 | 1 | 2 | 24 | 25 | 00000 | 00001 | 10111 | 11000 |
| 23 | 1 | 2 | 25 | 26 | 00000 | 00001 | 11000 | 11001 |
| 24 | 1 | 2 | 26 | 27 | 00000 | 00001 | 11001 | 11010 |
| 25 | 1 | 2 | 27 | 28 | 00000 | 00001 | 11010 | 11011 |
| 26 | 1 | 2 | 28 | 29 | 00000 | 00001 | 11011 | 11100 |
| 27 | 1 | 2 | 29 | 30 | 00000 | 00001 | 11100 | 11101 |
| 28 | 1 | 2 | 30 | 31 | 00000 | 00001 | 11101 | 11110 |
| 29 | 1 | 2 | 31 | 32 | 00000 | 00001 | 11110 | 11111 |

*Figure 8: Multiplexer switching code for electrode excitation 1 and 2* [51]
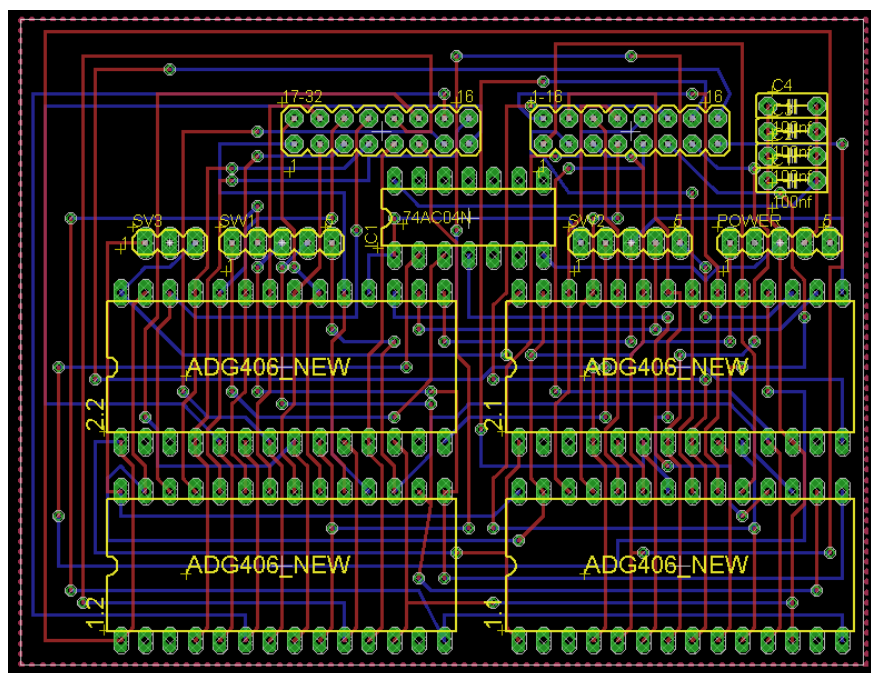


*Figure 9: Multiplexer design of 32 channel system*

### 3.1.4. 32 Channel multiplexer wiring design

Figure 10 shows the connection diagram for excitation systems for a 32 electrode system. As we can see from the diagram, pins 31 and 47 are used for outputting the current to the multiplexers, where pin 31 is the excitation pin and

47 is the current sink. Pins 65 – 74 are used to turn the multiplexer switching patterns.
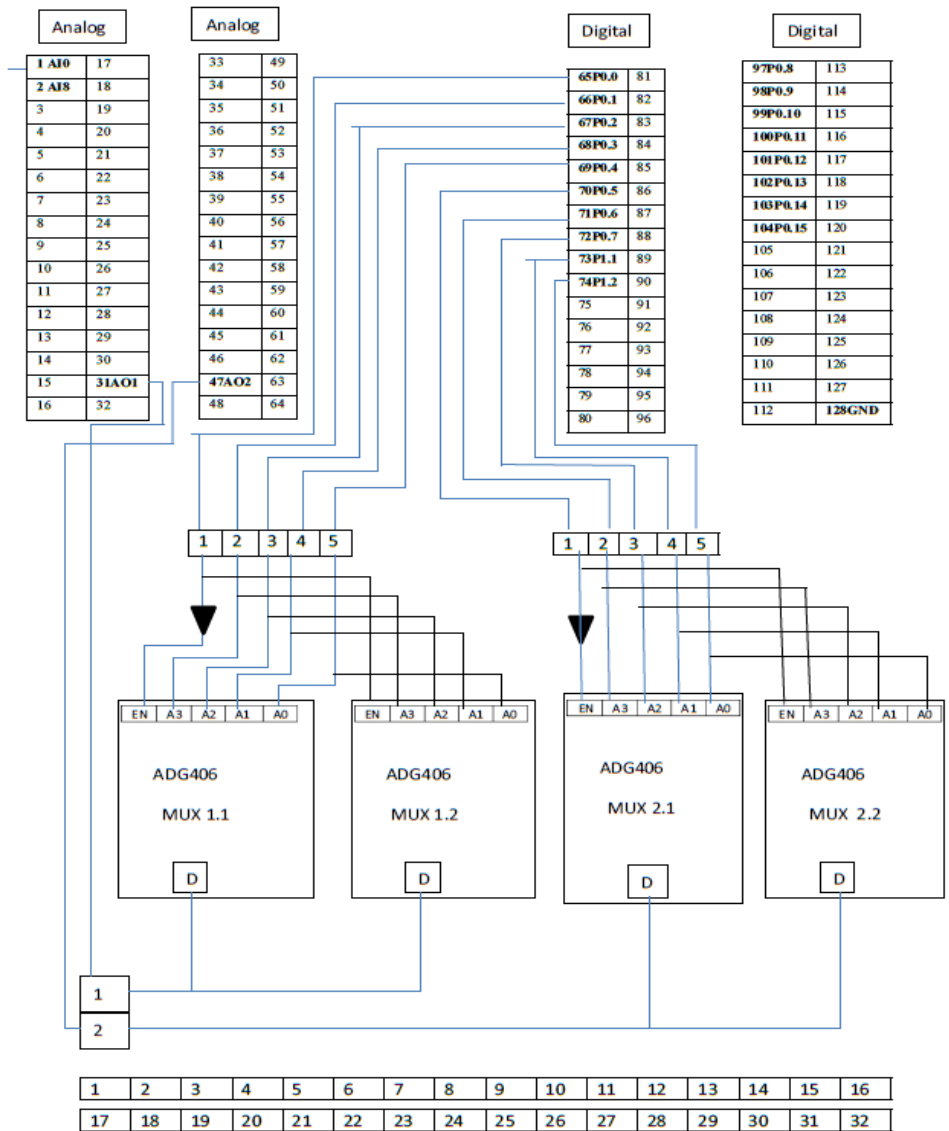


*Figure 10: A 32 channel wiring system for excitation*

Figure 11 represents the wiring diagram of data acquisition system for a 32 electrode system. Pins 1 and 2 are used for taking measurements. Pins 97 to 106 are used for driving the switching code for measurements.
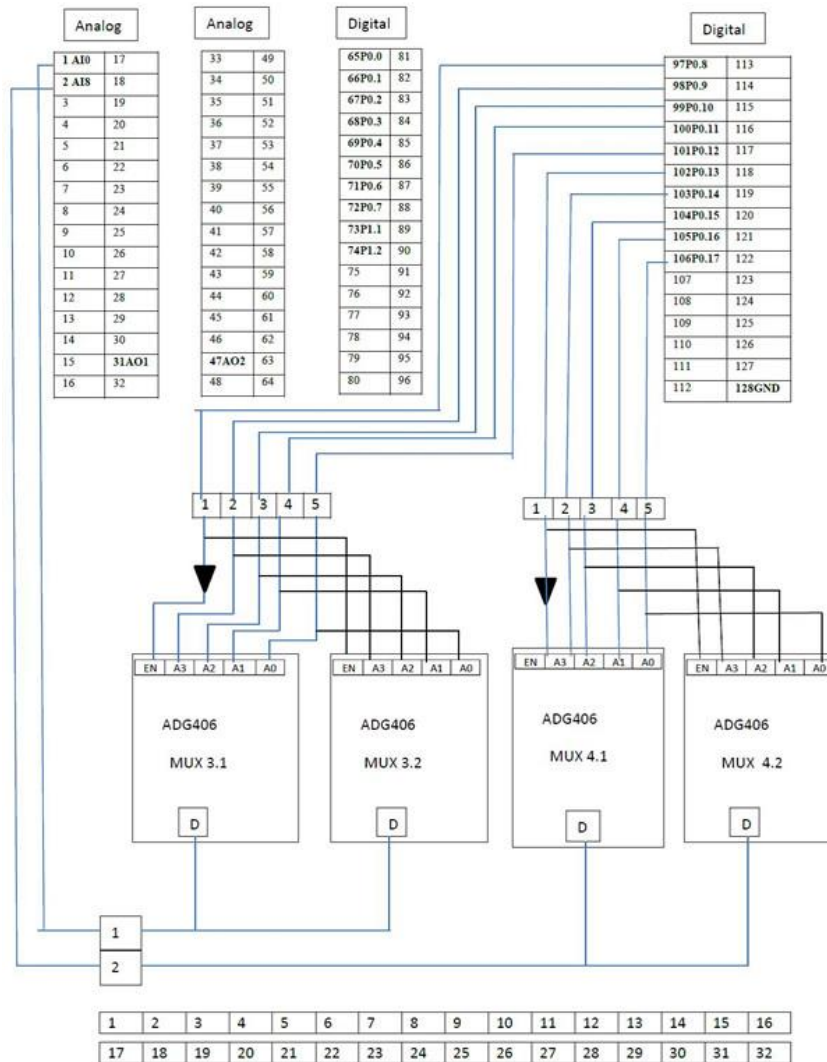
*Figure 11: A 32 channel data acquisition wiring diagram for voltage measurement*

## 3.2. KCHU Mark2.5 system

The KCHU Mark2.5 EIT system is a 16-channel system and has one power box and one current source. It can be used for multi-frequency tests. Figure 12 shows the device and its power supply. The system is optimised for operating from 50Hz to 500kHz. The output impedance of the current source is over 1 MΩ at all chosen frequencies.

The main issue in obtaining the complex impedance spectrum in EIT hardware is maintaining a similar performance at the low and high operating frequency. The improved Howland current source is adopted to maximize output

impedance and wide-band voltage measurement amplifiers. Additionally, the circuit for calibrating the output impedance of the current source is inserted at the operating frequency which was over 1MHz. A detailed description for the hardware is written in [79, 80].



*Figure 12: Photo of the KHU Mark2*

The current source has a high current amplitude stability of 0.009–0.095% and a low total harmonic distortion of $0.2\times10^{-3}$ to 0.08%. The signal to noise ratio is about 75-85dB depending on frequencies and measurement channels [6].

The complete system contains the following parts: (1) a computer with an USB port and EIT software; (2) a main controller, DSP (TMS320LF2812 [81]); (3) an intra-network controller on a digital backplane; (4) impedance measurement modules; and (5) switching circuits on an analog backplane [82].

TMS320LF2812 (see detail in the Appendix) is the newest and the best-performance DSP controller among the TMS320C2000 series. It has 56 digital I/O ports, 128KX16bit flash and 18KX16bit SRAM. The highest sampling frequency is 150MHz.

The general structure of the KHU Mark2.5 is imaged below (Figure 13). The analog switching board is used for signal switching (like AC/DC or DC/AC) and after the 16 IMM channels the signal is transferred to the digital backplane which contains a DSP controller and an intra-network controller, which lastly sends it to the PC computer to process the image.
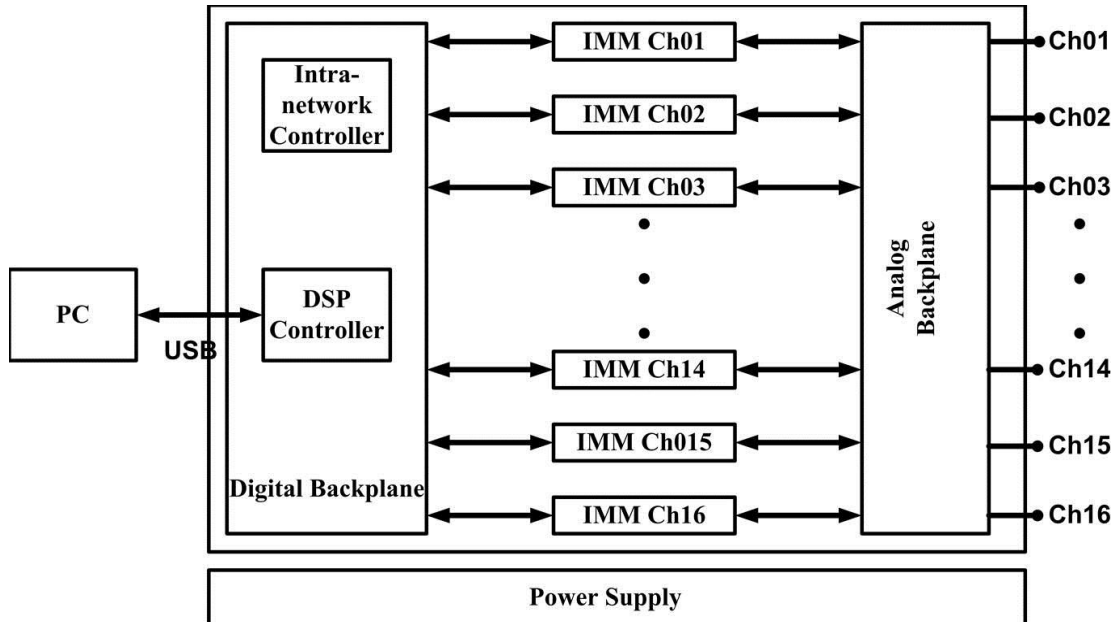


*Figure 13: Structure of the KHU Mark2 (adapted from [82])*

## 3.3. EIT software

This section explains the mathematical framework of EIT which includes forward problem, inverse problem and regularization techniques etc. Algorithms used in all experiments and simulations are described in detail in this chapter.

### 3.3.1. EIT measurement pattern

A variety of protocols for injecting current and collecting voltage measurements have been proposed over the years [52]. There are two main driving protocols which are pair drive and multiple drives. The pair drive method uses a single source current connected to the driving electrode pairs with measurements on the remaining pairs of electrodes. The current source is then switched to another pair of electrodes and the measurement is repeated on the remaining electrode pairs. The multiple drive system is able to drive current in more than two electrodes at one time, but with a more complex set-up and higher costs.

The most common measurement pattern is known as the adjacent pattern. The current is applied to the adjacent electrodes and voltage is measured on the remaining adjacent electrodes. For a 16 channel example, the current is applied to an adjacent pair of electrodes and the resultant voltages between the remaining 13 adjacent pairs of electrodes are measured. In Figure 14, current is injected through an electrode pair (1, 2) and the resulting boundary voltage differences are measured from electrode pairs (3, 4), (4, 5)… (14, 15), (15, 16) [83]. Voltages are not measured between pairs (16, 1), (1, 2), or (2, 3). Secondly, the current is injected between pair (2, 3), and the voltage difference measurements are done between pairs (4, 5) (5, 6) … (15, 16) (16, 1). The process is repeated 16 times, which means that all 16 adjacent pairs of electrodes have been powered. The total number of measurements will be 16x13=208. This would produce a data frame that has size of 1x208. The current is excited around the boundaries and therefore the resolution is greater on the outer regions and relatively low in the central region.
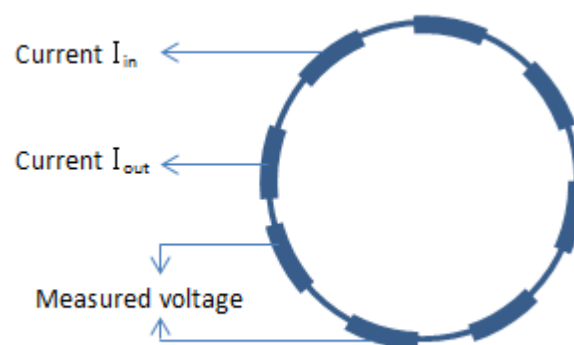


*Figure 14: Adjacent current pattern of a 8 electrode EIT system [39]*

### 3.3.2. Forward model

An image, or solution, is obtained by repeatedly running a forward model and an inverse solver until convergence is attained. The forward problem of EIT is to determine the voltage distribution arising from the current pattern injection onto the object [84].

The basic field quantities involved in EIT are the electric field E and the magnetic field H, which will be modelled as vector valued functions of space

and time [85]. Electric displacement D and magnetic flux B will be produced when the fields are applied to a material. By Faraday's Law of induction:

$$\nabla \times E = -\frac{\partial B}{\partial t}$$

(1)

and Coulomb's Law:

$$\nabla \times H = \frac{\partial D}{\partial t} + J$$

(2)

where $J$ is the electric current density. Assume the media to be linear and isotropic, the magnetic permeability is then a scalar function $\mu$ and the magnetic flux $B = \mu H$. The permittivity $\varepsilon$ is similar to the permeability with $D = \varepsilon E$. In a conductive medium, the conduction current density is $J_c = \sigma E$. The total current is then $J = J_c + J_s$, the sum of the conduction and source currents. Now the time harmonic Maxwell's equations are given by:

$$\nabla \times E = -i\omega\mu H$$
$$\nabla \times H = i\omega\varepsilon E + J$$

(3)

The conductivity and permittivity can be combined as a complex admittivity $\sigma + i\omega\varepsilon$ and the equation becomes:

$$\nabla \times H = (\sigma + i\omega\varepsilon)E + J_s$$

(4)

Typically in EIT the source current $J_s$ is zero at frequency $\omega$. The quasi-static approximation assumes $\omega\mu H$ is negligible, so that $\nabla \times E = 0$ and therefore for a scalar potential $\phi$, $E = -\nabla\phi$.

### 3.3.3. Direct approach and complete electrode model

We have a given body $\Omega$ with a smooth boundary $d\Omega$. The body has conductivity $\sigma$. The scalar potential is $\phi$ and the electric field is $E = -\nabla\phi$. From Ohm's law, the current density is $J = -\sigma\nabla\phi$. In the absence of interior current sources, Kirchhoff's law is governed by Laplace's equation:

$$\nabla \cdot \sigma\nabla\phi = 0$$

(5)

where $\phi$ is the complex-valued electric potential and $\sigma$ is the complex conductivity of the medium. The appropriate boundary conditions (complete electrode model) [6, 52, 53, 86] are needed to enable a representative model for the EIT measurement process. Utilisation of the boundary condition of the complete electrode EIT model includes,

$$\phi + z_l \sigma \frac{\partial \phi}{\partial \eta} = U_l, \qquad r_x \in e_l, l = 1, 2, ..., L,$$

$$\int_{e_l} \sigma \frac{\partial \phi}{\partial \eta} dS = I_l, \qquad r_x \in e_l, l = 1, 2, ..., L,$$

$$\sigma \frac{\partial \phi}{\partial \eta} = 0, \qquad r_x \in \partial \Omega / \cup_l^L e_l,$$

(6)

where $z_l$ is the effective contact impedance between the $l^{th}$ electrode and the tissue, $\eta$ is the outward normal to the surface electrodes, $U$ is the complex-valued voltage, $I$ is the complex-valued current and $e_l$ denotes the electrode $l$. Here, $r_x \in \partial \Omega / \cup_l^L e_l$ means a point on the boundary not under the electrodes [87, 88].

Let an imaging object occupy a two-dimensional region $\Omega$ with its boundary $\partial \Omega$. On the boundary, electrodes $e_l$, $l = 1, 2, ..., L$ are attached. For complex impedance imaging, given a current with magnitude $I$ and angular frequency $\omega$ is injected through a chosen pair of adjacent electrodes ($e_l$ and $e_{l+1}$) to generate an electric potential, the resulting potential $V$ is governed by:

$$\nabla \cdot (\sigma * \nabla \phi *) = 0$$

(7)

where $\sigma^* = \sigma + i\omega\varepsilon$ is the complex conductivity distribution.

The Jacobian matrix is then established for a linearised inverse problem [89]. If $\sigma$ and $V_R$ are the real parts of admittivity and voltage respectively, while $\varepsilon$ and $V_I$ are the imaginary parts, the complex voltage measurements are formed by:

$$J_{RR}\sigma + J_{RI}\varepsilon = V_R$$
$$J_{IR}\sigma + J_{II}\varepsilon = V_I$$

(8)

The Jacobian which corresponds to the effect of perturbations in conductivity on the real part of the measurements can be expressed as:

$$J_{RR} = \frac{\partial V_R}{\partial \sigma}$$

(9)

and the Jacobian corresponding to the effect of the conductivity perturbations on the imaginary part of the measurements is:

$$J_{RI} = \frac{\partial V_I}{\partial \sigma}$$

(10)

Therefore the remaining two combinations would be:

$$J_{IR} = \frac{\partial V_I}{\partial \varepsilon}$$

(11)

and

$$J_{II} = \frac{\partial V_I}{\partial \varepsilon}$$

(12)

Thus the forward problem would become:

$$J * \partial \sigma * = V *$$

(13)

$$\begin{bmatrix} J_{RR} & J_{RI} \\ J_{IR} & J_{II} \end{bmatrix} \begin{bmatrix} \sigma \\ \varepsilon \end{bmatrix} = \begin{bmatrix} V_R \\ V_I \end{bmatrix}$$

(14)

The complex conductivity perturbation $\partial \sigma*$ in Equation (7) can be computed by the linearised reconstruction algorithm via:

$$\partial \sigma* = (J*^T J* + \lambda L)^{-1} J*^T \partial V*$$

(15)

where is $J*$ the Jacobian matrix for complex impedance, $L$ is the regularization matrix, $\lambda$ is the regularization parameter and $V*$ is the complex measured voltage.

### 3.3.4. Inverse problem

The inverse problem is the image reconstructing step for EIT. The aim of the reconstruction algorithm is to determine the conductivity distribution given by

the voltage measurement and sensitivity matrix [90]. The following equation can be described as the voltage measurements across the surface:

$$\Delta V = J \Delta \sigma \qquad (16)$$

Where $\Delta V$ is the voltage measurement and $J$ is known as the Jacobian matrix which relates the voltage measurement to the image. The inverse problem of EIT is to solve $\sigma$ for given V and J. Therefore, the above equation becomes:

$$J^T \Delta V = J^T J \Delta \sigma \qquad (17)$$

$$\Delta \sigma = (JJ^T)^{-1} J^T \Delta V \qquad (18)$$

### 3.3.5. Tikhonov regularization and singular value decomposition

The EIT system is usually ill-posed [91, 92] and inconsistent because of some limited sources and noisy projection data. As a result it is very important to ensure a reasonable solution for the ill-posed problem to system equations existing at each linearised step [93, 94]. The system can be basically solved by using a linear back projection reconstruction technique including Tikhonov regularization [91].

Tikhonov regularization is the most commonly used method of regularization of ill-posed problems. The EIT inverse problem is not well-posed.

$$\Delta V = J \Delta \sigma \qquad (19)$$

The standard approach is known as linear least squares and seeks to minimize the residual:

$$\| \Delta V - J \Delta \sigma \|^2 \qquad (20)$$

where $\| \cdot \|$ is the Euclidean norm. This may be due to the system being over determined or underdetermined. In the latter case this is no better than the original problem.

$$\| \Delta V - J \Delta \sigma \|^2 + \| \Gamma \Delta V \|^2 \qquad (21)$$

$\Gamma$ is called the Tikhonov matrix. In many cases this matrix is chosen as the identity matrix, giving preference to solutions with smaller norms. In other cases, high pass operators may be used to enforce smoothness if the underlying vector is believed to be mostly continuous. This regularization improves the conditioning of the problem, thus enabling a numerical solution. An explicit solution, denoted by $\Delta\hat{V}$, is given by:

$$\Delta\hat{V} = (J^{T}J + \Gamma^{T}\Gamma)^{-1}J^{T}\Delta\sigma$$ 

(22)

The effect of regularization may be varied via the scale of matrix $\Gamma$. For $\Gamma = I$, $\Gamma^{T} = \alpha^{2}$, the above equation can be written as:

$$\Delta\hat{V} = (J^{T}J + \alpha^{2}I)^{-1}J^{T}\Delta\sigma$$ 

(23)

Where $\alpha^{2}$ is the regularisation parameter dependent on the noise level and $I$ is the identity matrix.

The linear system would become better conditioned after the regularization is applied. However, it does not necessarily prove of having a perfect solution. When dealing with sets of equations or matrices that are either small or numerically very close to singular, a powerful mathematical technique called singular value decomposition (SVD) [95] is introduced. Singular value decomposition provides a convenient way for breaking a matrix, which perhaps contains some data that are interesting, into simpler, meaningful pieces [96].

Any $m \times n$ matrix with $m \geq n$ can be written as the product of an $m \times n$ column orthogonal matrix $U$, an $n \times n$ diagonal matrix with positive or zero elements, and the conjugate transpose of an $n \times n$ orthogonal matrix $V$. SVD is a decomposition of matrix:

$$J = U\Sigma V^{T}$$ 

(24)

With singular values $\sigma_{i}$ and Tikhonov matrix $\Gamma = \alpha I$, the Tikhonov regularized solution can now be expressed as:

$$\Delta\hat{V} = (J^T J + \alpha^2 \Gamma)^{-1} J^T \Delta\sigma$$

$$\Delta\hat{V} = (U^T \textstyle\sum^T V \cdot U \textstyle\sum V^T + \alpha I)^{-1} U^T \textstyle\sum^T V \Delta\sigma$$

$$\Delta\hat{V} = V(\textstyle\sum^T \textstyle\sum + \alpha I)^{-1} \textstyle\sum^T U^T \Delta\sigma$$

$$\Delta\hat{V} = VDU^T \Delta\sigma \qquad\qquad (25)$$

where D has diagonal values:

$$D = diag\left(\frac{\sigma_i^2}{\sigma_i^2 + \alpha} \cdot \frac{1}{\sigma_i}\right) \qquad\qquad (26)$$

## 3.4 Conclusion

In this chapter, two EIT hardware systems being used for experiments throughout the thesis have been proposed. One is a 32 channel EIT hardware design using LabVIEW software and NI DAC and the other is a commercial EIT system called KCHU Mark2. Also, EIT theory including the forward and inverse problem is described, and some well-known image reconstruction algorithms have been introduced.

# Chapter.4 EIT Phantom fabrication and modelling

## 4.1. Phantom design

The first designed phantom is a 2D circular phantom consisting of 32 rectangular electrode plates (Figure 15). The electrodes are curved and fixed at the top of the tank. The phantom is constructed using a cylindrical plastic pipe with a square board fixed at the bottom. As shown in the engineering drawing, the diameter of the pipe is 23cm and the height is 16cm. The phantom is built with long electrodes with dimensions of 2.5 x 16cm and 0.2mm thickness. Pitch between each electrode is 2cm. The electrodes are made of steel (conductivity of approximately $1.3 \times 10^6$ s/m) which may not oxidize fast as compared to copper and aluminium.



23 cm

16 cm
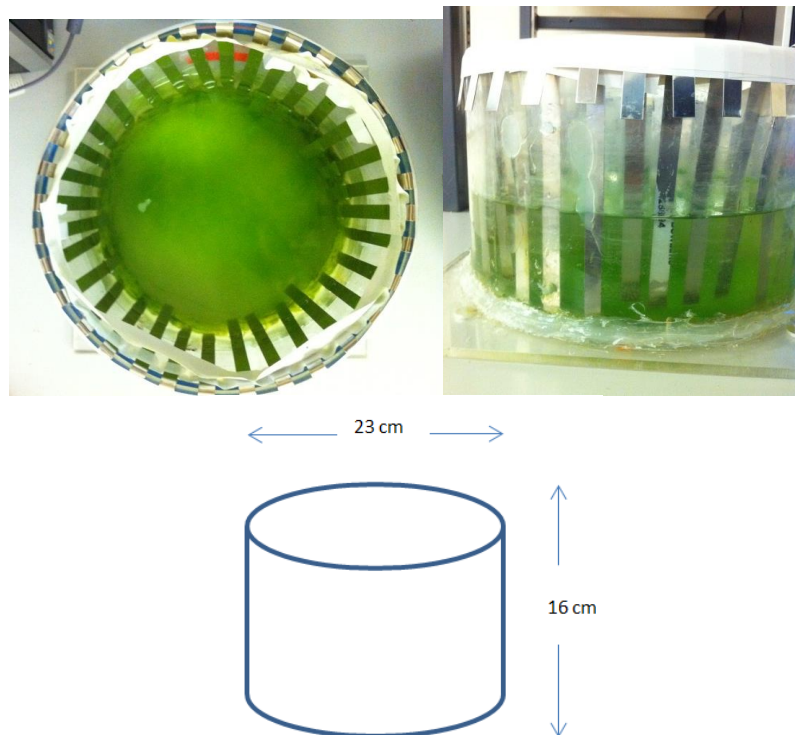
*Figure 15: A 32 channel 2D EIT phantom (picture and engineer drawing)*

A square fabric sensor has been built (Figure 16). The sensor consists of 3 main parts: a wooden frame, the fabric material and the electrodes. The frame

is constructed from two wooden plates with one on the top of the fabric and the other at the bottom. The sensor is a square shape with side length of 35cm. 32 identical copper electrodes (conductivity of approximately $58.5\times10^6$ s/m) with size of 1.5 x 2cm and thickness of 0.2mm are placed with 2.5cm pitch between each other. 16 bolts are used to hold the position of the electrodes.
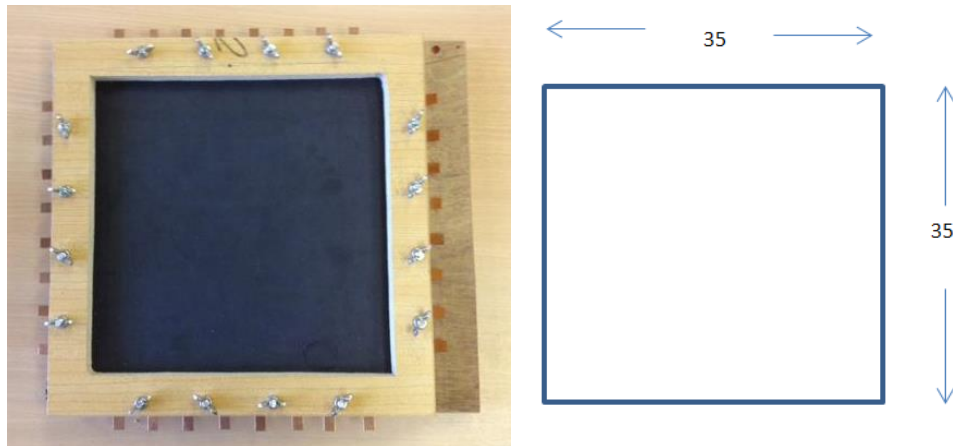


*Figure 16: Square fabric sensor (picture and engineer drawing)*

In order to test the 32 channel EIT hardware performance, a relative 3D test phantom needed to be built. The basic structure of the phantom is a 20 x 30cm plastic tube, with another plastic plate sealed at one end of the tube [97]. The electrodes, size 5 x 8cm, are cut from aluminium plates (conductivity of approximately $36.9\times10^6$ s/m) with thickness around 0.2mm. Holes are drilled equally spaced (2cm) in each layer and the gap between the two layers is 12cm. Electrodes have been curved at an angle to fit the circular tank. Screws are used to hold the electrodes in position and also act as connectors to the wiring system. Washers are inserted in each screw and silicon is used to seal any gap between the electrodes and the holes. Figure 17 shows the top and side view of the completed phantom.
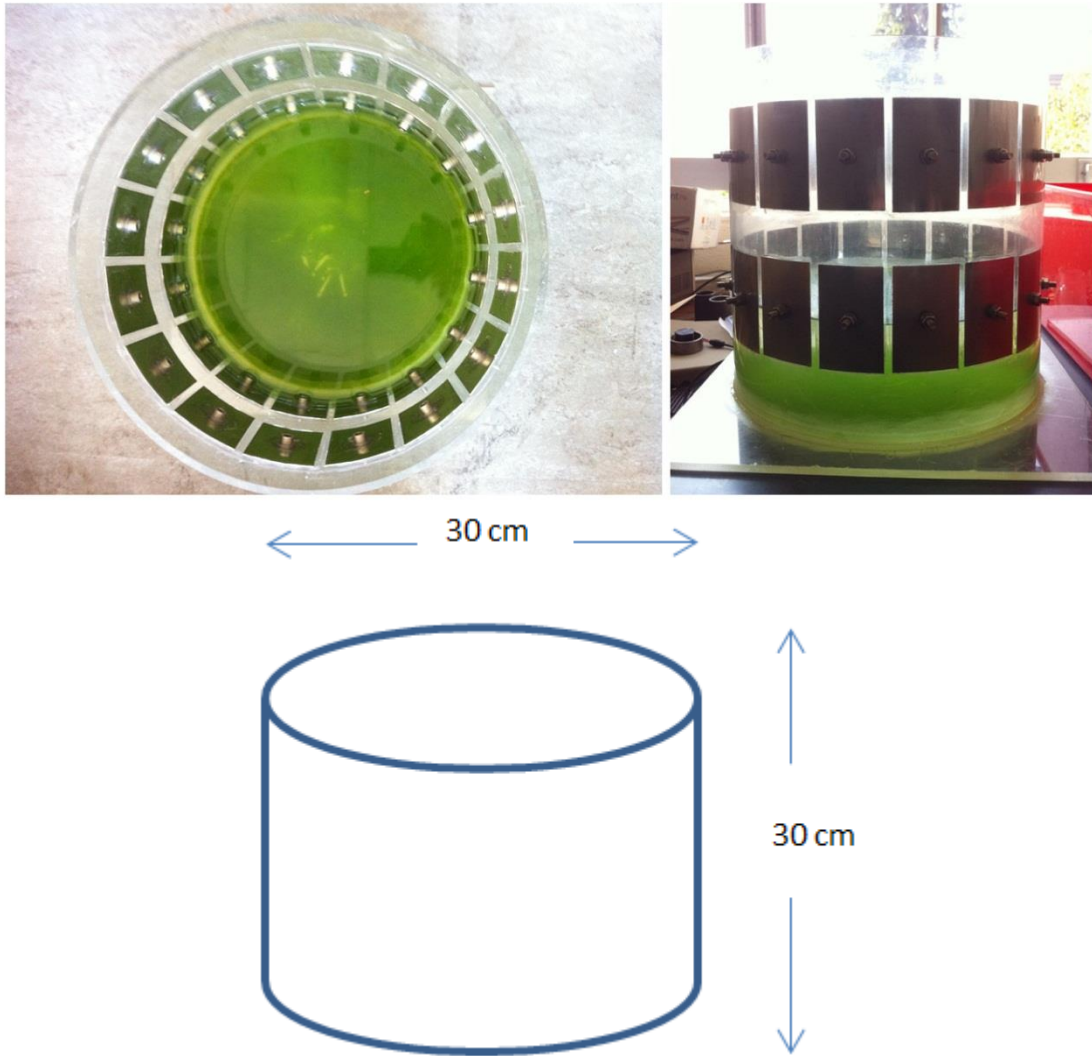
*Figure 17: Top and side view of the 32 channel system (picture and engineer drawing)*

Figure 18 shows the newly built planar array sensor. It is a square shape 3D phantom with width 14cm and height 25cm. Circular shape electrodes (radius = 5cm, thickness=0.2mm) are attached in two sides of the phantom. The distance between each electrode is 2.5cm. Each side consists of 16 electrodes.
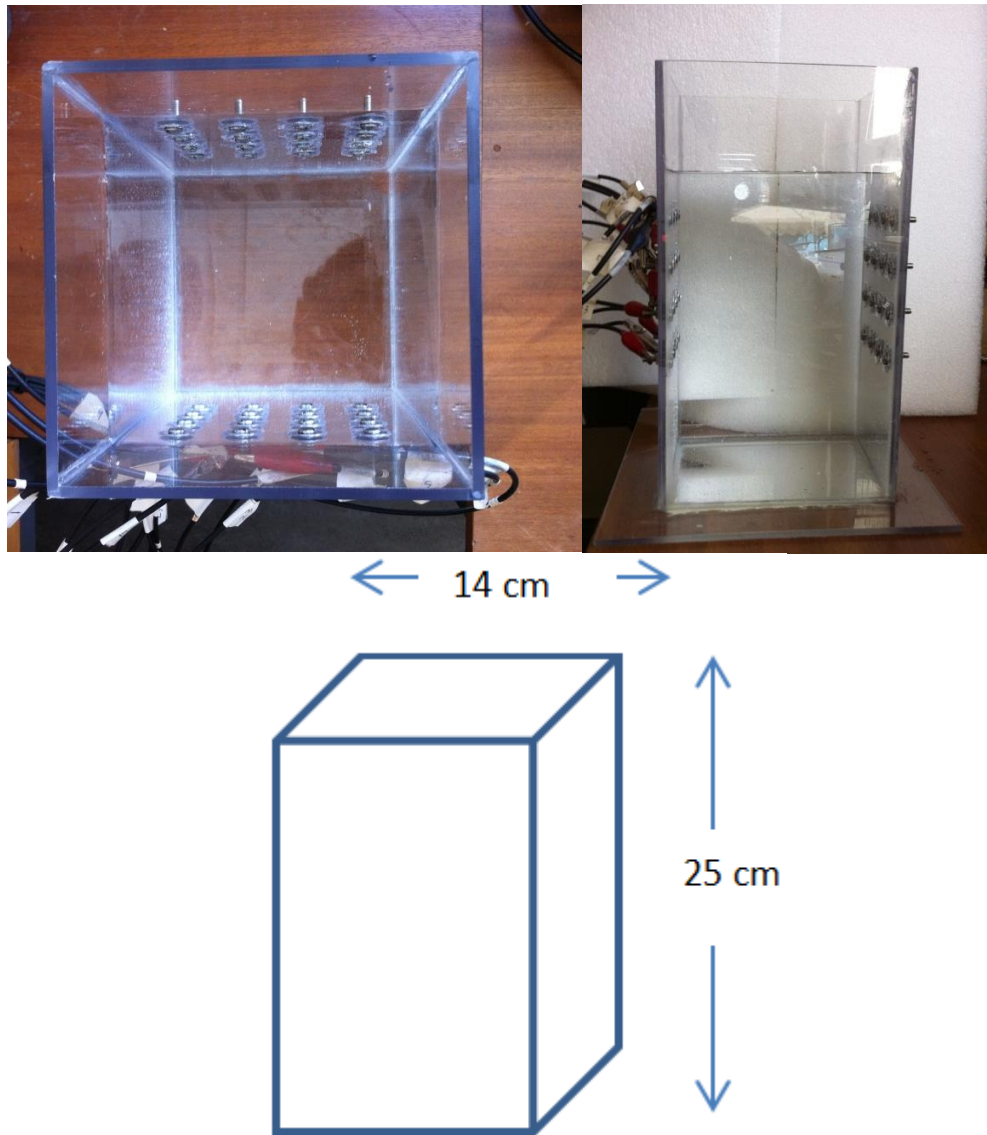
*Figure18: Plane array EIT phantom (picture and engineer drawing)*

## 4.2.    Phantom modelling

To solve Equation 6 with the complete electrode model, a finite element method (FEM) has been used [72, 98]. Considering that the FEM has the advantage of a building model for objects in any shape and handling inhomogeneous material properties, it is adopted here to solve the forward problem of the 3D EIT [39]. Finite element methods calculate the approximate solution for potential difference and conductivity. They convert the body under investigation into number of elements called finite element mesh.

EIDORS provides code for generating an FEM model for most typical EIT models. The meshing is done by a software named Net-gen. The function calls Net-gen automatically. Several parameters have to be decided for accurate meshing, which are:

- Type of model (circular, rectangular or others)

- Number of electrodes

- Number of planes

- Electrode size (width, height)

- Tank size (width, height)

- Electrode position (centre height)

- Mesh density.

Two by eight electrode model and two by sixteen electrode model are the most commonly used 3D EIT systems for both experimental validation and algorithm testing. In this research, two FEM models are mainly required. One is a basic 32 channel 3D EIT model. The other FEM model, which consists of four planes of 32 electrodes, would be used to evaluate the performance of the reconstruction algorithm developed for large scale EIT problem later on. The two meshings are shown in Figure 19.
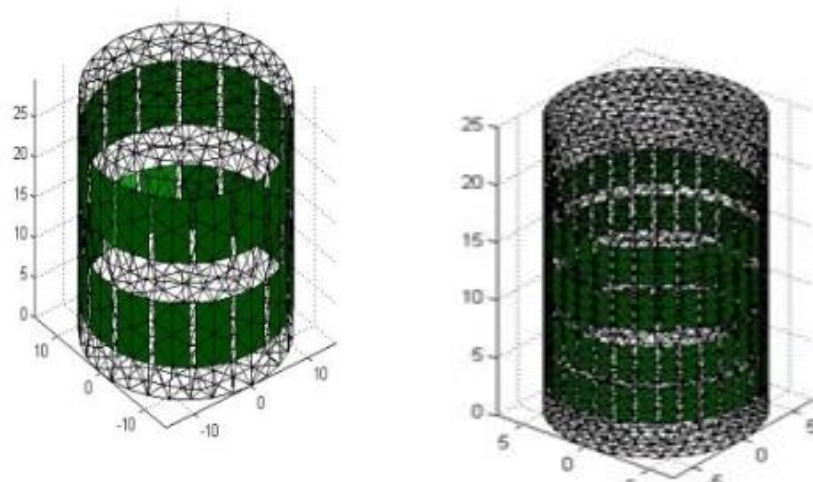


*Figure 19: FEM of a 32 electrode EIT system and a 128 electrode model*

A mesh for a 4 by 4 electrode plane array EIT is also required in the research (Figure 20).
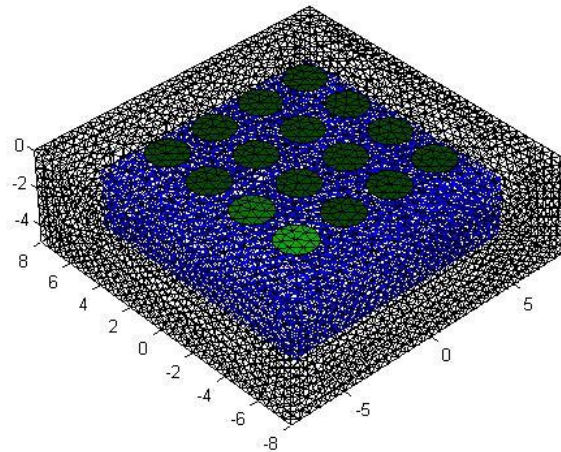


*Figure 20: Finite element mesh of 4x4 surface electrode EIT model*

Net-gen can also generate more complex geometries, such as a human thorax model shown in Figure 21, which can be used to simulate lung images.
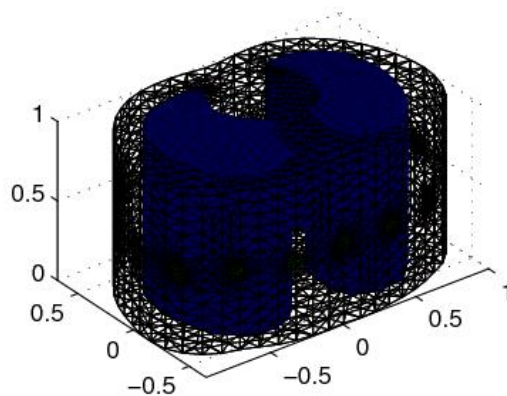


*Figure 21: Meshing of a 3D human thorax model with lungs*

## 4.3    Phantom tests

In order to avoid most experimental errors, several test constraints have to be considered:

- Equal measure of saline solution used for all tests

- Same image reconstruction software

- Data acquisition parameters such as sampling rate and number of samples are maintained throughout all systems

- Test objects are placed in the same locations in the phantom for image reconstruction

- Repeated tests to eliminate the experimental anomalies.

## 4.4.    Reconstruction images and discussion

Figure 22 shows the reconstruction results of the 32 channel 2D circular EIT system. Each reconstruction image is referred to a location picture that shows the exact position of the actual inclusion within the test phantom. Notice the regions showing in the reconstruction which have exceeded the tank size and would not be taken into account.
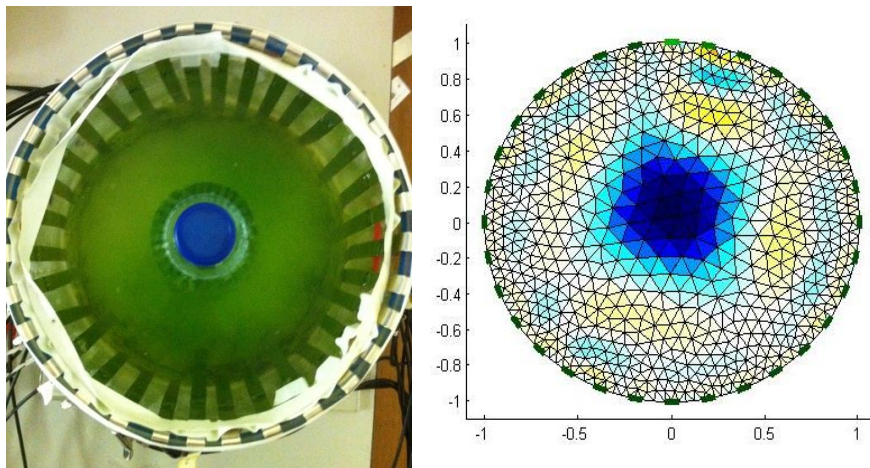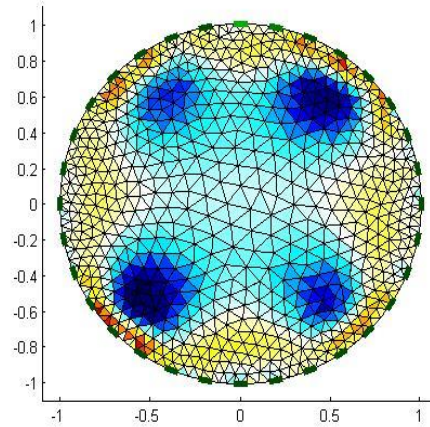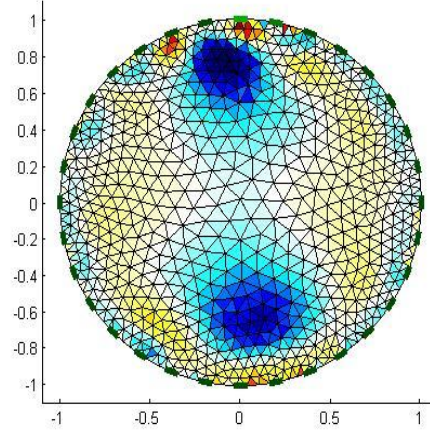
*Figure 22: Experiment reference location pictures and reconstruction results of 2D phantom*

Figure 23 shows the reconstruction results of our square fabric sensor.
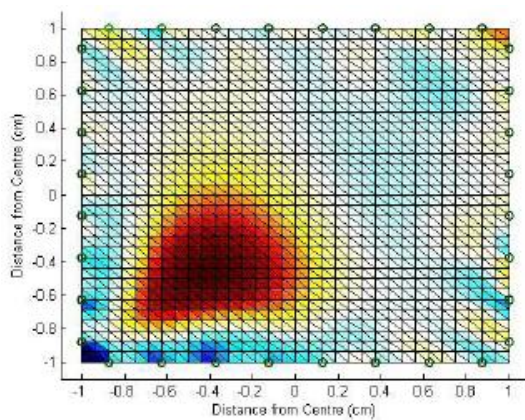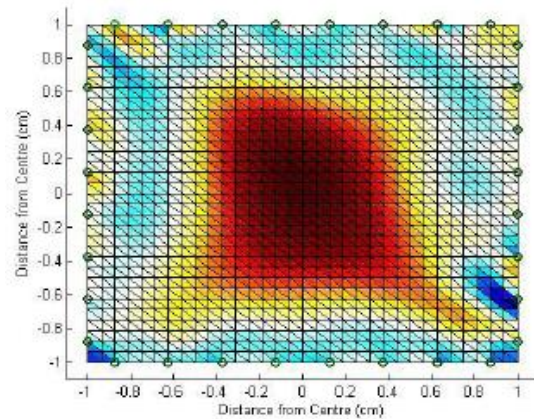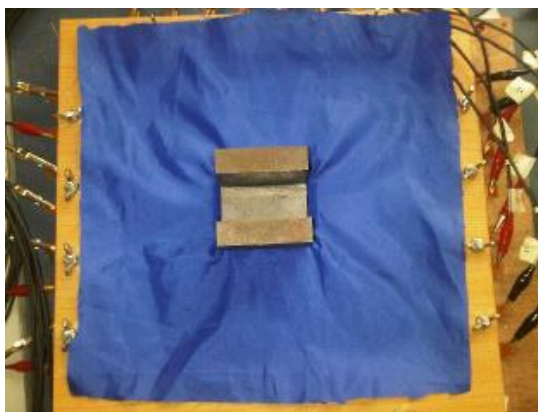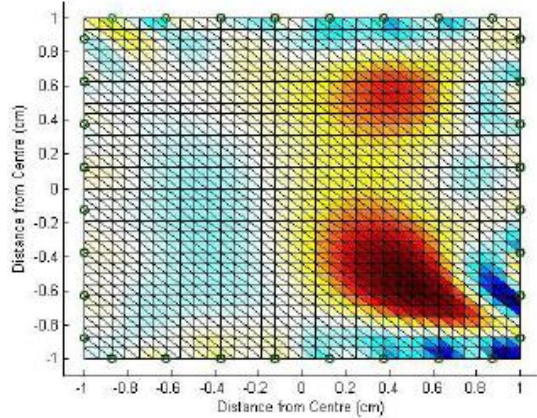
*Figure 23: Experiment reference location pictures and reconstruction results of the fabric sensor*

For our 3D phantom, experiments were performed for three different cases (shown in Figure 24). As potential changes occur more obviously when an object with a different conductivity is placed close to the electrodes, the most difficult reconstruction task for a single inclusion would be placing the object in the centre position. In the first case, a plastic cylinder with radius 2cm is inserted and the result is indicated. Secondly, two plastic cylinders (one solid with radius 2cm and one hollow with radius 1.5cm) are placed side by side close to the electrodes. In the third experiment, two bottle cans are used as samples and are placed at different heights inside the tank (one is near a side at the top and the other is at an opposite position at the bottom). This test is best for proving the 3D performance as it shows the reconstruction in both electrode layers.
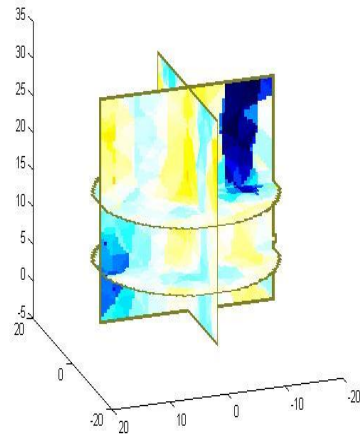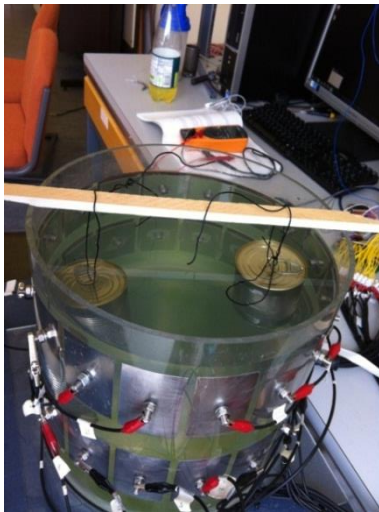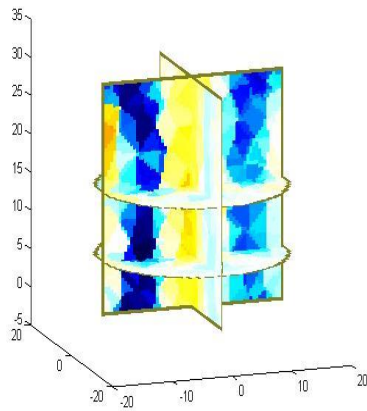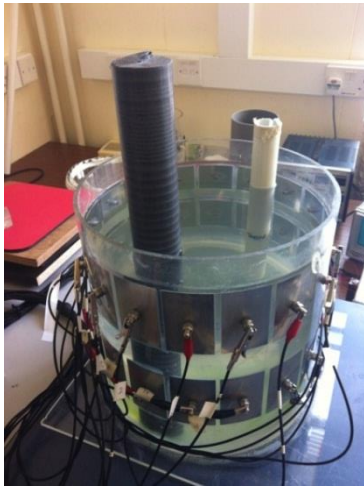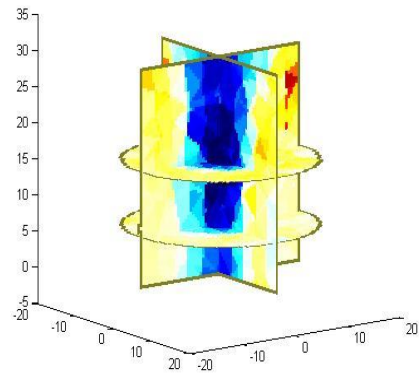
*Figure 24: Experiment reference location pictures and reconstruction results of 3D phantom*

## 4.5. Data analysis of EIT measurements

In order to perform difference imaging, the measurement has to be recorded twice; one is for the background data reading, and the other is for the measurement with test sample included. Figures 25, 26 and 27 show the background data reading of the three different EIT phantom designs.
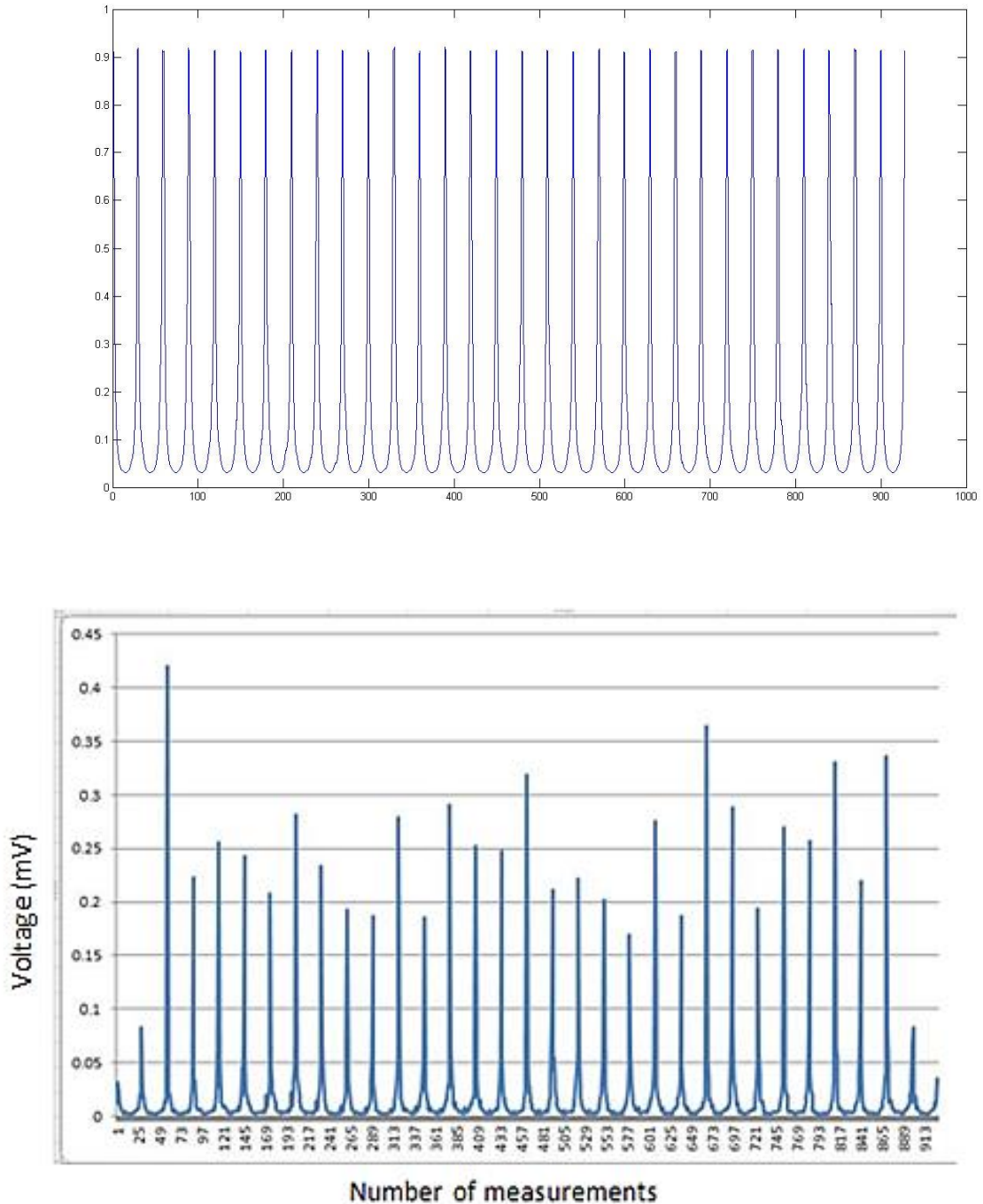


*Figure 25: Background reading of the 32 channel 2D phantom (simulation and real data)*
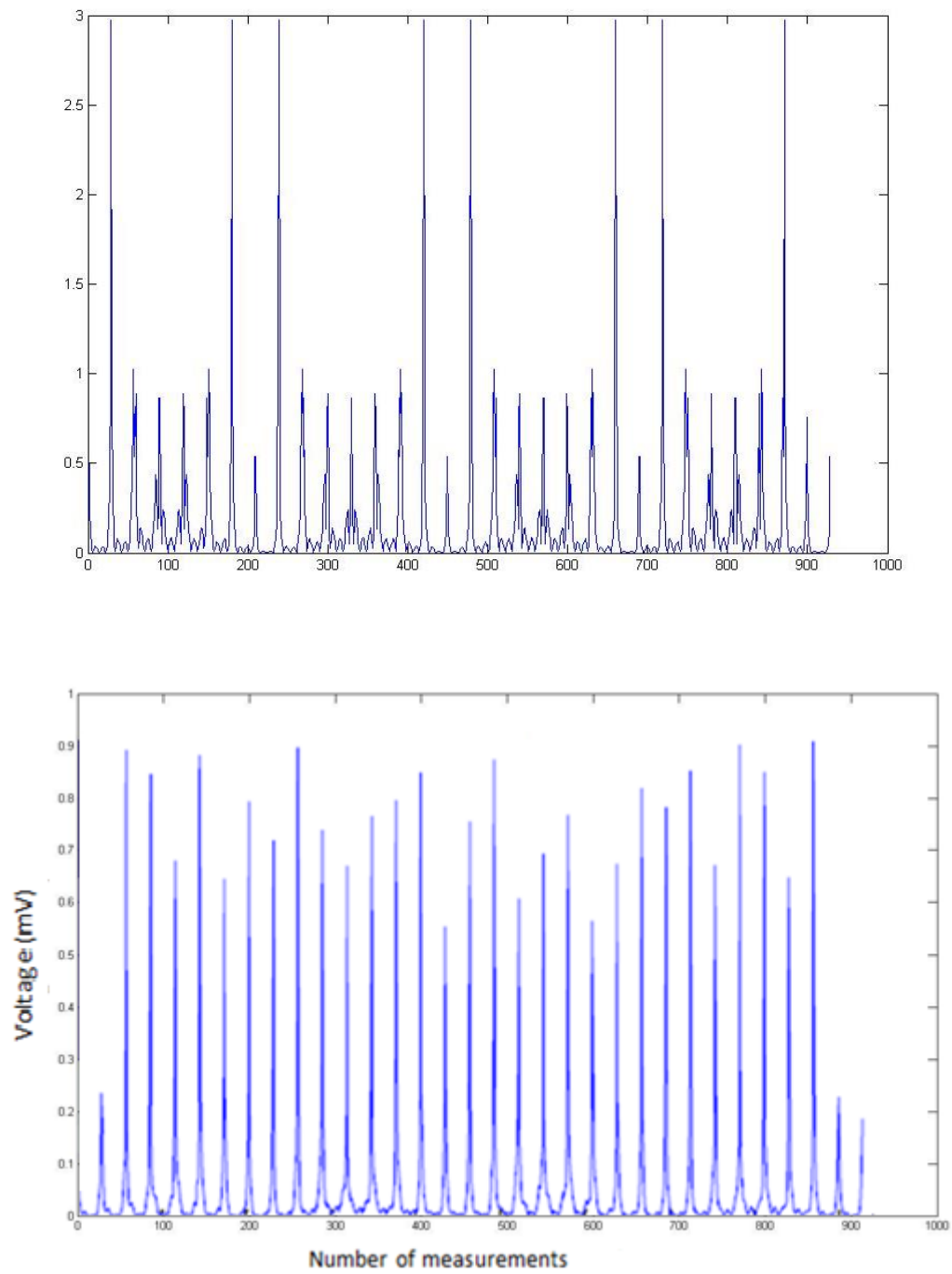
*Figure 26: Background reading of the square fabric sensor (simulation and real data)*
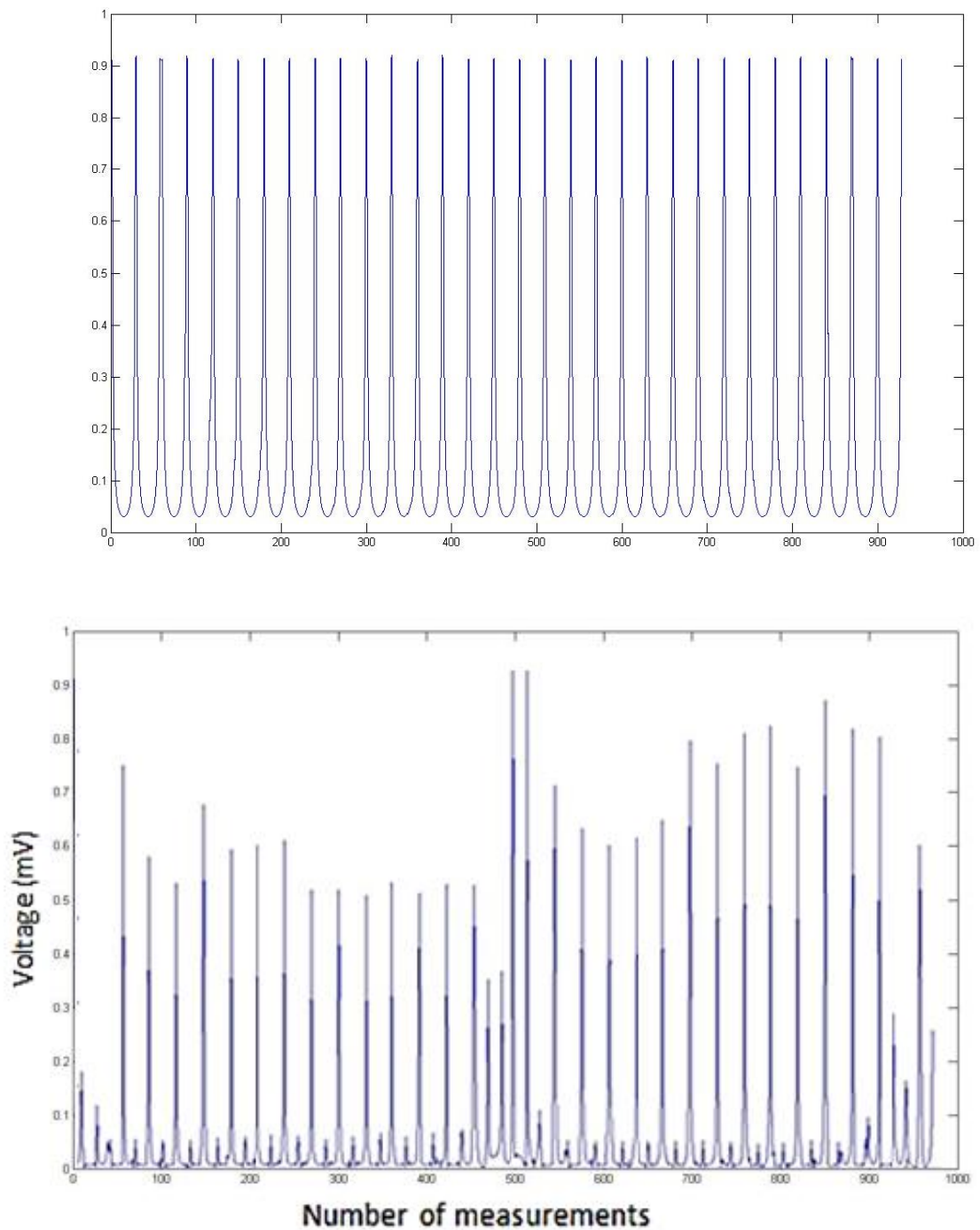
*Figure 27: Background reading of the 32 channel 3D EIT system (simulation and real data)*

Overall the system performed well and provided good "U shape" data in all three different phantom data collections. There is a little distortion when the signal is small; this may cause by the system noise.

## 4.6.    Conclusion

A variety of meshings for different types of EIT sensor have been demonstrated including a 2D tank sensor, a square fabric sensor and also a 3D tank sensor. Also several experiments have been done using different EIT phantoms. In the next section a special reconstruction technique to improve the performance of EIT when dealing with large number of measurements will be presented.

# Chapter.5 Sparse Jacobian and parallel computing in 3D EIT

Although EIT is a fast and simple imaging technique compared with other tomography methods like CT and X-ray, there is still great interest in optimising the computational performance of EIT image reconstruction while maintaining the image quality. This chapter describes a method for obtaining benefits on computer memory and time saving.

## 5.1 Background

The back projection reconstruction algorithm is a traditional method that provides fast and accurate results for a typical 16 electrode EIT system. However, an idea has been created such that if the number of electrodes is increased, making the system become larger in scale, such as a 128 electrode system, then a large number of measurements and pixels [99, 100] would be obtained. As a result of increasing the density of the sensitivity distribution, then the problem might become similar to a CT problem, which would potentially increase the image quality. Limitations appear to the traditional back projection reconstruction algorithm when facing a large scale 3D EIT problem as a great deal of information needs to be stored and calculation of the Jacobian matrix becomes unfeasible. A new reconstruction technique combining the Block-wise conjugate gradient method and sparse matrix simplification is developed to overcome these problems. The new combination reconstruction technique has significant advantages in the computational time of large scale EIT reconstruction without decreasing the image quality.

In the chapter, three dimensional EIT [101, 102] is taken into consideration. Increasing the number of electrodes will increase the number of independent measurements. This increase will provide more impedance information to the measurements [103, 104]. Theoretical consideration for information content in EIT data has been presented in [105], which provides a good guideline for selection of the number of electrodes. For EIT in 3D, the information required extends to multiple layers; a large number of electrodes could mean better

coverage of 3D space. If the number of electrodes increases to 128 (e.g. 4 planes of 32 electrodes), the number of independent measurements is 8000, and with 256 electrodes (e.g. 4 planes of 64 electrodes) the number of measurements is as high as 32384.

With a priori knowledge of the conductivity distribution, one can reduce the size of the inverse problem (number of voxels or degrees of freedom used in the image reconstruction) [106]. Assuming there is no prior knowledge about the conductivity distribution, then a large number of voxels is needed for the inverse problems. When the problem of a large number of electrodes and a large number of voxels happens, limitations appear as large size matrices need to be stored and large matrix inversions are required. In EIT each row of the Jacobian matrix represents the sensitivity of one measurement with respect to all voxels. In 3D EIT the values of the Jacobian matrix in each row have a very large dynamical range, making some of the voxels almost in-sensitive to a particular measurement.  In this chapter the Jacobian matrix is reduced to a sparse matrix by setting very small values to zero. Sensitivity of a given measurement to some voxels can be very low and here this very small value is set to zero. Conjugate gradient methods are well suited for such a large scale inversion. In this chapter, a new reconstruction technique has been proposed by combining the Block-wise conjugate gradient method and sparse matrix reduction to the Jacobian matrix to overcome the computational and memory problems in large scale 3D EIT. Adjacent current measurement patterns were used in all tests.

## 5.2.    Sparse Jacobian and threshold limits

Due to the nature of 3D EIT, the sensitivity of the measurements to conductivity changes far from field of view of the relevant electrode pair can be very small. These values from the sensitivity map would appear to be close to zero. The zero elements still remain in the matrix, which takes up memory and means they are used in the inverse calculation. The sparse matrix reduction method indicates that values which are very small, typically below a certain threshold, can be located and transformed to zero. These zero elements are then eliminated from the Jacobian matrix. This effect would decrease the total number of non-zero elements of the Jacobian matrix and hence reduce the

memory storage. Figure 28 shows an example of the effect after thresholding. Level of sparsity (LOS) is defined as the number of non-zero elements divided by the total number of elements in the matrix.
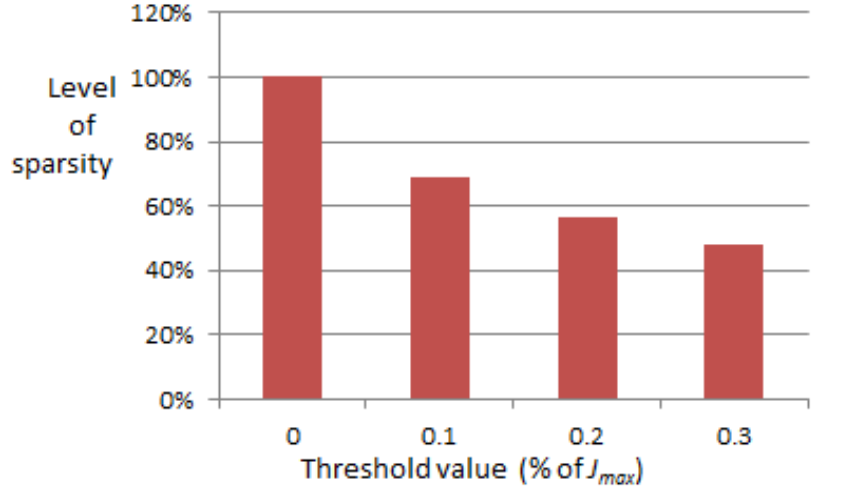


*Figure 28: Histogram of the level of sparsity of Jacobian for a 32 channel system*

The new Jacobian $J_k$ after being sparsed is then formed:

$$J_k = \begin{cases} J_{ij} & if \quad \sum_{i=1}^{nm} J_{ij} \geq threshold \\ 0 & if \quad \sum_{i=1}^{nm} J_{ij} < threshold \end{cases} \qquad (27)$$

where *j* corresponds to the element number within the domain and *nm* denotes the number of measurements. The Jacobian matrix $J_k$ now contains a large number of zero values. This study investigates the reduction of the memory usage of the Jacobian by comparing the non-zero elements and the suitable value for thresholding. Two ways to define the threshold value were considered. One is to make the threshold to be a small percentage t of the maximum value of each row of the Jacobian matrix (*t* is a small percentage value, e.g. 0.01%).

$$J_k = \begin{cases} J_{ij} & if \quad \sum_{i=1}^{nm} J_{ij} \geq t \% \times J_{max} \\ 0 & if \quad \left| \sum_{i=1}^{nm} J_{ij} \right| < t \% \times J_{max} \end{cases} \qquad (28)$$

The second way of thresholding is that the threshold can be $t\%$ of the average value of a sum of $n_m$ biggest numbers in each row of the Jacobian matrix. Let the sum of a list of $h$ biggest values in a row of the Jacobian be $\sum J_{\max(h)}$, then:

$$
J_k = \begin{cases} J_{ij} & if & \sum_{i=1}^{nm} J_{ij} \geq t\ \% \ \times \ \overline{\sum J_{\max(h)}} \\ \\ 0 & if & \sum_{i=1}^{nm} J_{ij} < t\ \% \ \times \ \overline{\sum J_{\max(h)}} \end{cases}
\tag{29}
$$

There might be some abnormal elements in the forward modelling mesh, which result in high values of sensitivity. The second method is used to avoid this and make the thresholding more accurate. Therefore, all tests in this chapter are made with the second thresholding method.

## 5.3. Block-wise conjugate gradient least square

### 5.3.1. Conjugate gradient

The main problem of large scale 3D EIT reconstruction is to solve the inverse problem involving a large dimensional Jacobian matrix $J$. Krylov subspace methods, especially conjugate gradient, are currently used for large scale 3D problems [107]. The Conjugate Gradient method is the most prominent iterative method to solve sparse systems of linear equations [42, 108]. Being fast and suitable to solve the inversion working with a large sensitivity matrix, Conjugate Gradient Least Square (CGLS) can be easily implemented on parallel processors [109]. This is an iterative method that generates a number of iterations, $x_k$ of successive approximations to the solution and residuals, $r_k = b - Ax_k$, and search directions, $P_k$, to update the iterates and residuals [110, 111]. It can be applied to sparse systems that are too large to be handled by direct methods.

An implementation of CGLS for the EIT problem can be expressed as follows:

$$
Jx = b
\tag{30}
$$

where $J$ is the sensitivity matrix obtained by the forward problem, x is the image and b is the measurement data.

The least square problem is to minimise

$$\|Jx - b\|$$

(31)

Since $J^T J$ is positive-definite for any matrix $J$, the conjugate gradient algorithm can be applied to the normal equations

$$J^T Jx = J^T b$$

(32)

Let $r_0 = b - Jx_0$ . The following loop shows the iteration of CGLS:

Loop start

$$a_{k+1} = \frac{\|J^T r_k\|^2}{\|Jp_k\|^2}$$

$$x_{k+1} = x_k + a_k p_k$$

$$r_{k+1} = r_k - a_k Jp_k$$

If ( $r_{k+1}$ < threshold)

Break;

Else

$$\beta_n = \frac{\|J^T r_{k+1}\|^2}{\|J^T r_k\|^2}$$

$$p_{k+1} = J^T r_{k+1} + \beta_n p_k$$

Repeat
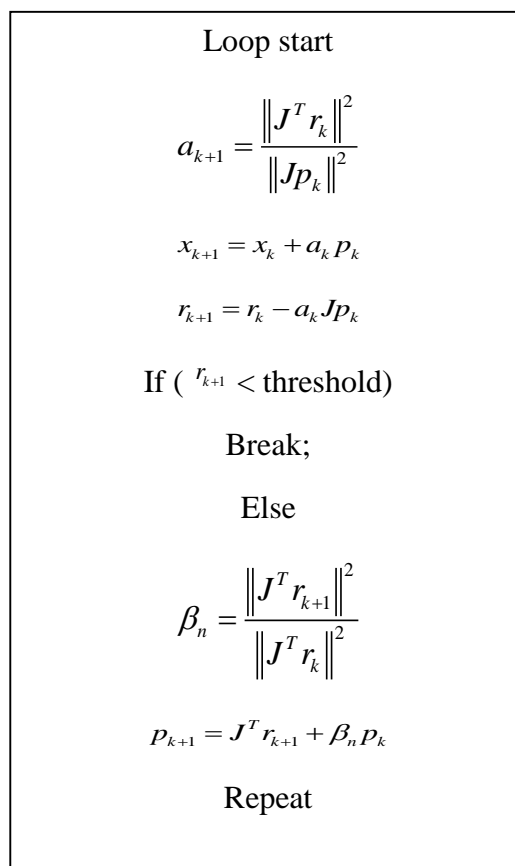
Algorithm1: Conjugate gradient method

where $r_k$ is the residual at the $k^{th}$ step and $p_k$ is an auxiliary vector of length n.

The loop approximates to the solution $x_{k+1}$ with the minimum residual error $r_{k+1}$. With CGLS, the number of iterations provides the effect of regularisation to the final reconstructed image. The number of iterations required depends on the

meshing size and scale of the problem (number of electrodes). Tikhonov regularisation can be applied to the Jacobian by adding a regularisation term:

$$\begin{bmatrix} J \\ \alpha I \end{bmatrix} \mathrm{x} = \begin{bmatrix} b \\ 0 \end{bmatrix}$$

(33)

where $\alpha$ is the regularisation parameter and *I* is identity matrix.

The CGLS iteration already has a regularization effect. Due to the computational aspect, the identity matrix is used here to make the inversion more stable and still be memory efficient. It is fully sparsed and becomes the last block of the matrix [112].

### 5.3.2. Block-wise matrix vector multiplication

A simulation for a 128 electrode system was firstly done to test the performance of the sparse Jacobian CGLS method. The algorithm was run in MATLAB using an 8GB RAM computer. However MATLAB could not handle the forward problem as an error message said out of memory. Assume there is no other background usage of memory, the PC would provide a fully virtual memory of 8GB to MATLAB and MATLAB itself does not limit the memory usage. This indicated that the current computer storage capacity (RAM) may not be sufficient to process and store a full Jacobian matrix in the 3D EIT problem with a large number of measurements. The block-wise matrix method suggests that one can separate the Jacobian into blocks, and solve the inverse problem in a matrix free method as CGLS does not require access to the full matrix *J* [110]. Therefore all that is needed is a simple matrix vector multiplication with each of *J* and *J* per iteration. The matrix *J* can be divided in to $l+1$ blocks (24a).

As described in the CGLS, two matrix multiplications are mainly considered, the $Jp$ multiplication and $J^T r$ multiplication. Therefore, the $Jp$ multiplication can be done in block-wise format (24b) where *p* is a vector with size *n* x 1. Similarly, in the $J^T r$ multiplication, r has a size of 1x (*m* + *n*) which can be partitioned into *l* + 1 blocks, shows in (24c), where each block has a dimension of $(m+n)/l$.

$$J_k = \begin{bmatrix} J_1 \\ J_2 \\ ... \\ J_l \\ J_{l+1} \end{bmatrix} \quad (24a) \qquad Jp = \begin{bmatrix} J_1 p \\ J_2 p \\ ... \\ J_l p \\ J_{l+1} p \end{bmatrix} \quad (24b) \qquad r_k = \begin{bmatrix} r_1 \\ r_2 \\ ... \\ r_l \\ r_{l+1} \end{bmatrix} \quad (24c)$$

where $k = 1, 2, 3 \ldots l, l+1$, each block $J_k$ has a dimension of $m/l$ by $n$ and $J_{l+1}$ is the $n \times n$ regularised identity matrix used for Tikhonov regularisation. From (10c), $J^T r$ can be expressed as the sum of all $J_k^T r_k$ blocks,
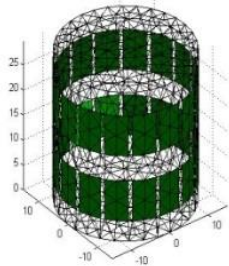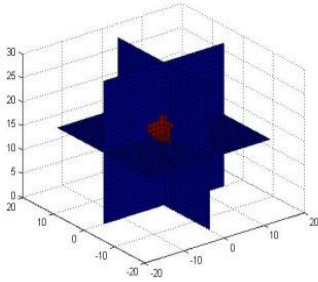
$$J^T r = \sum_{k=1}^{l+1} J_k^T r_k \qquad (34)$$

Each block-wise sensitivity element $J_k$ can be loaded at the same time and matrix multiplication steps can be done in parallel using computers with multiple cores. This will improve the reconstruction speed significantly.

## 5.4. Results

### 5.4.1. Simulation results

Simulations are initially done using the 32 channel system to test the feasibility of the sparse Jacobian CGLS algorithm and also to measure the optimum threshold value. The simulations are done using a desktop computer with an 8 core CPU and 4GB RAM. For the 32 electrode model, which gives 928 measurements, the sensitivity map has been partitioned into 58 segments. All reconstructions are done in parallel execution with 7 cores. The results are shown in Figure 29. The mesh has parameters of tank height=30cm, tank width=15cm, electrode height=8cm, electrode width=5cm.



| 32 electrodes EIT system meshing | True image( a sphere with radius=4cm in the centre) |
|---|---|

| | |
|---|---|
| Original reconstruction(200 iterations)<br><br>LOS=100% | Threshold= 0.1%*$\overline{\sum J_{\max(100)}}$<br><br>LOS=88.54% |
| Threshold= 0.5%*$\overline{\sum J_{\max(100)}}$<br><br>LOS=66.81% | Threshold= 1%*$\overline{\sum J_{\max(100)}}$<br><br>LOS=52.90% |
| Threshold= 2%*$\overline{\sum J_{\max(100)}}$<br>LOS=38.08% | Threshold= 5%*$\overline{\sum J_{\max(100)}}$<br>LOS=22.93% |
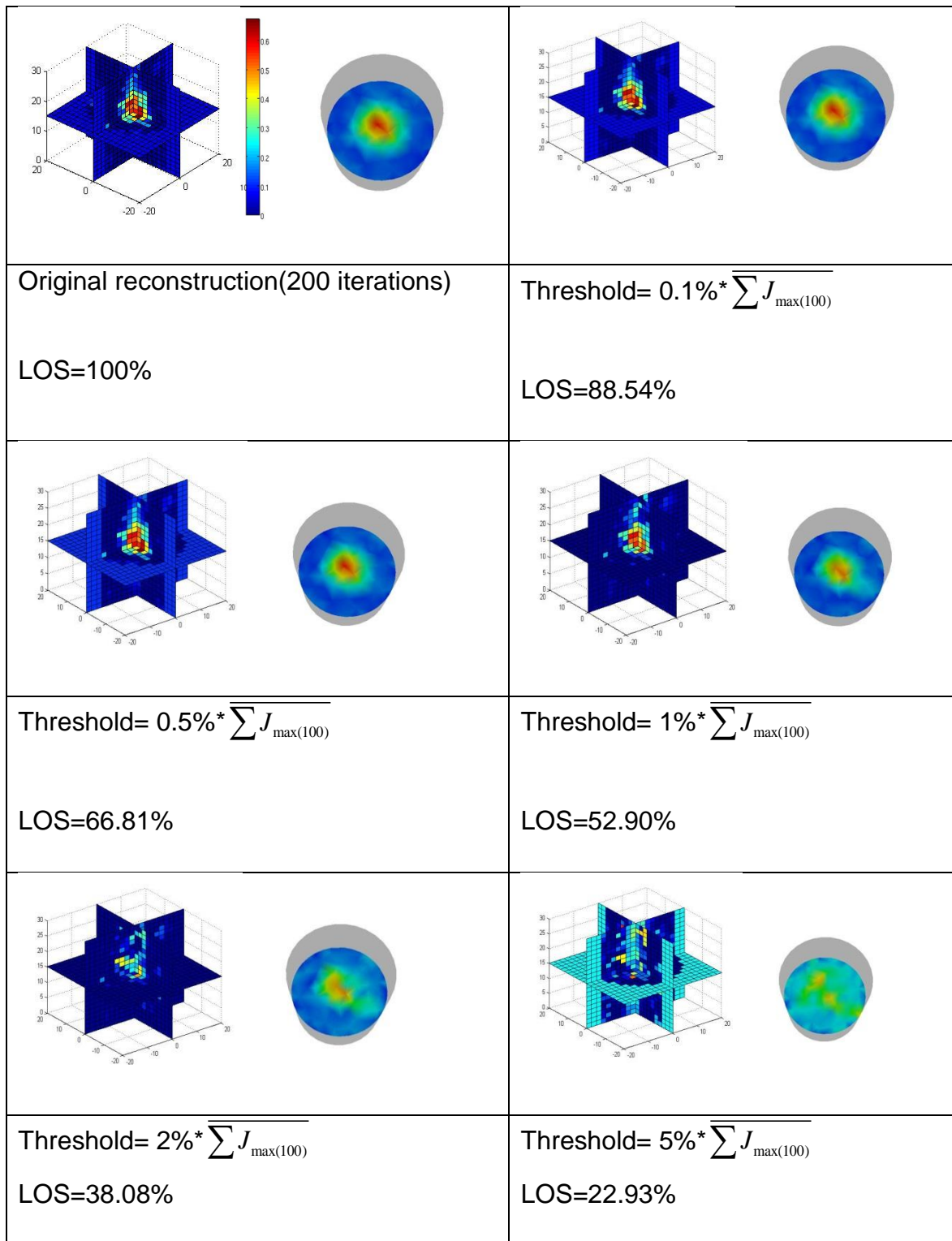
*Figure 29: Simulation results of 32 channels EIT system*
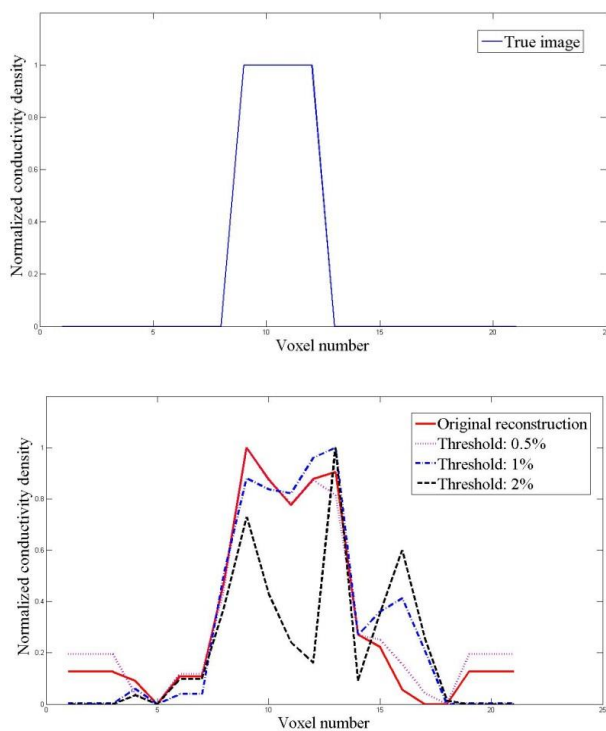
*Figure 30: 1D plot of normalized conductivity distribution against number of voxels*

Table 2: Image quality measures based on GREIT (32 electrode simulation case)

| Threshold value | AR(Amplitude response) | PE(Position error) | RES(Resolution) | SD(Shape deformation) |
|---|---|---|---|---|
| Original | 38 | 10.9, 13.9 | 0.1053 | 9 |
| 0.1% | 38 | 10.9,13.9 | 0.1053 | 9 |
| 0.5% | 33 | 10.87,14.15 | 0.0914 | 15 |
| 1% | 22 | 10.63,11.31 | 0.0609 | 4 |
| 2% | 12 | 10.87,14.15 | 0.0332 | 15 |
| 5% | 11 | 10.89,13.97 | 0.0305 | 18 |

The performance of thresholding in a critical case was evaluated, which is by inputting a spherical inclusion in the centre of the imaging area. Since it is very difficult to observe the degradation of the image quality directly from the reconstructed images, a 1D plot of normalized conductivity was used to compare the image qualities of different threshold values. For image visualisation a 21 x 21 x 21 3D grid is used. Figure 30 shows the 1D graph using the 32 channel simulation case and is a line from plane z=11 and along a line of y=11. It can be observed that the image quality remains up to a limit where the threshold value is equal to approximately 1% of the average of the maximum 100 values. After that point distortion starts to occur in the image region. Further simulation shows that the image quality is lost significantly when a threshold value of 2% is applied. Therefore, the simulation results for the 32 electrode system show that a suitable threshold value would be up to 1%. This value of thresholding will be the maximum point that can provide satisfactory image information. Any other inclusion types and locations might have higher tolerance on the threshold percentage, but they will always produce satisfying images with thresholding between 0.1% and 1%, since the simulation is done in a critical case. From the ratio of the number of non-zeros in the Jacobian matrix and the total elements in the Jacobian matrix, the level of sparsity and the reduction in memory storage can be calculated. For an optimum thresholding of 1%, approximately 50% of total matrix elements are transformed to zeros and can be eliminated.

To further analyse the results, GREIT performance parameters [85] have been used to perform image quality measurement. Figure 31 shows a set of figures of merit to characterize the image qualities based on GREIT. Based on images of point targets, several figures of merit are defined: amplitude response (AR), position error (PE), resolution (RES), shape deformation (SD) and ringing (RNG). AR measures the ratio of image pixel amplitudes in the target in the background to that in the reconstructed image. It is considered to be the most important figure of merit in quality measures. PE measures the extent to which reconstructed images faithfully represent the position of the image target. RES measures the size of reconstructed targets as a fraction of the medium.

Reconstruction algorithms typically create circular images for the medium boundary. SD measures the fraction of the reconstructed one-fourth amplitude set which does not fit within a circle of the reconstructed area. This indicates shape changes of the objects near the medium boundary. RNG indicates whether reconstructed images show areas of opposite sign surrounding the main reconstructed target area. Constant AR is considered to be the most important figure of merit. PE is required to be small and constant compare with the original reconstruction image as a second important parameter. An increase in value of PE could mean more error obtained in reconstruction of the object location. A uniform RES would represent a more accurate shape of the target conductivity distribution as well as a uniform SD and is considered to be another important figure of merit. Large SD shows incorrect interpretation of images. A low and uniform RNG is important to indicate the correctness of conductive pattern inside the reconstruction region. Table 2 shows a set of figures of merit to characterize the image qualities based on GREIT. It can be observed that some image information degrades as the threshold increases. It is suggested that there is a direct relationship between the LOS and image quality (image quality remained well while LOS is higher than 50%). Notice that GREIT is a new tool for measuring image quality by calculating several figures of merits; however it is not possible to simultaneously optimize all measures. Random measurement noise would occur which may effect on error calculation. Most of the parameters are expected to be similar to the parameters of true images, as quality goes down the difference becomes bigger. It is therefore a useful tool for analysing the performance of the sparse matrix algorithm.
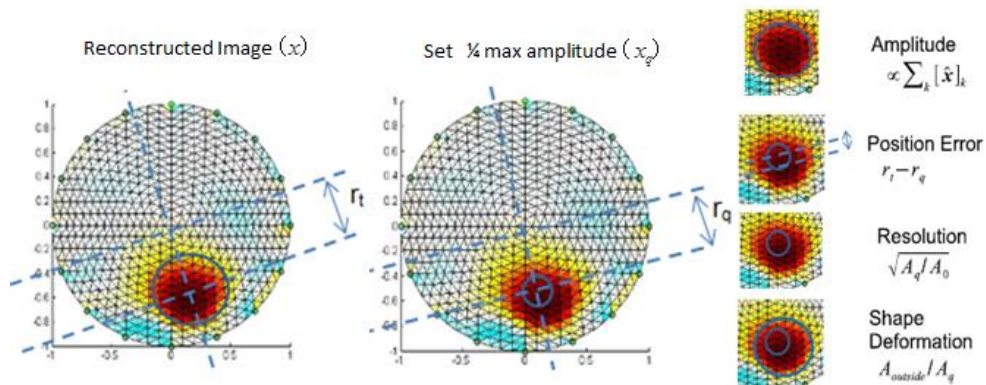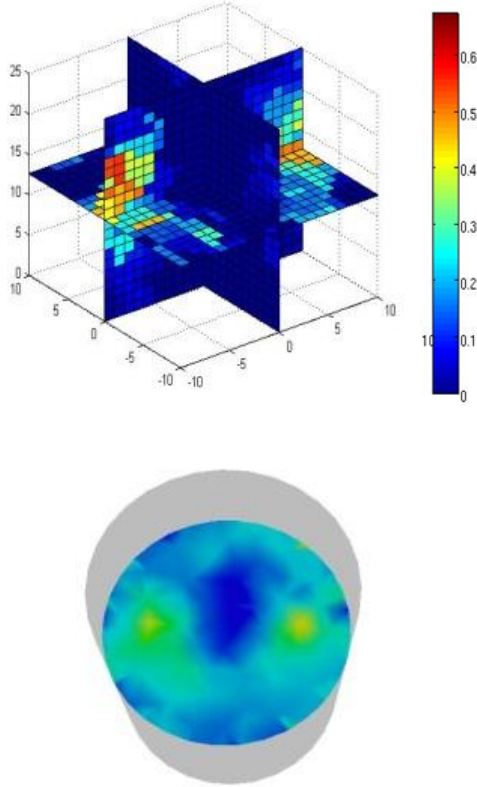


*Figure 31: Performance figure of merit for evaluation of GREIT images*

### 5.4.2. Experimental validation

In order to experimentally validate the programme performance, a LabVIEW based EIT system was built. The simple EIT system was developed using the National Instruments system for data acquisition and a multiplexer for channel switching. Details of the system are described in the hardware chapter.

Two metal cans with radius 2cm, height 10cm are used as inclusion in the experiment. They are located at two sides of the phantom and with a small height difference. Figure 32 shows the reconstruction images with various LOS in sparse Jacobian.

| | |
|---|---|
| |  |
| Phantom pictures | Original reconstruction(300 iterations)<br><br>LOS=100% |

| Threshold= $0.1\% * \overline{\sum J_{max(100)}}$ | Threshold= $0.5\% * \overline{\sum J_{max(100)}}$ |
|---|---|
| LOS= 88.54% | LOS=66.81% |

| | |
|---|---|
| Threshold= 1%*$\overline{\sum J_{max(100)}}$<br><br>LOS=52.90% | Threshold= 2%*$\overline{\sum J_{max(100)}}$<br><br>LOS= 38.08% |
| <br><br>Threshold= 5%*$\overline{\sum J_{max(100)}}$<br><br>LOS= 22.93% | |
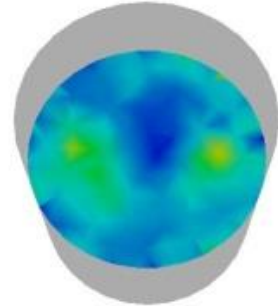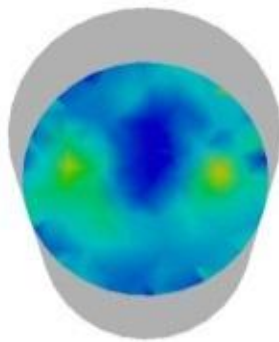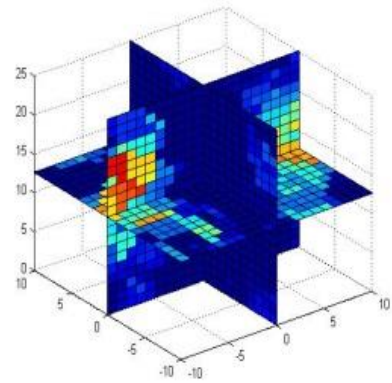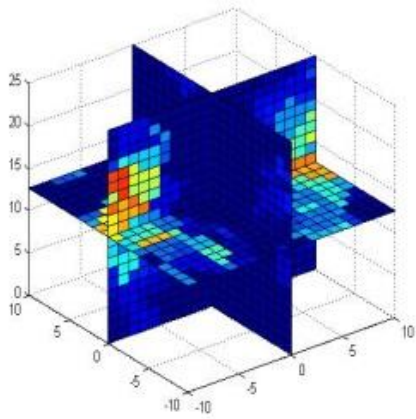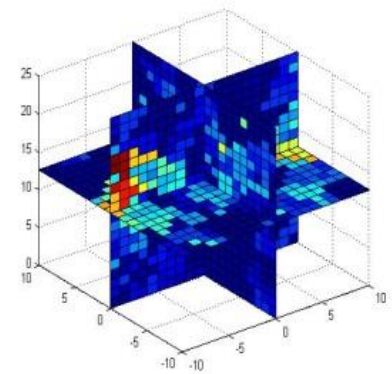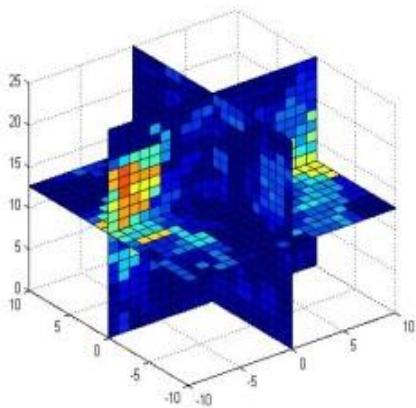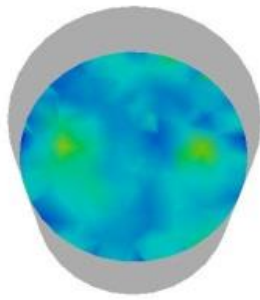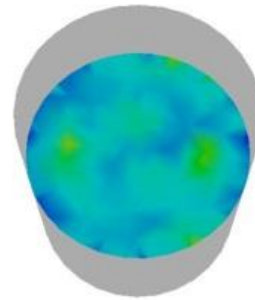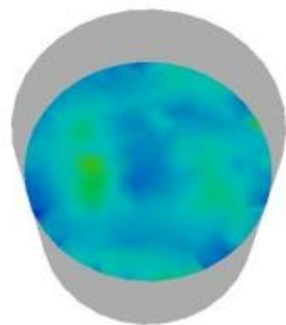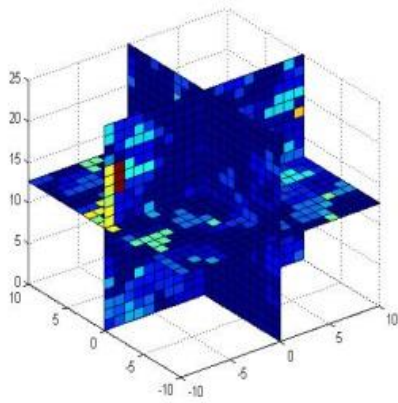
*Figure 32: Experimental results of 32 channels EIT system*

Table 3: Image quality measures based on GREIT (32 electrode real object case)

| Threshold value | AR(Amplitude response) | PE(Position error) | RES(Resolution) | SD(Shape deformation) |
|---|---|---|---|---|
| Original | 26 | 19.72, 10.72 | 0.0720 | 14 |
| 0.1% | 25 | 19.72,10.72 | 0.0693 | 12 |
| 0.5% | 21 | 20.27,10.72 | 0.0582 | 15 |
| 1% | 29 | 20.00,10.35 | 0.0803 | 22 |
| 2% | 53 | 19.42,9.84 | 0.1468 | 58 |
| 5% | 61 | 14.21,5.05 | 0.1690 | 80 |

### 5.4.3. Large scale data

Simulations are done to test the performance of the proposed algorithm on a 128 electrode system. A circular tank model of 32 electrodes by 4 planes is generated. The sensitivity map has been divided into 80 blocks, and the CGLS is operating with an iteration number of 400. Results are shown in Figure 33. The tank height=25cm, tank width=10cm, electrode height=3cm, and electrode width=1cm.
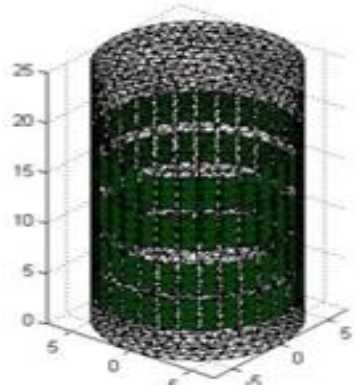
| 128 electrodes 3D EIT system FEM mesh | True image |
| --- | --- |
| | (A sphere with radius of 4cm) |



| Original reconstruction(400 iterations) | Threshold= $0.1\% * \overline{\sum J_{max(100)}}$ |
| --- | --- |
| LOS=100% | LOS= 45.87% |
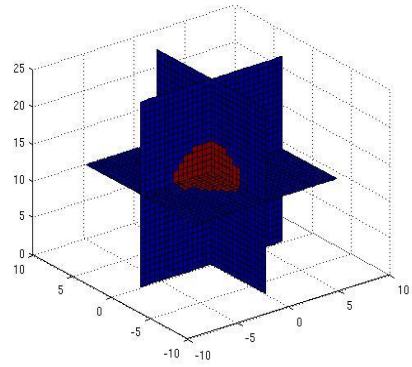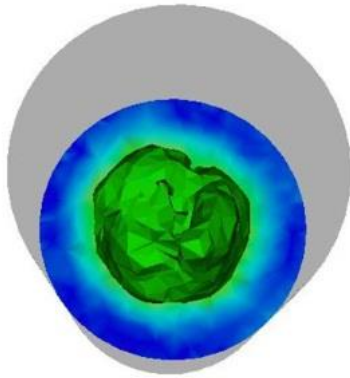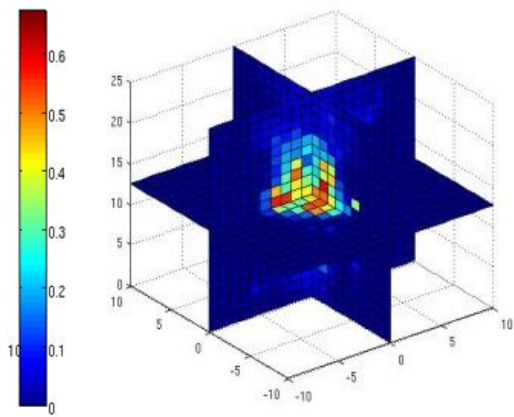
Threshold= $0.5\% * \overline{\sum J_{max(100)}}$

LOS= 36.36%
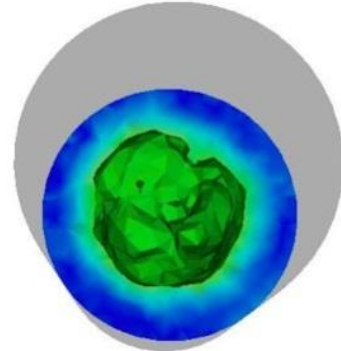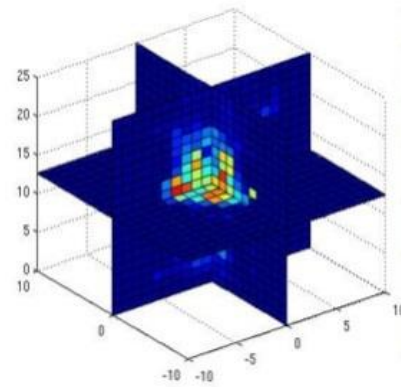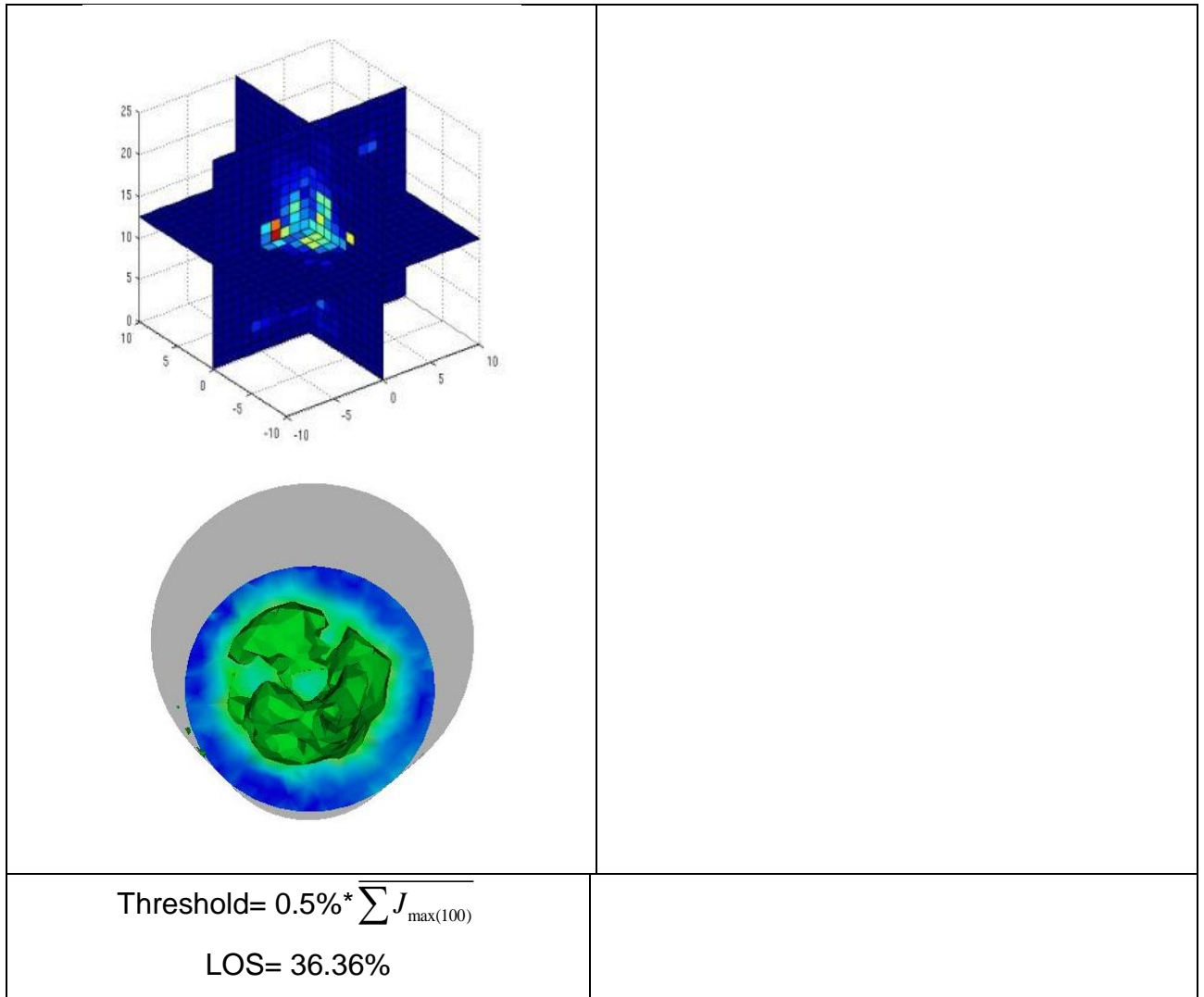
*Figure 33: Simulation results of the 128 electrode system*

Table 4: Image quality measures based on GREIT (32 electrode real object case)

| Threshold value | AR(Amplitude response) | PE(Position error) | RES(Resolution) | SD(Shape deformation) |
|---|---|---|---|---|
| Original | 39 | 11.11, 11.19 | 0.1080 | 23 |
| 0.1% | 32 | 11, 8.8.86 | 0.0886 | 37 |
| 0.5% | 26 | N/A | 0.0720 | N/A |

Table 5: memory requirement 128 electrode system with different threshold values

| Threshold value | 0 | 0.001 | 0.002 |
|---|---|---|---|
| Memory requirement for each block (bytes) | 18789600 | 15230176 | 13852576 |

Simulations are done in the same way as previous tests. The first threshold value was chosen to be 0.1%. It can be seen that LOS has dropped to 46% which is about the minimum point (50%) for the image quality to remain. A further experiment is done by increasing the threshold to 0.5%, which gives 36% LOS, and a significant drop in image quality can be observed from the reconstruction images and GREIT data. In 32 channel system reconstruction, a suitable threshold value of 1% is suggested, whereas a threshold of 0.1% is optimum in this case. The reconstructions between 32 and 128 channel systems show the same pattern, as LOS below 50% will dramatically reduce the image quality. This indicates that a suitable threshold value can be obtained while LOS is at 50%, but this value is different in various scales of problem.

## 5.5. Computational time

Partitioning the sensitivity matrix $J$ into a number of blocks enables the block-wised matrix calculation to be operated in parallel given a multiple core computer, which will further enhance the calculation speed. Tables are generated to indicate the improvements:

Table 6: Time performance comparison of a 32 channel simulation EIT system

|  | Original reconstruction | Threshold =0.1% | Threshold =0.5% |
|---|---|---|---|
| Serial reconstruction | 51.13s | 51.77s | 51.46s |
| Parallel reconstruction (7 cores) | 27.77s | 26.94s | 27.07s |

Table 7: Time performance comparison of a 128 channel simulation EIT system

|  | Original reconstruction | Threshold =0.1% | Threshold =0.5% |
|---|---|---|---|
| Serial reconstruction | 8291.07s | 6973.24s | 5936.98s |
| Parallel reconstruction (7 cores) | 1527.90s | 1283.68s | 1136.06s |

As shown in Table 6, there are small improvements on serial reconstruction when thresholding is used for small scale problems. Similarly, parallelisation shows little improvement on small scale problems. For large scale problems the improvements become significant (Table 7). The reconstruction time decreases dramatically as the thresholding is applied. And for parallel implementation the computational time has become almost 7 times shorter than the serial method. By increasing the number of CPU cores the program can further achieve better computational time.

## 5.6.  Conclusion

Computational aspects including memory issues and execution time are important in developing more efficient 3D EIT systems. A reconstruction method for large scale 3D EIT has been proposed. This method is a combination of sparse matrix method and a block-wise CGLS algorithm. This is especially suitable for large scale EIT problems that cannot be solved by traditional methods such as the standard Tikhonov regularisation method. The level of thresholding is investigated as a tool for the sparse Jacobian method. It has been found that the optimum threshold is different when dealing with varying locations of the inclusion(s). However, 32 channel system simulations show that when applying the critical case, which is by placing an object in the centre, a suitable threshold value of 1% is achieved before the image quality starts to degrade. In this worst case scenario (of an object in the centre of 3D phantom), increasing the sparsity of the Jacobian matrix by more than 50% will dramatically affect the imaging results. In practical settings a calibration of thresholding can be done by testing the image quality for the smallest object to be detected in the least sensitive area. Adjacent pattern was used in this study, and this thresholding value may vary for a different excitation/measurement pattern. By making good use of the sparse Jacobian technique and combining the method of partitioning the Jacobian into the blocks, the inverse problem in large scale 3D EIT problems can be solved effectively. Further improvement has been achieved by parallel implementation of the block-wise CGLS in multicore systems. This could be a suitable alternative for the large scale EIT inverse problem.

# Chapter.6 Subsurface EIT

A different EIT geometry for detecting the conductivity distribution beneath the surface of a medium is proposed in this chapter. Mueller [113] has presented a simple implementation of a 3D reconstruction algorithm on a four by four electrode array and the reconstructions obtained from numerical and experimental tank data. Such an electrical configuration may be desirable for using EIT to detect tumours in the human breast [114].

## 6.1. Background

A planar array system is treated as an emerging measuring platform which has multiple uses in medical and clinical areas [115]. Unlike the EIT system with annulus electrodes, the planar EIT can provide more flexibility of the electrode structure, add convenience in operation [116] and be applied into some difficult measuring situations. For example, the size of the breast, head and skin is much smaller than the chest and abdomen for which the EIT technique has achieved huge success [117]. The previous annular electrode system is no longer appropriate for small-volume objects [114], so in order to overcome the barrier, the planar array EIT is put forward.

Though the 3D planar array EIT can be applied to small area detection and obtain multi-layer reconstructed images [118-120], there are still technical challenges making it hard to employ. Firstly, adding more electrodes to improve the distinguishability of the reconstructed images is not possible for the small-volume objects. Secondly, the planar array EIT system cannot obtain the deeper image of the object because of the limitation of the sensitivity of the electrodes. Finally, the finite element model and the algorithms involved are different from the previous system and this restricts the development of the planar array EIT.

However, the 3D planar array EIT still has a broad prospect in clinical application. In the near future, this technique will make great contributions to long-term disease observation and cancer detection like the bladder filling examination [121], breast tumour screening and skin cancer detection.

The main study of subsurface EIT requires knowledge of hardware design, planar array EIT software development and detailed design of experiments carried out. In this chapter a planar array of 4 x 4 electrodes attached on the surface of a phantom side is constructed to detect the conductivity distribution inside a cuboid-shaped phantom and obtain the reconstructed images using MATLAB. The data processing is completed by using the EIDORS tool kit to solve the forward problems by FEM and iterative regularized inverse solvers. The challenging part is to distinguish and locate the inserted objects precisely and present the size and shape of the objects in the reconstructed images, which means that a more stable and accurate hardware system is needed. Methods used to surmount the barriers are utilizing the new algorithm and designing an advanced mesh model for image reconstruction. In this section, several experiments are conducted and the corresponding reconstructed images produced by MATLAB are well presented to demonstrate the whole process.

## 6.2. System and phantom design

We implemented a hardware model for a plane array EIT. The phantom is a cuboid container which is also made of plexiglass (Figure 34). It has a square shape 3D phantom with width 14cm and height 25cm. Circular shape electrodes (radius = 5cm) are attached to two sides of the phantom, each side consisting of 16 electrodes. As in the proposed simulation model, only one side of the experimental phantom is required, which has 4x4 numbers of electrodes. By connecting one side of the phantom to the acquisition system, data from the 16 electrode plane array EIT can be acquired (Figure 35).
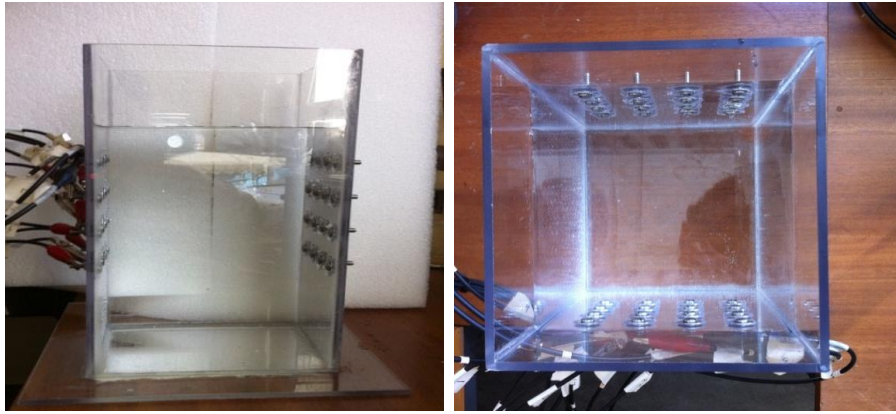
*Figure 34: Top view and lateral view of the planar array EIT phantom*
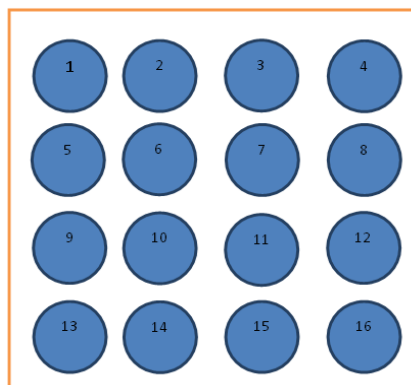


*Figure 35: The distributions and numbers of the electrodes*

The 16 circular electrodes are fixed in a 4x4 square shape and the gap between each electrode is 1cm. All the electrodes are marked from 1 to 16 in order not to get confused when connecting to the equipment. The schematic diagram of the positions and numbers of the 16 electrodes is shown in Figure 35.

The system used in the laboratory is the KHU Mark2.5. In the process of data acquisition, the measured voltage potentials are collected at all of the electrodes and then processed by the computer with high running speed and sufficient capacity. The whole procedure needs a constant current source to provide the injection current and a multiplexer to deal with the switching modes of the applied current and measured voltages. In my project the adjacent switching pattern is also suitable for the voltage measurement. The safe current is injected into two adjacent electrodes and the voltages between any other two electrodes are measured each time. Then the current will be injected into next pair of electrodes and the process will continue until all the electrodes are used.

16 electrodes are employed in the experiment, which means that 16x13=208 measurements are obtained in total.
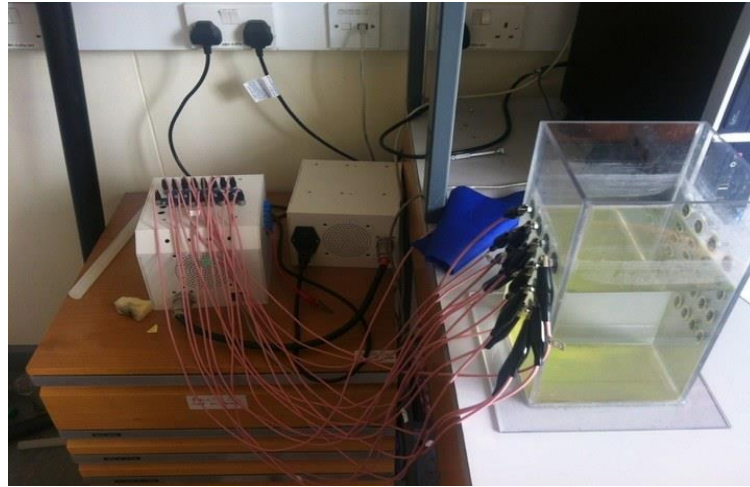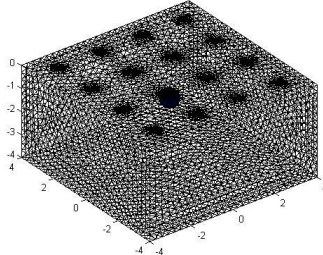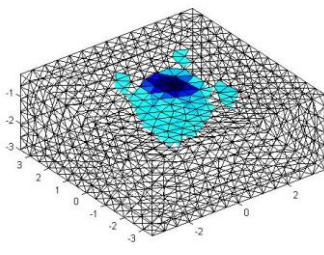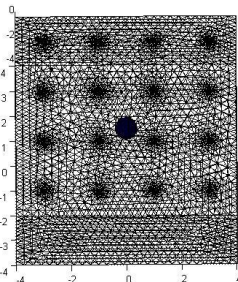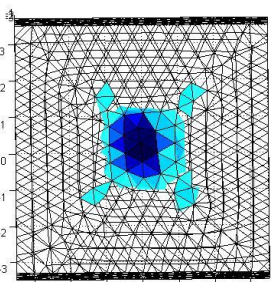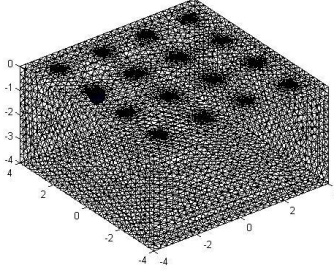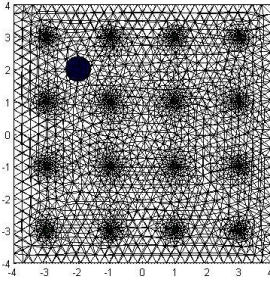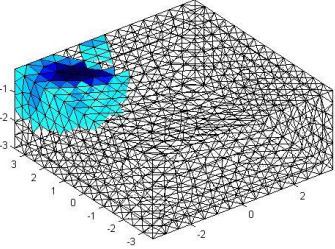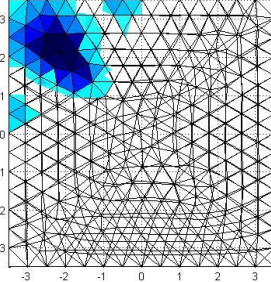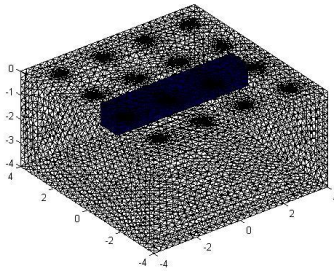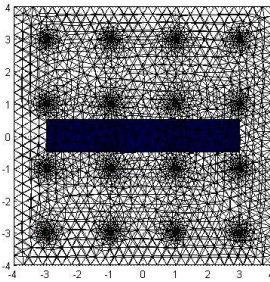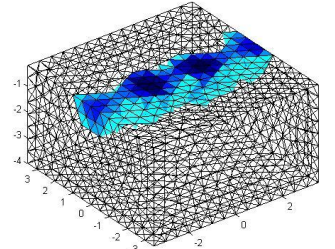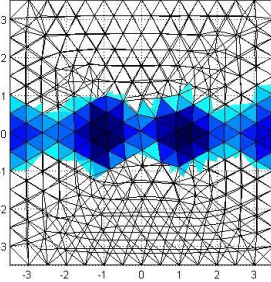


*Figure 36: Planar array EIT phantom*

## 6.3. Simulation study

Before the phantom test a series of simulations were done to test the feasibility of the subsurface electrode model and examine the performance of the programme. The image reconstruction method using in this study is based on the 3D surface electrode reconstruction algorithm implemented in EIDORS. Different types of inclusions are introduced and also multiple object reconstructions are carried out. Furthermore, objects in different locations of the surface are imaged to test the coverage of the 3D electrode surface. Another important aspect in 3D surface electrode EIT is to find out how far away from the electrode plane can the object still be detected. A set of simulations are done for this purpose.

| Objects and location | True image of object | Reconstructed image |
|---|---|---|
| A sphere with 0.4cm radius at the centre |  |  |

| | | |
|---|---|---|
| |  |  |
| A sphere with 0.4cm radius at the top left side |  |  |
| A rectangular object located in the centre |  |  |
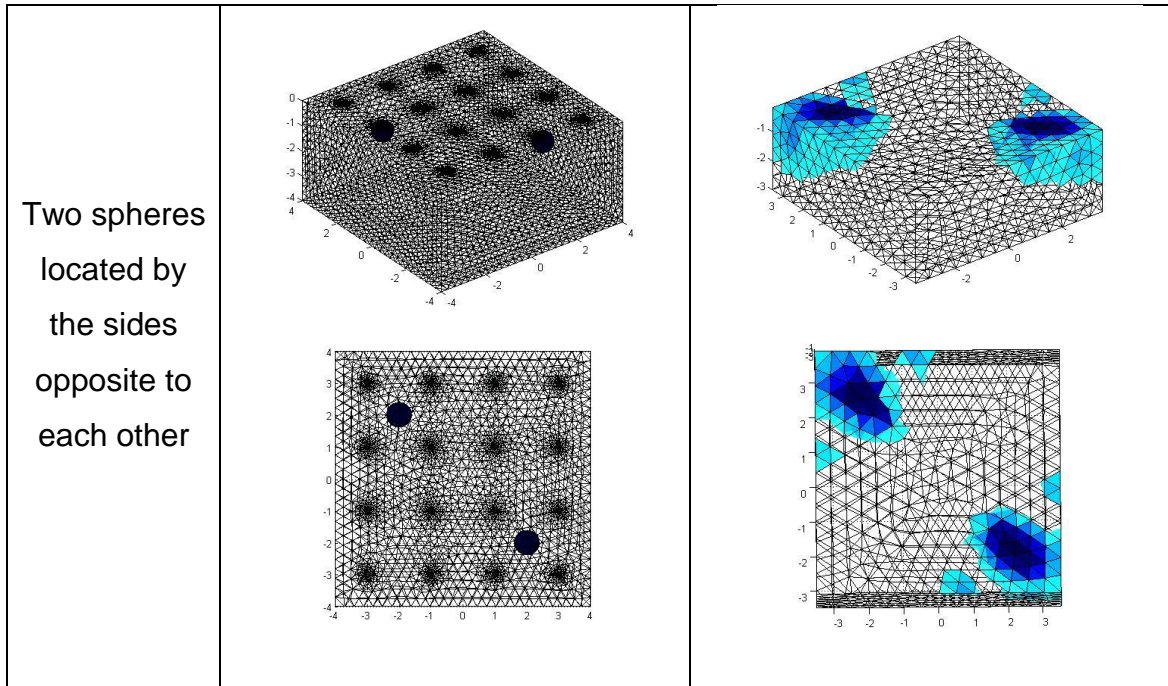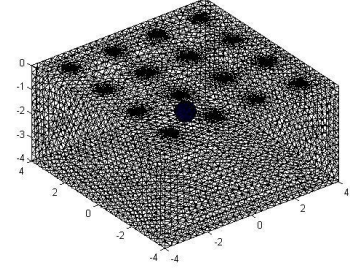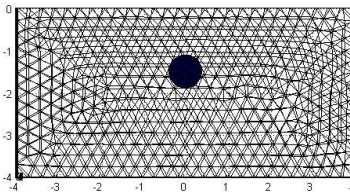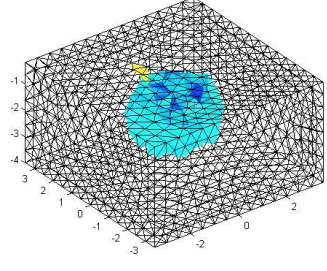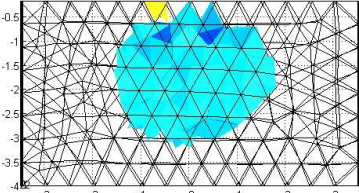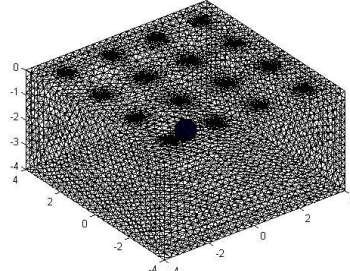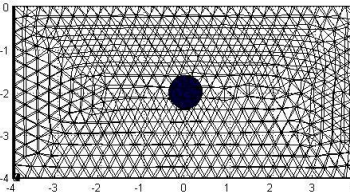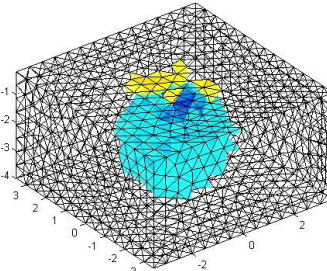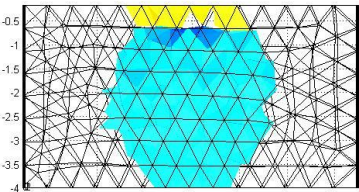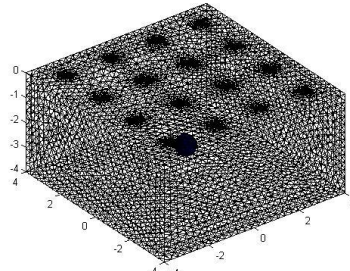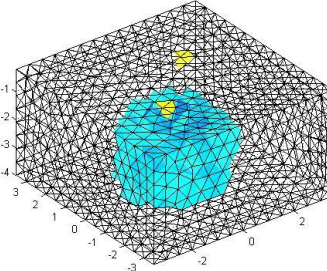
*Figure 37: Computer simulation results of a 4x4 subsurface electrode EIT system*

Some applications, such as skin cancer detection, using the planar array EIT system only require the system to detect anomalies near the surface electrode plane. The simulation studies shown in Figure 37 show promising results when an object is located near the electrode plane for both small sphere and larger cuboid shape objects. However, it is supposed that image reconstruction would become more difficult when the true object is located further away from the electrode plane. For applications such as crack detection, when the anomaly is located further away from the electrode array, it is essential to have an EIT system developed which has the ability to image objects when the distance between the object and the electrode array is increasing. A series of simulation works have been done to test the reconstruction performance.

| Objects and location | True image of object | Reconstructed image |
|---|---|---|
| | | |

| | | |
|---|---|---|
| A 0.4cm radius sphere at 1.5cm under the electrode plane |  |  |
| A 0.4cm radius sphere at 2cm under the electrode plane |  |  |
| A 0.4cm radius sphere at 2.5cm under the electrode plane |  |  |

| | | |
|---|---|---|
| |  |  |
| A 0.4cm radius sphere at 3cm under the electrode plane |  |  |
| A 0.4cm radius sphere at 3.5cm under the electrode plane |  |  |
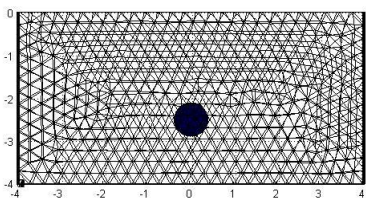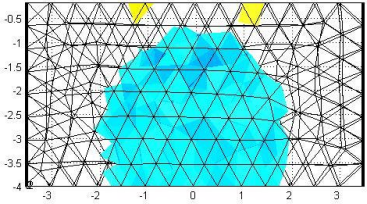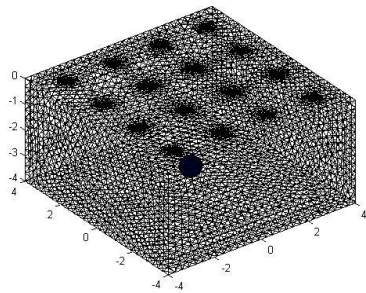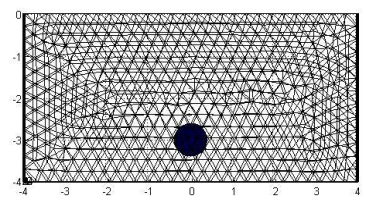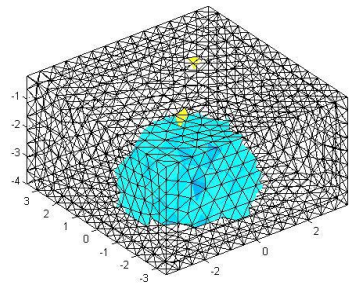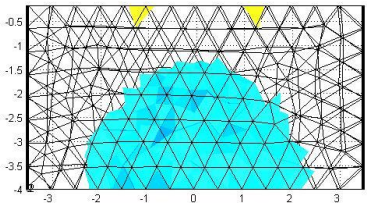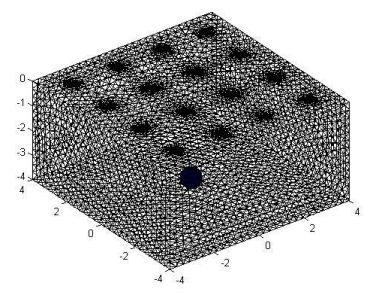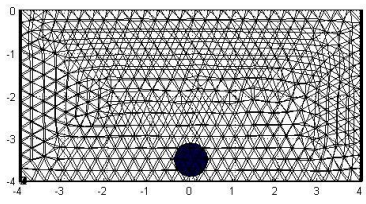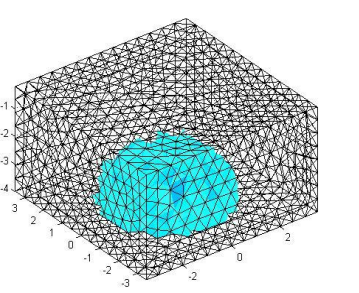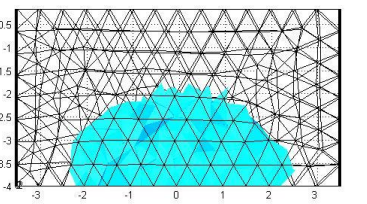
*Figure 38: Simulation study of 3D subsurface EIT system when the object is getting further away from the electrode array*

## 6.4. Experimental validation

The reconstruction image is the most intuitive and efficient way to assess the performance of the EIT system. Here several types of experiments are designed to test the performance of this EIT system in all domains.

To ensure the accuracy of the result, some tips have to be followed during the experiment:

1. Use the same distilled water throughout the experiment to make sure the background data is the same;

2. Do not move the inserted objects when gathering data;

3. Record the exact place of the object every time and it will be easier to compare and at the same time the accuracy of the result is guaranteed.

### 6.4.1. Plastic stick in different locations

The experiments on a single plastic stick with different locations and two plastic sticks near the electrodes are designed to test the performance of the reconstruction image near the subsurface and the ability to distinguish the two objects.

| Object location | Reconstruted image |
|---|---|
|  |  |
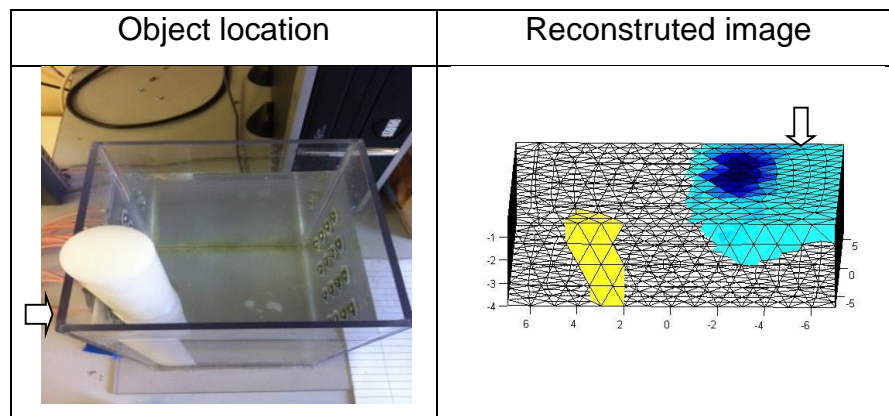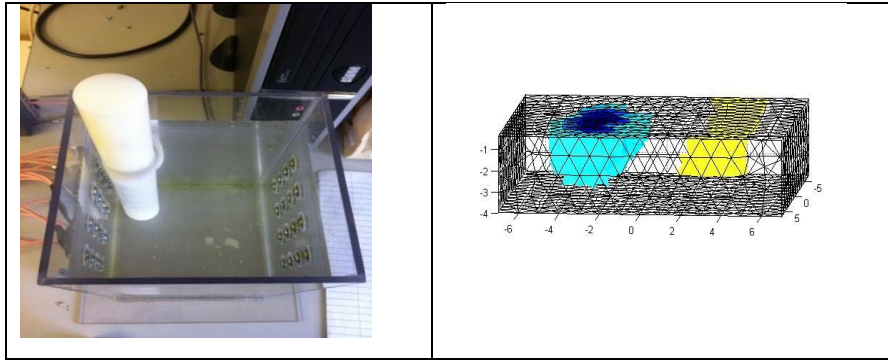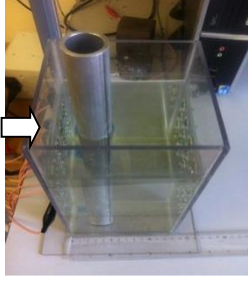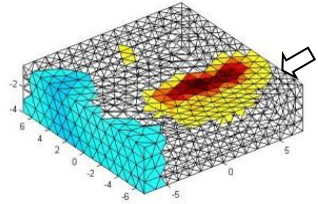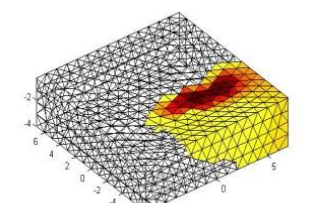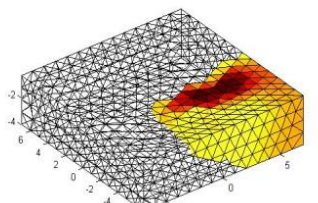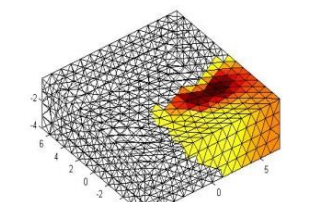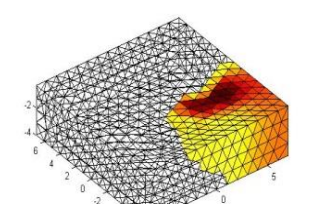
*Figure 39: Experiments with plastic sticks in different locations*

The result reveals that the performance of the system with one single object is good and the location, shape and size of the object can be observed.

### 6.4.2. An iron stick with different distances to the electrode plane

This series of experiments shows the effect on the reconstruction images with different distances. We chose the iron stick as the experimental object because the conductivity of iron (around 80W/mK) is much higher than plastic (around 0.03W/mK) and it makes the iron more detectable.

| Distance to electrode surface (cm) | Object location | Reconstructed image |
|:---:|:---:|:---:|
| 2 |  |  |
| 3 |  |  |
| 4 |  |  |
| 5 |  |  |
| 6 |  |  |

| | | |
|---|---|---|
| 7 |  |  |
| 8 |  |  |
| 9 |  |  |
| 10 |  |  |
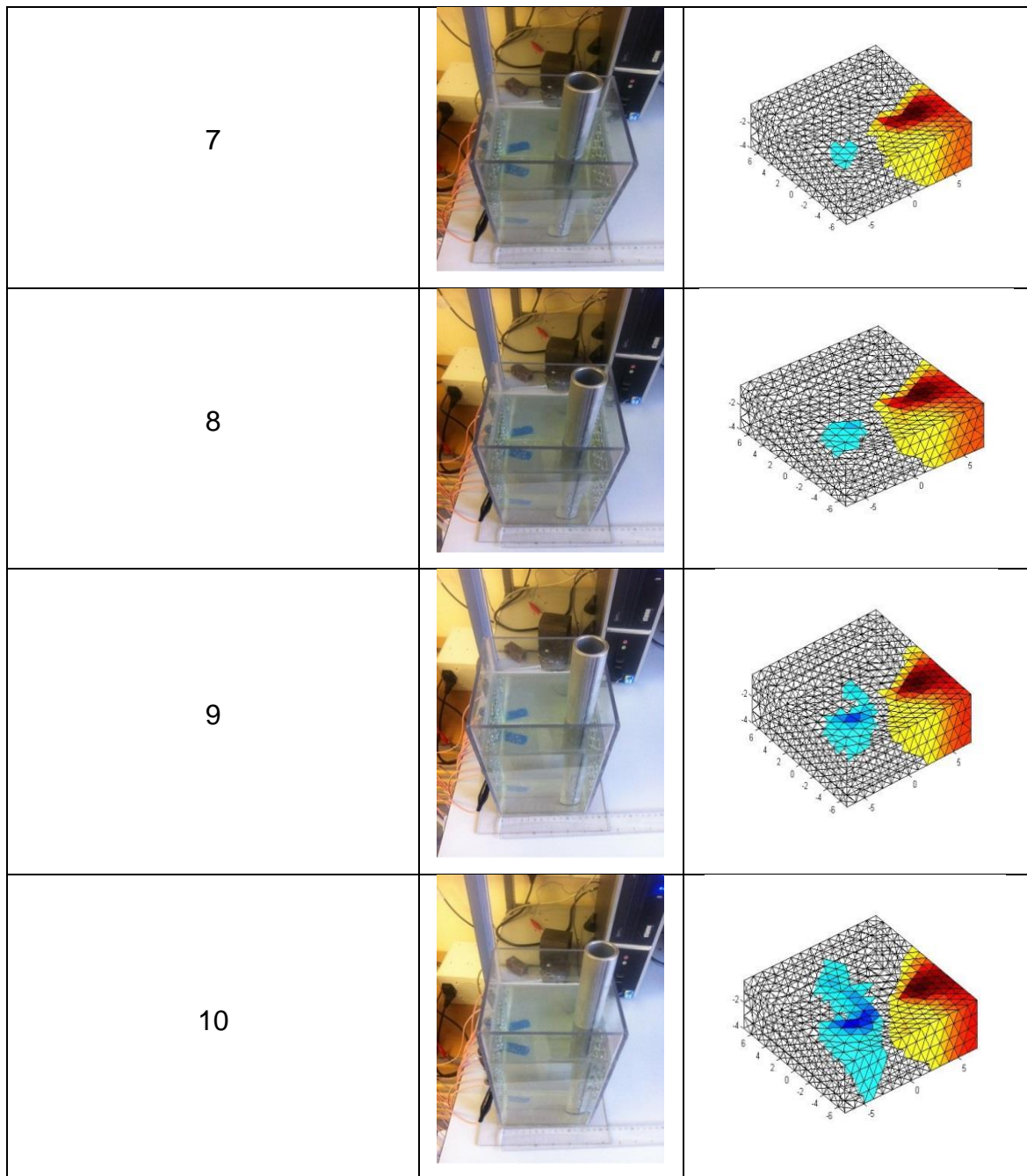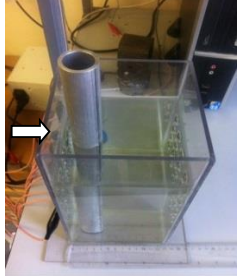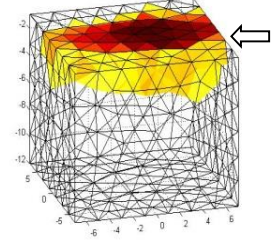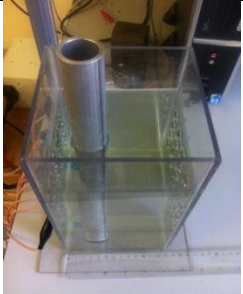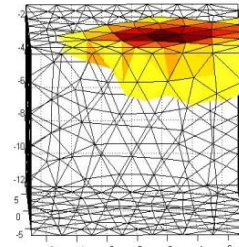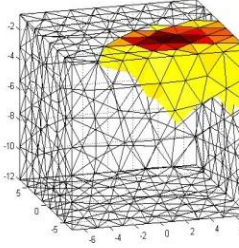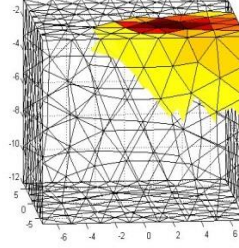
*Figure 40: Experiments with the iron stick with different distances*
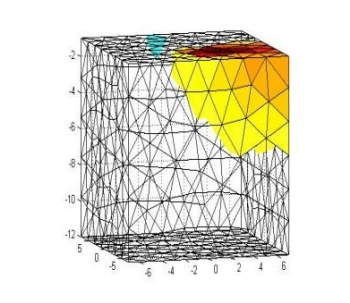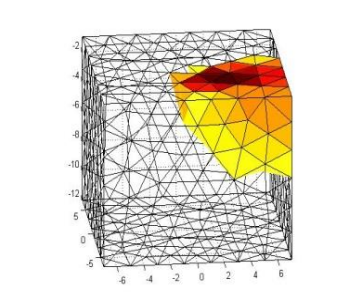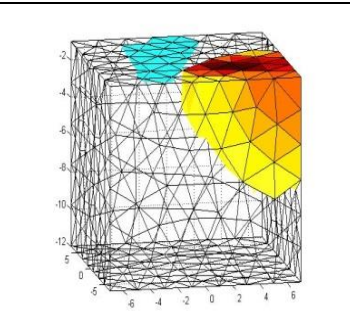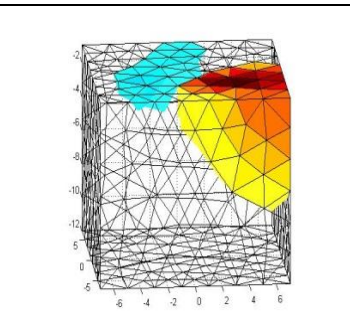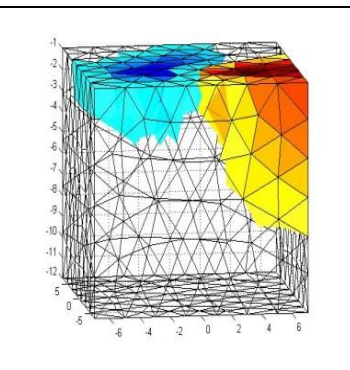
From the reconstruction images, the yellow area grows thicker as the stick moves far away from the electrodes and it means that position of the stick moves away from the electrodes. And also the shade of colour changes over the distance.

But due to the limitation of the mesh model it is hard to see any obvious difference after 7cm. The possible reason is that the depth of the model is not

enough to contain all the information and the reconstructed images are compressed into a limited space. So in order to solve the problem, a larger size mesh model will be constructed. In the meantime, some unknown noises occur in the area far from the electrodes, which implies that the system is not suitable for detection in deeper areas.

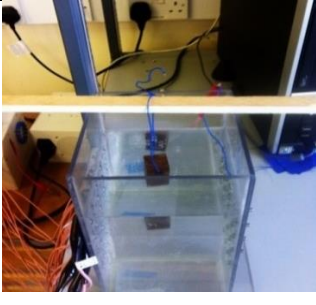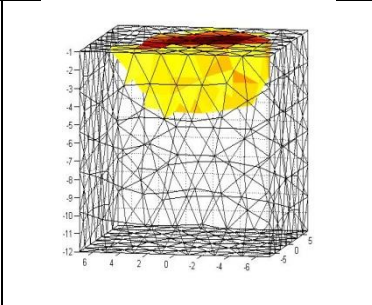### 6.4.3. An iron stick with different distances to the electrode plane (larger mesh size)

| Distance to electrode surface (cm) | Object location | Reconstructed image |
|---|---|---|
| 1 |  |  |
| 2 |  |  |
| 3 |  |  |
| 4 |  |  |

| | | |
|---|---|---|
| 5 |  |  |
| 6 |  |  |
| 7 |  |  |
| 8 |  |  |
| 9 |  |  |

*Figure 41: Repeated experiment in 6.4.2 with a larger-size mesh model*

With a larger-size mesh model, the compressed part is extended and it reflects on the colourful area. As shown above, the thickness of the yellow area is increasing as the distance increases and it clearly suggests the movement of the object. Compared with the previous test, the result of the experiment with the larger-size model is much better. From the calibratrion on the x,y and z axes, the rough position of the object can be obtained.

In the first image, the shape of the object is clear and close to the real schematic, and as the object moves far away the red area reduces gradually because the ability to detect a signal decreases and it presents like an inverted cone. But it is not ideal as a simulated image in which the area between the object and electrodes can be clearly distinguished. A possible reason is that the current field of the circular electrode is not uniform and the density of the current field is low away from the electrodes. Also some noise and interfence is shown in the reconstruction images.

## 6.4.4. An iron cube with difference distance to the electrode plane
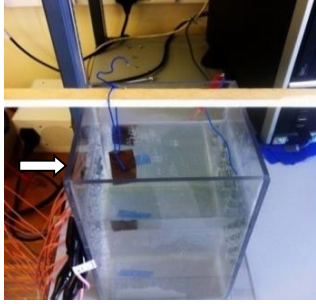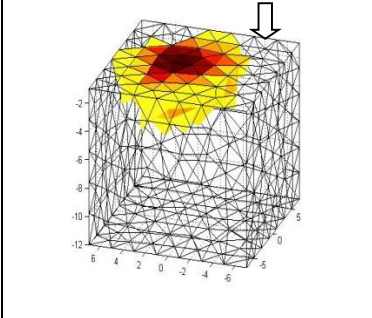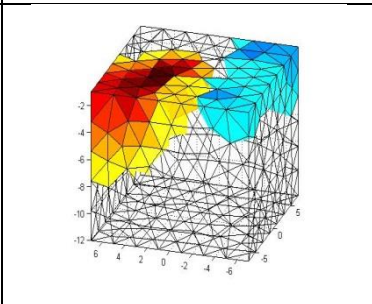
| Distance to the electrode plane (cm) | Object location | Reconstructed image |
|:---:|:---:|:---:|
| 1 |  |  |
| 4 |  |  |
| 8 |  |  |

*Figure 42: The real schematics of the experiments and corresponding reconstruction images*

The size of the iron cube (conductivity around 80W/mK) is about 1.5x1.5x2.5cm. Only three sets of results are displayed above because the size of the cube is comparatively small which makes it more difficult to detect and determine the shape and position of the cube. Therefore three typical sets are chosen to demonstrate the result of the experiment. The distance to the electrodes is 1cm, 4cm and 8cm. As seen in the pictures, the result of the

experiment is not satisfying and it implies that the 16 circular-electrode planar array EIT system is not very feasible for small objects.

### 6.4.5. Two different objects in the phantom

In this experiment, several different objects are used to test the performance of the reconstruction algorithm.

| Object location | Reconstructed image |
|---|---|
|  |  |
|  |  |
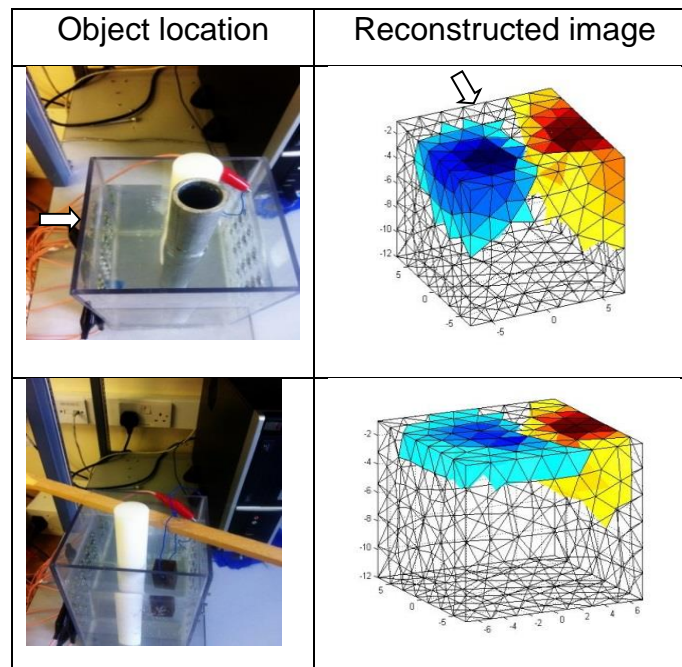
*Figure 43: Different objects in the phantom and reconstruction images*

In the first picture, two long sticks made of different materials, one is plastic and the other is iron, are used. The result reveals that the reconstruction images well determine the shape and location of the objects.

In the second picture, an iron cube and a plastic stick are chosen as the experimental objects. Similarly, the objects are put in different locations. The reconstruction shows a similar pattern to the stick experiment and it is possible to tell the location of the objects from the colour difference and thickness of the colourful area. However, it is difficult to determine the size of the objects by direct observation from the reconstruction image.

## 6.5 Data analysis and reliability assessment

Simulation shows promising result in all cases including test of object in different distances to the electrode plane. Figure 44 shows the background reading taken by simulation and phantom experiment. Both measurements have identical pattern and real data has stronger signal. This indicates that measurements taken from the sensor is in good quality. However, experimental result comes out not being as good as expected from the simulations. This may be cause by experimental phantom design could not be perfectly fit the original generated mesh. A reliability assessment table (table 8) is generated to evaluate the effects and limits of the current designed planar array sensor.
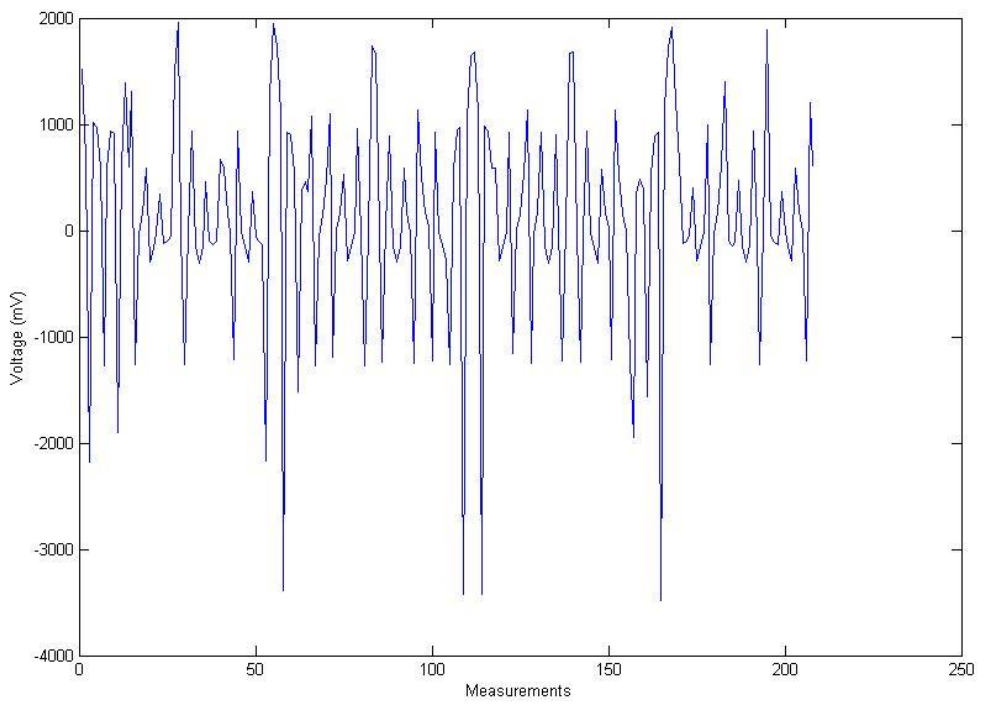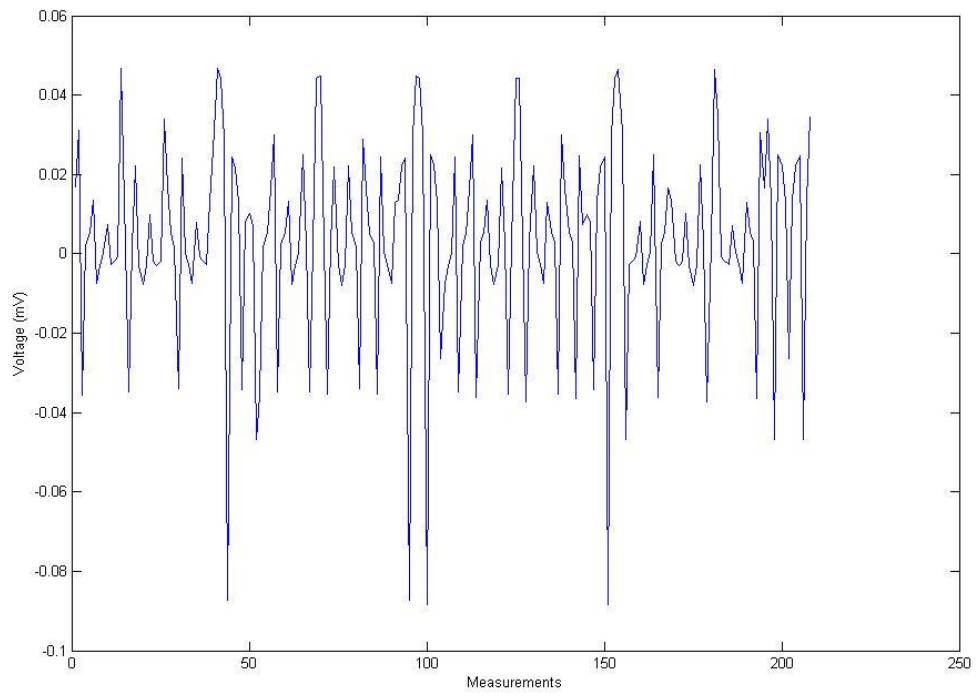
*Figure 44: Background data of planar array EIT sensor (Simulation and real data)*

Table 8: Reliability assessment of planar array EIT sensor

|  | Simulation results | Experimental results |
|---|---|---|
| Signal detection | Strong | Strong |
| Object detection | Yes | Yes |
| Multiple objects detection | Yes | Yes |
| Object location | Precisely correct | Quite accurate |
| Size and shape reconstruction | Quite reliable | Unreliable |
| Reconstruction in depth | Very accurate | Shows pattern of object moving away but inaccurate |

## 6.6. Conclusion

All the procedures and details of experiments are presented in the chapter. With simulation images and the real schematics it is clear to see the performance of the planar array EIT imaging reconstruction method. Simulation study provides a promising result. However, experimental validation using a real phantom did not work well in all cases, maybe due to some experimental errors. This study is proposed to be useful for people working on a subsurface EIT imaging area as this is an early study that combines good simulation results and a large number of real phantom experiments in many cases.

# Chapter.7 Multi-frequency EIT for fabric pressure mapping sensor

The EIT-based fabric pressure mapping sensor aims to provide a pressure mapping image using current carrying and voltage sensing electrodes attached on the boundary of the fabric patch. This is potentially a very cost effective pressure mapping imaging solution, in particular for imaging large areas. Recently, promising results are being achieved in resistivity imaging for these sensors. However, the fabric structure presents capacitive behaviour that could also be exploited for pressure mapping imaging.

In this chapter, an EIT-based fabric pressure mapping sensor is presented and tested. In the proposed model a pressure sensitive fabric patch is stretched over a deformable support along which electrodes are attached. In order to measure the pressure-induced shape change over the fabric patch a predetermined sequence of currents is injected and the corresponding voltages through electrodes are measured. Reconstructions are done by using complex impedance data. To identify how the imaginary part data changes with respect to frequency can be a benefit for the image reconstruction, and a series of multiple frequency tests are employed. GREIT parameters are calculated to measure the image performance.

## 7.1. Background

Complex conductivity reconstructions with multiple frequencies [122, 123] are being studied in this chapter to observe both conductivity and permittivity changes due to the pressure applied on the fabric. The related mathematical framework of complex conductivity reconstruction is presented. Experimental studies on detecting the change of complex conductivity using both an EIT tank phantom and a fabric pressure mapping sensor are performed allowing a comparative evaluation. First, electrical impedance spectroscopy on a fabric pressure mapping sensor is performed. Secondly, complex impedance tomography is carried out on a fabric and on a traditional EIT tank phantom. Quantitative image quality measures are used to evaluate the performance of a

fabric pressure mapping sensor at various frequencies and are compared with the better understood tank phantom. This chapter of the thesis demonstrates for the first time the useful information available on pressure mapping from the imaginary component of conductivity imaging.

The EIT-based fabric pressure mapping technique has become a popular area of EIT study in recent years with various potential applications in mind. It can provide major improvements in the cost and operation complexity for clinical facilities, as the technology is very cheap and simple. It can be applied to dynamic pressure seating systems and mattresses for patients' ulcer prevention [124, 125]. Additionally, potential touch sensitive applications such as robotic skin are applicable and are being developed [4, 126-128]. Also different kinds of sensor structure have been introduced and tested, such as a rectangular fabric pressure mapping sensor. Previous research has shown promising results on pressure detection [129, 130]. The characteristic of conductive polymer for an EIT-based sensor is evaluated in [131] for analysing the non-linearity and hysteresis behaviour of the sensor. These sensors could limit the application of pressure mapping imaging, in particular in dynamic situations with rapid changes of applied pressure. Further information through multiple frequency reconstruction and complex impedance imaging could potentially help to overcome these problems.

Most EIT experiments measure the resistivity information of the object, as the capacitive component is used in fewer applications. The resistive component can only provide information of the behaviour of the yarn. When the fabric patch has been stretched, the air gaps between yarns will change shape and this will be the capacitive information. If both resistance and capacitance are obtained, the reconstruction image of the fabric might become more accurate and reliable. By making a complex conductivity reconstruction one can obtain real and imaginary data for conductivity, where the permittivity change is mainly indicated by the imaginary part of the voltage measurement and is highly related to the capacitive changes in the material. In order to validate this approach, various experiments of complex conductivity reconstruction on both saline phantom and fabric pressure mapping sensors are performed, which provides a comparative study.

## 7.2. Complex impedance measurements on fabric

In order to analyse the impedance spectrum change of a piece of conductive fabric, a device was used to measure the complex impedance. The tetra-polar (separate current and voltage electrodes) measurement method was used for characterisation of tested fabric material. Each electrode was made up of a pair of stainless steel bars. They immobilized the piece of tested fabric with a sandwich structure and plastic nuts and bolts. The large surface area and high conductive electrodes may minimize the effect of electrode contact impedance. Also, this is to ensure that injected current will flow uniformly across the fabric material to cancel out the geometric effect. Figure 45 shows the picture of measuring the impedance spectrum of a piece of fabric.
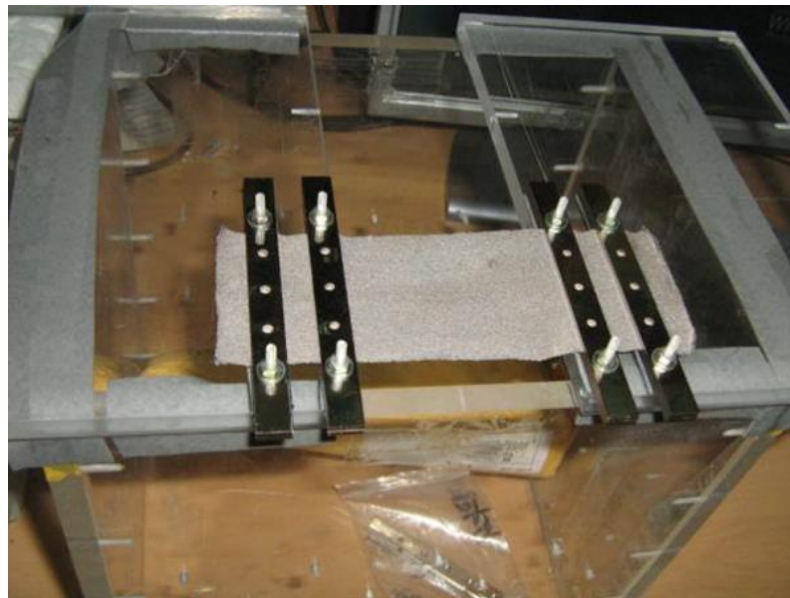


*Figure 45: Picture of measuring impedance spectrum of a piece of fabric*

Complex impedance values were measured with increasing pressure applied in various frequency ranges. Figure 46 is generated by plotting the impedance values against different weight data. It can be observed that both real and imaginary parts of the impedance measurement vary with frequency. The impedance value increases as frequency increases.
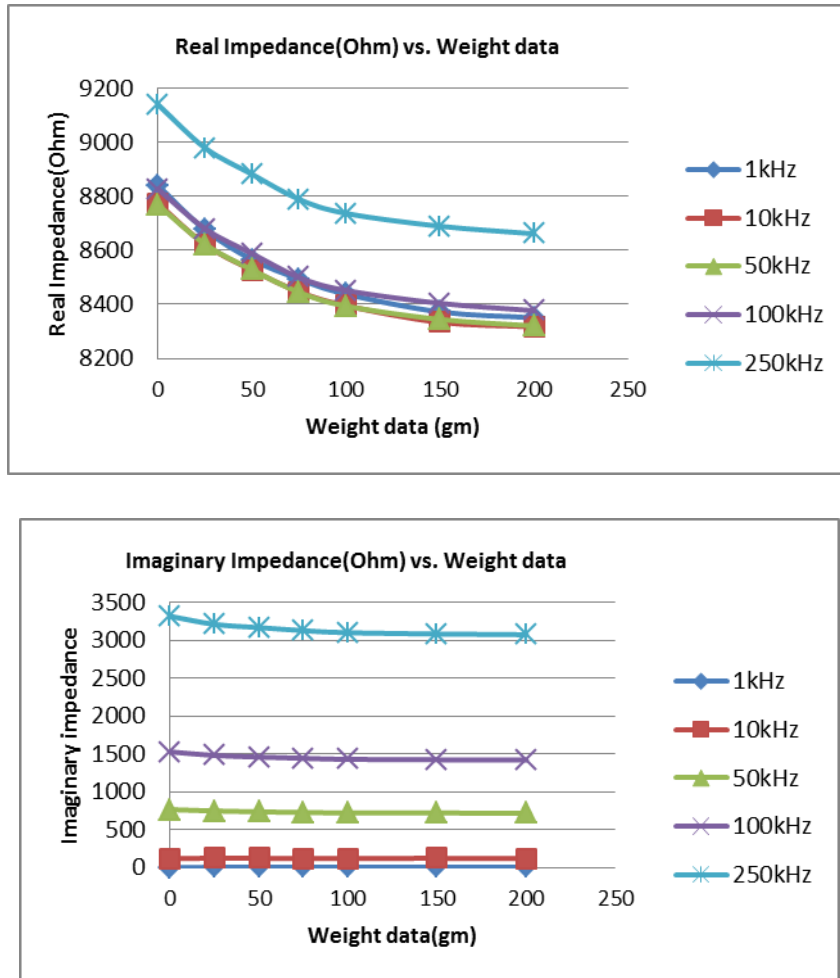
*Figure 46: Plots of complex impedance value against weight data*

There are measurable variations in real and imaginary parts of impedance of the fabric structure. This motivates complex impedance tomography for pressure sensing fabric.

## 7.3. EIT hardware

To measure the small changes of complex impedance due to the pressure requires a high accuracy EIT measurement system with uniform performance within the operating frequency range.

Experiments were carried out using the KHU Mark2 EIT system developed by the research group in Kyung Hee University, Korea [82, 132].

By acquiring two different sets of voltage measurement data, the computer software is used to do a time difference image reconstruction. A 16 electrode
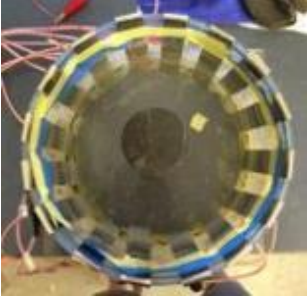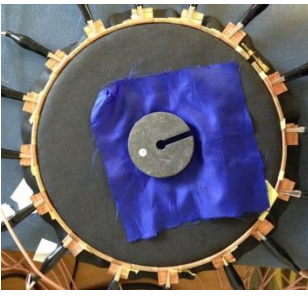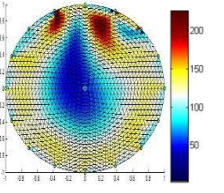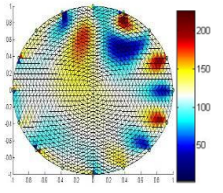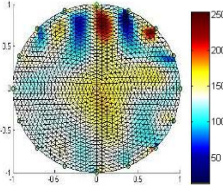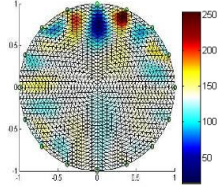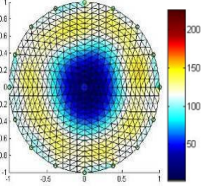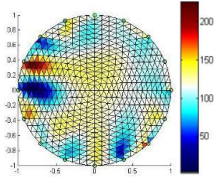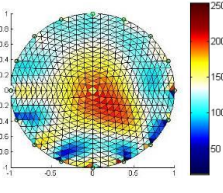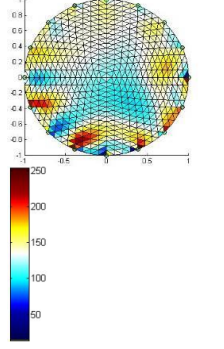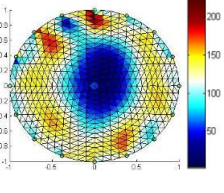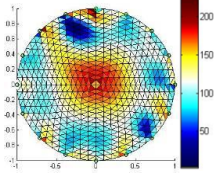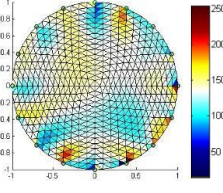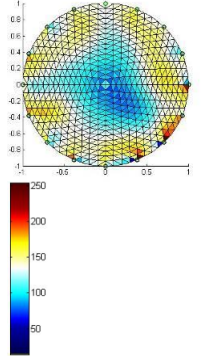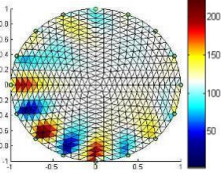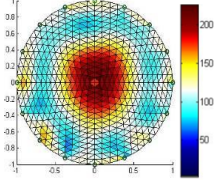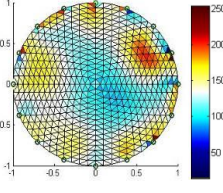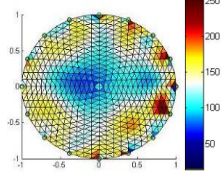
EIT with adjacent current pattern was used for multiple frequency EIT imaging at 1kHz, 10kHz, 50kHz, 100kHz, and 250kHz excitation frequencies.

## 7.4. Experimental validations

To evaluate the behaviour of complex conductivity changes due to the change of frequency, two types of sensor have been built: one is a typical 16 electrode tank phantom and the other is the 16 channel EIT-based fabric pressure mapping sensor. This sensor consists of a conductive fabric patch and a circular wooden frame with a sponge pad at the bottom. 16 narrow copper plates are used as boundary electrodes placed equidistant between the circular frame and the fabric. The conductive fabric used here is EeonTex™ NW170-SL-PA-1500, developed by Eeonyx Corporation, with a surface resistivity of 1500 ohm/sq. +/- 15%. It is a nonwoven microfibre coated with a conductive formulation, generally used for dynamic pressure sensors [133].

Conductivity distribution varies with the deformation of the fabric in respect to the pressure sensitive characteristic. Since the modal structure of the fabric-based sensor is not pure resistance, measurement of the imaginary part of conductivity distribution can be useful, particularly for the capacitive effect in the contact nodes, and the change due to the deformation of the structure can provide valuable information. All experiments include reconstruction images of both the real and imaginary parts of conductivity changes.

Two sets of experiments were carried out. Each of the tests included a tank phantom test and a fabric pressure mapping sensor test. For adjacent current pattern EIT measurement, the centre position was considered to be the most difficult imaging position. Therefore, the first test was to perform image reconstruction in the centre position for both sensors. The results are shown in Figure 47. It is important to note that both real and imaginary parts of the Jacobian matrix are functions of the real and imaginary parts of the impedance, as is reflected in Equation 8 in Chapter 3.

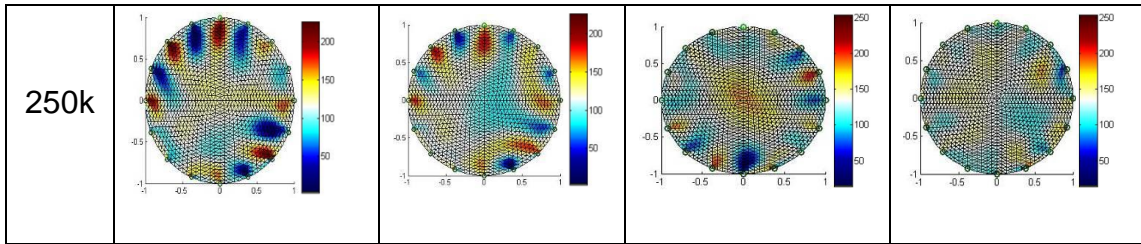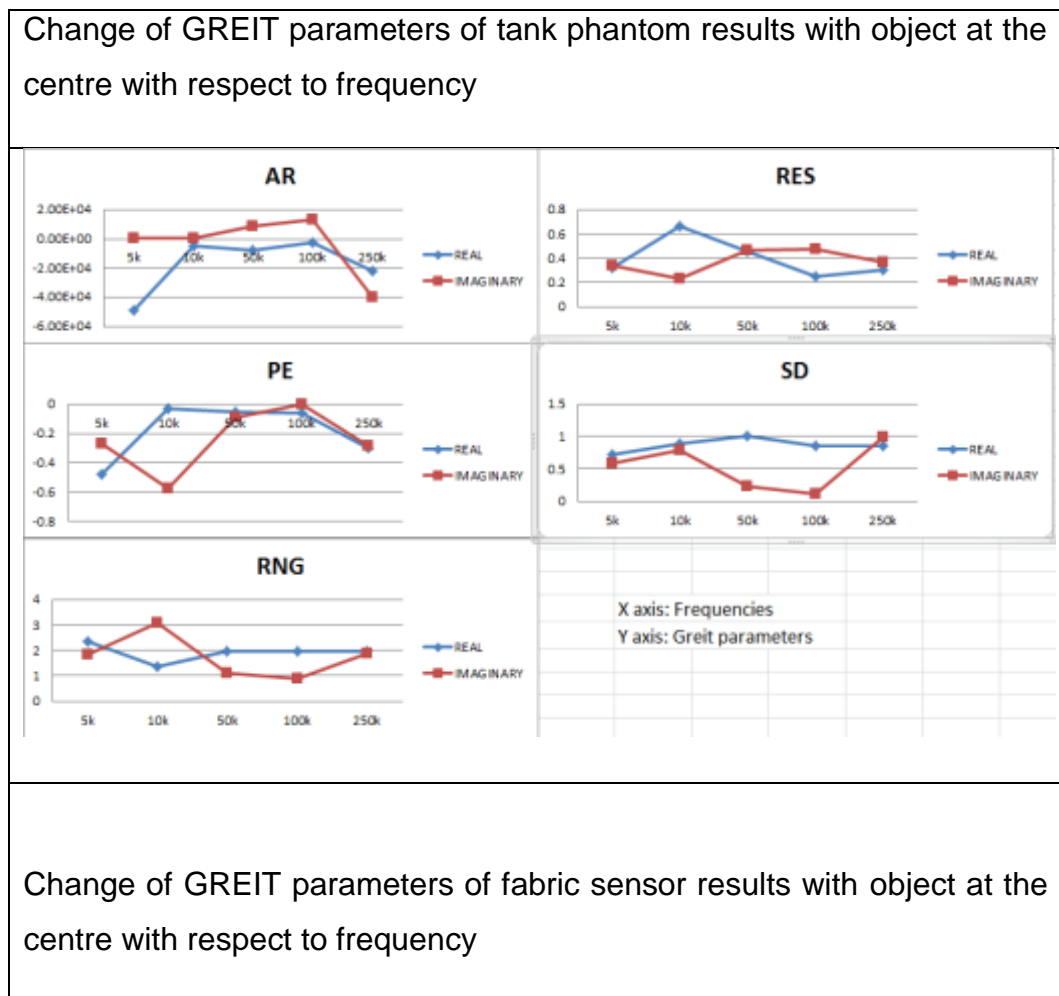| Freq. (Hz) | Tank phantom (Real) | Tank phantom (Imaginary) | Fabric sensor (Real) | Fabric sensor (Imaginary) |
|---|---|---|---|---|
| |  | |  | |
| 5k |  |  |  |  |
| 10k |  |  |  |  |
| 50k |  |  |  |  |
| 100k |  |  |  |  |

| 250k |  |  |  |  |

*Figure 47: Complex conductivity reconstructions at a multiple frequency range with centre pressure point (Test 1)*

Most typical EIT experiments only acquire real conductivity information that provides good image results like those in Test 1 at a frequency of 10kHz. As the frequency increases, it can be observed that image qualities of the real conductivity start to degrade, while the imaginary part shows the opposite behaviour.

Change of GREIT parameters of tank phantom results with object at the centre with respect to frequency



Change of GREIT parameters of fabric sensor results with object at the centre with respect to frequency
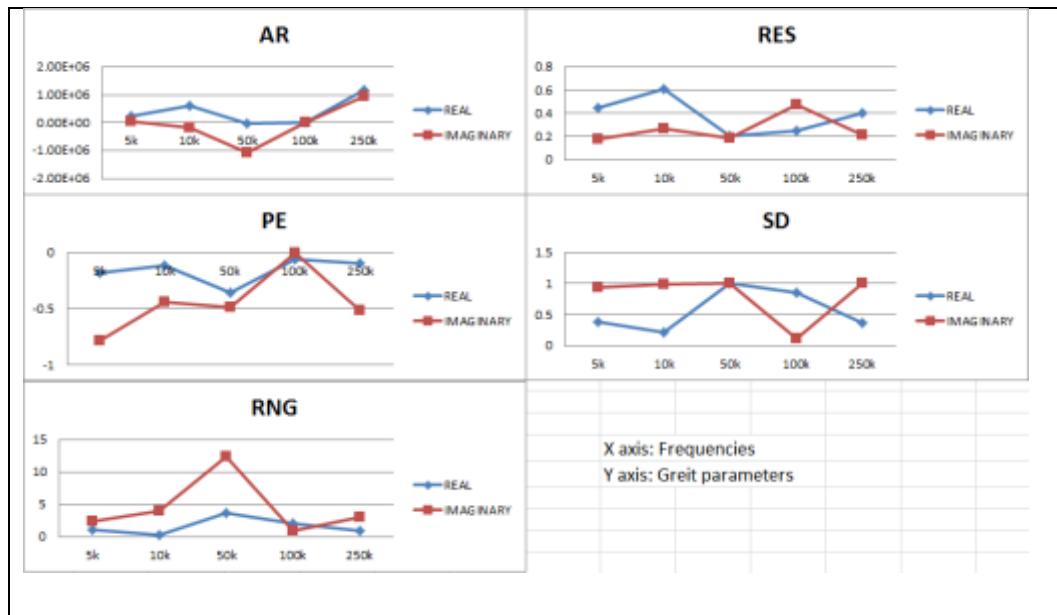
*Figure 48: Evaluation of GREIT parameters AR, RES, PE, SD, and RNG as a function of point radial position (Test 1)*

From Figure 48 it can be observed that some important parameters, such as RES and SD, change relative to the quality of the reconstruction images. Focusing on the real part, it indicates that RES drops with increasing SD for real conductivity reconstruction while frequency increases. Imaginary part data behaves in the opposite manner. It means that the image from real part data is losing resolution and starting to shape change when the frequency increases. However, the imaginary part image remains in shape and has better resolution. PE behaves a bit randomly and shows small changes as the positions do not vary much from the centre. This shows that information from the imaginary part could be of benefit for reconstruction when the system is operated at high frequencies, such as 100kHz. Performance of imaginary images have bigger changes through the operating frequencies, because the same amount of capacitance variation can produce a different amount of change in the result at different operating frequencies.

The second test was to perform image reconstruction with the target position at one side for both sensors. Results are shown in Figure 49.
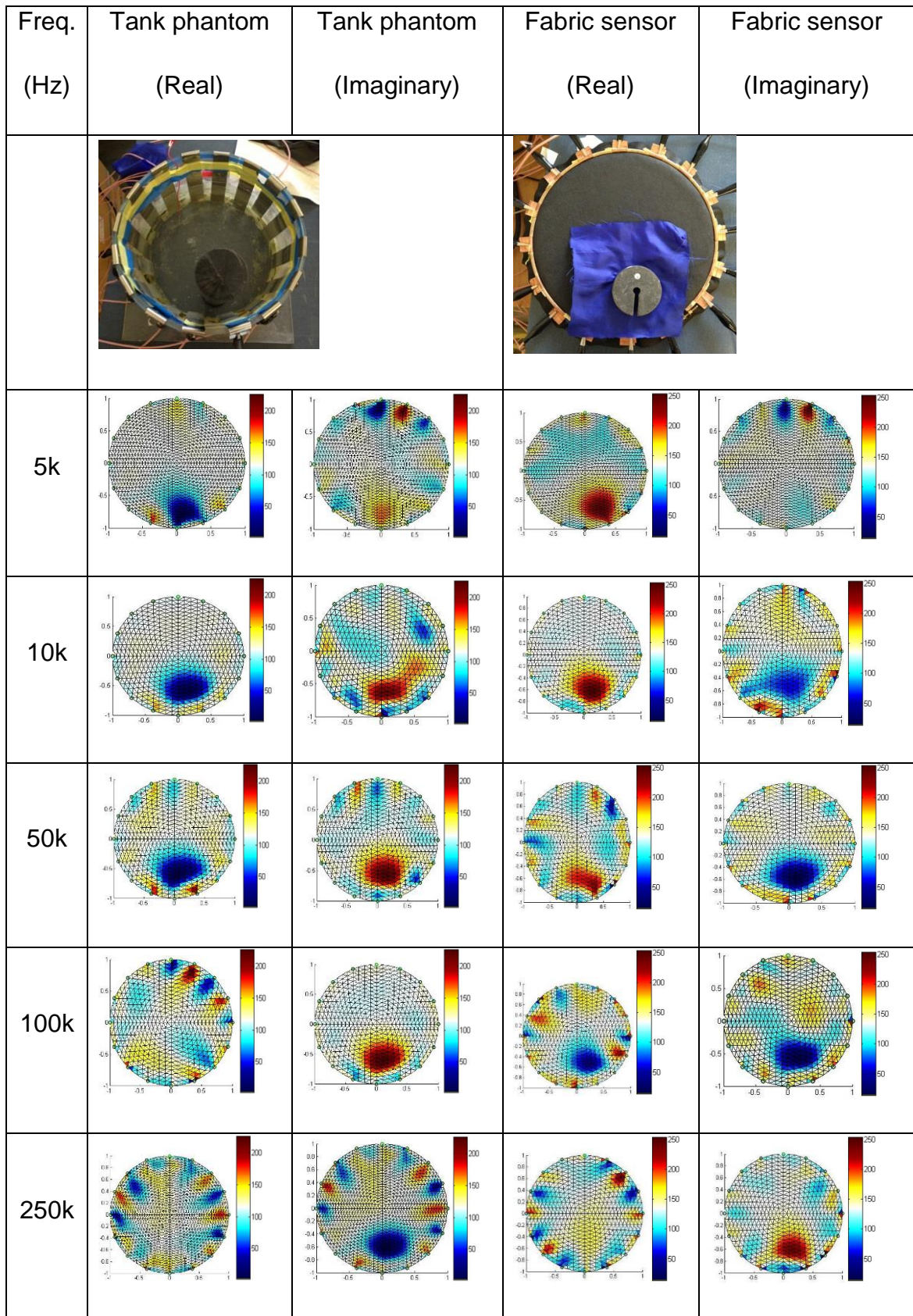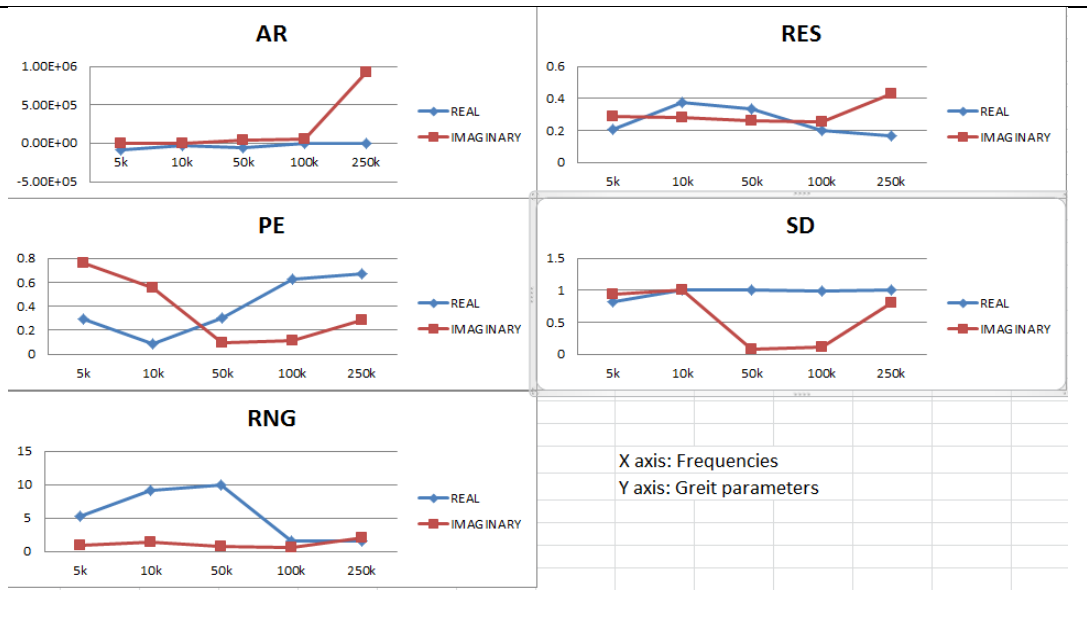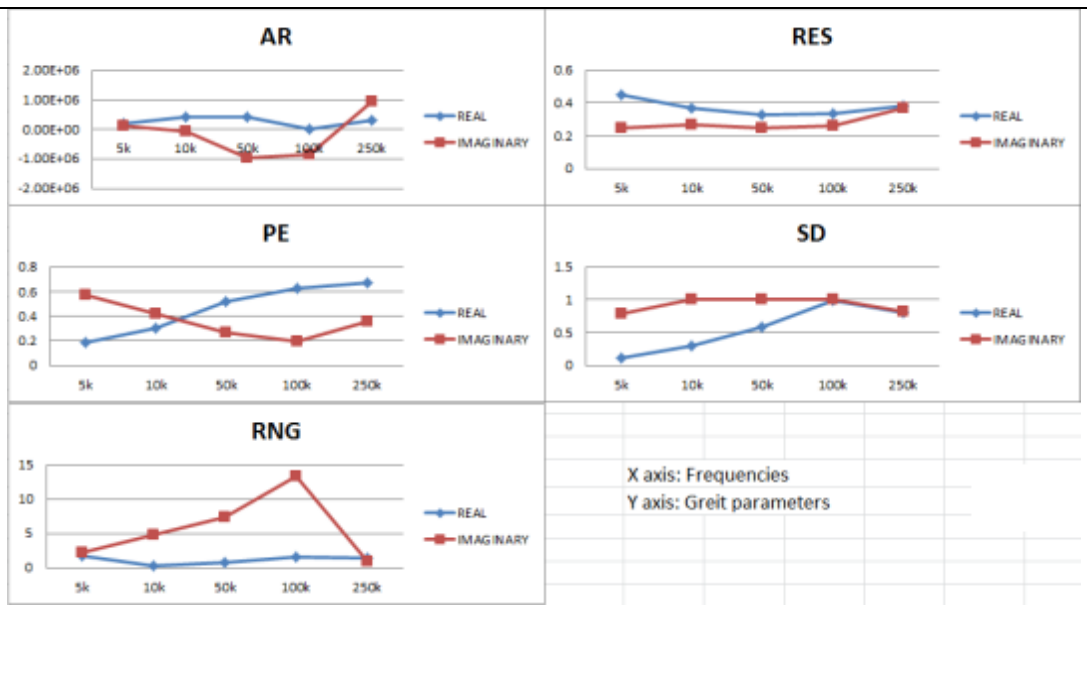
| Freq. (Hz) | Tank phantom (Real) | Tank phantom (Imaginary) | Fabric sensor (Real) | Fabric sensor (Imaginary) |
|---|---|---|---|---|
| |  | |  | |
| 5k |  |  |  |  |
| 10k |  |  |  |  |
| 50k |  |  |  |  |
| 100k |  |  |  |  |
| 250k |  |  |  |  |

*Figure 49: Complex conductivity reconstruction at a multiple frequency range with single pressure point by a side (Test 2)*

Figure 50: Evaluation of GREIT parameters AR, RES, PE, SD, and RNG as a function of point radial position (Test 2)

By observation of the images in Figure 49, both the tank phantom and the fabric pressure mapping sensor have shown similar detectability for the object in different locations. Low distortion and apparent high quality of reconstruction images are produced in all situations. Conductivity distribution of the real part is always useful for typical low frequency EIT systems. However, the real part has failed to provide satisfactory image information at frequencies of 100kHz and 250kHz, while the imaginary part becomes more reliable with higher frequency.

Figure 50 shows the GREIT parameters in the second test. AR measures the image pixel amplitude and therefore the value would be reliant on the image scale. Both real and imaginary part data provide similar AR values except for one strange value that appears in the 250kHz tank test and that may be due to a systematic error. RES has obviously gone up for the imaginary part image in the tank phantom test. In the fabric sensor experiment, real and imaginary part images have significant differences of SD at a frequency of 5kHz. As frequency increases they both reach an SD value of about 0.8. It can be observed that PE for the real part data is increasing dramatically from around 0.2 to 0.6 in both tank and fabric tests. On the contrary, PE for the Imaginary part decreases as operational frequency increases. These facts mean that at higher frequencies such as 100kHz and 250kHz, reconstructed images of imaginary part data locate more accurately to the actual object position.

## 7.5.   Pressure mapping experiments with load and unload tests

A linear image reconstruction algorithm was used for time difference EIT imaging to recover complex impedance information. An electromechanical model needs to be developed to fully model an EIT-based fabric pressure mapping sensor. Further work is needed to establish such forward and inverse modelling. To motive such a study in future, here nonlinear behaviour of the fabric through loading and unloading experiments is investigated. This experiment involved investigating the relationship between measured voltage and applied pressure. It was done by the application of static loads at the side of the fabric. The load was continuously increased and later decreased. The load was initially 1kg and voltage readings were taken. It was then increased to 2kg on the same position, with the corresponding voltage measurements
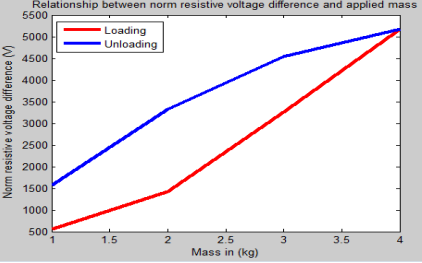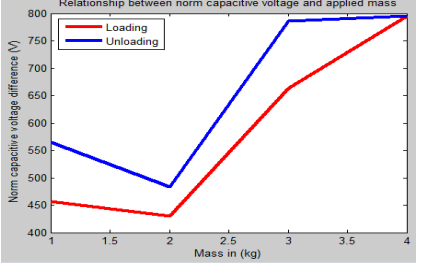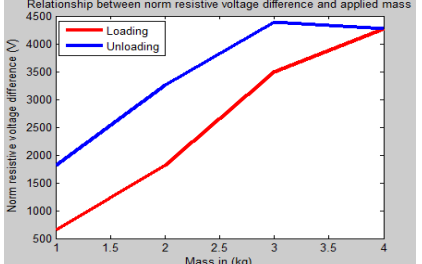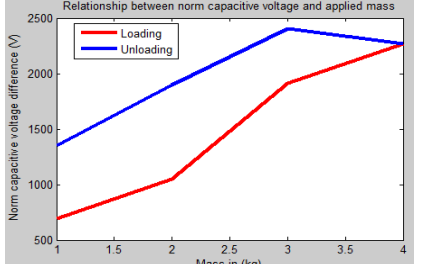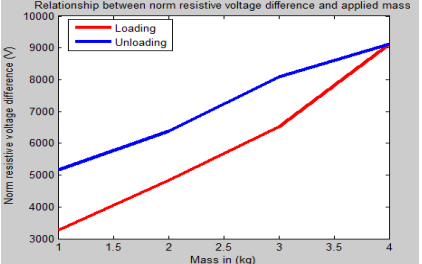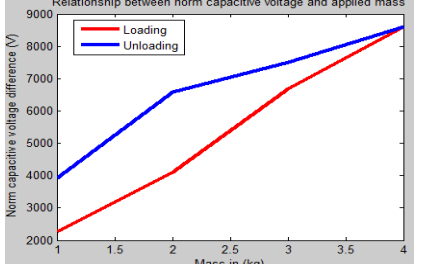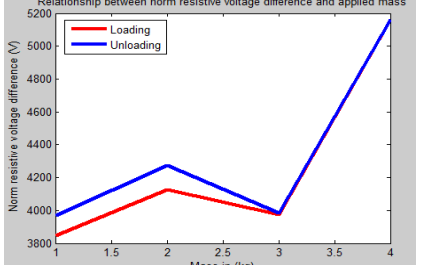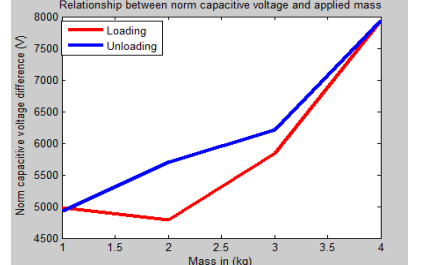
recorded. The procedure was repeated for 3 and 4kg, and for the unloading procedure in steps of 3kg, 2kg and down to 1kg. The voltages measured were analysed to establish a pressure-voltage relationship.

The plots in Figure 51 show the relationship between applied mass and the norm of the voltage difference between the loaded fabric and fabric background (in relaxed mode). The vertical axis gives the norm of the voltages differences, while the horizontal axis gives the applied mass. The norm of voltage differences are calculated separately for real and imaginary parts of the measured voltage. The graphs are used to show the non-linearity in voltage norm for loading and unloading of the same mass. The norm of voltage differences provides a collective measure for nonlinearity of this electromechanical imaging problem. Figure 52 gives a summary of the reconstructed images due to loading and unloading of the fabric patch. Future work should focus on more sophisticated electromechanical modelling, enabling reconstruction of nonlinear behaviour.

For the real part images between 5kHz and 50kHz, the loading voltage norm experiences a non-linear increase with an increase in mass. Consequently, the unloading phase experiences a similar relationship, however with a slight drift in the norm voltage values between loading and unloading. These drifts during unloading can be attributed to the loss in mechanical structure of the already loaded-fabric due to stretch.

Also, for the 10kHz and 50kHz excitation, the non-linearity exhibited by the real image is similar to that of the imaginary image. These frequencies present the best complex impedance results. After 50kHz, the non-linearity in the real part image increases, with the 250kHz frequency having an indescribable voltage-mass relationship for both loading and unloading. For the imaginary part images at 100 and 250kHz, the bias between loading and unloading reduces and resembles that of the real part image obtained at 10 and 50kHz.

Generally, it was established that the offset of the norm voltage between loading and unloading is nearly the same as for the real part images between 10 and 50kHz, as well as for the imaginary part images between 100 and 250kHz.

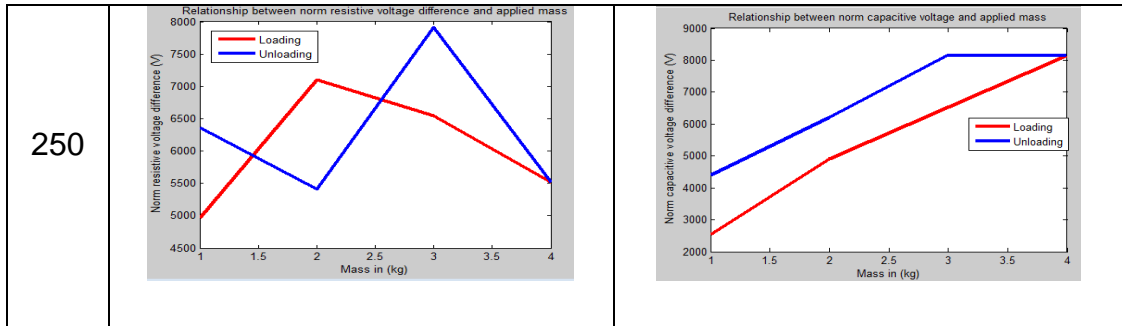| Freq. (kHz) | Conductivity image (Real) loading and unloading cycle | Permittivity image (Imaginary) loading and unloading cycle |
|---|---|---|
| 5 |  |  |
| 10 |  |  |
| 50 |  |  |
| 100 |  |  |
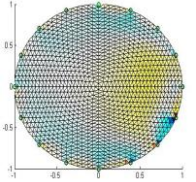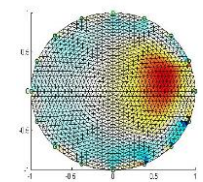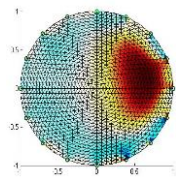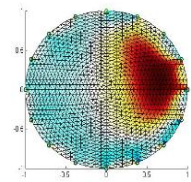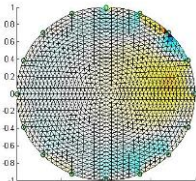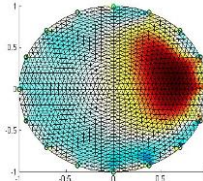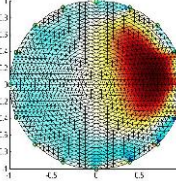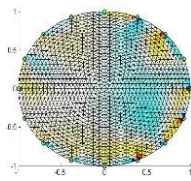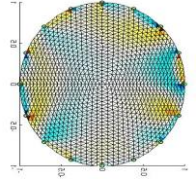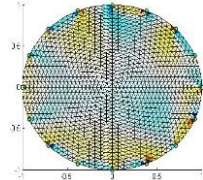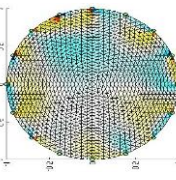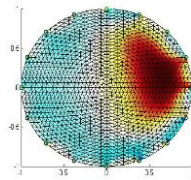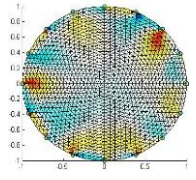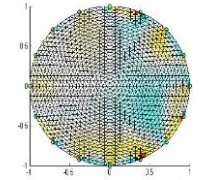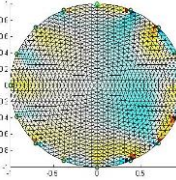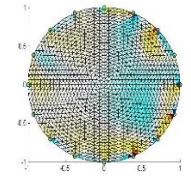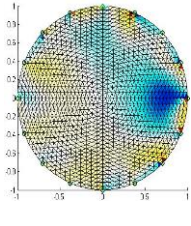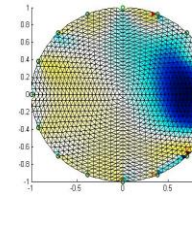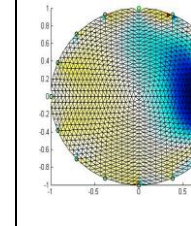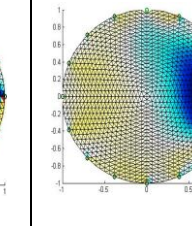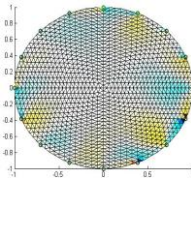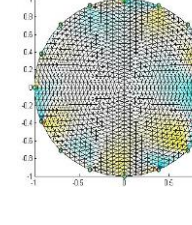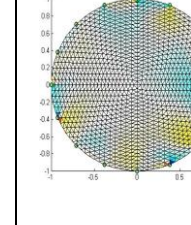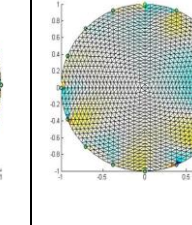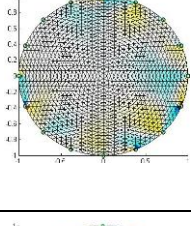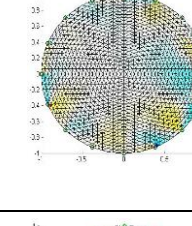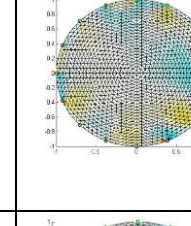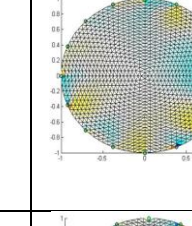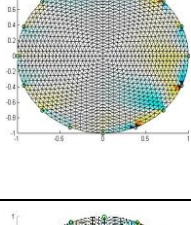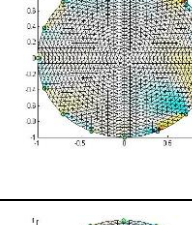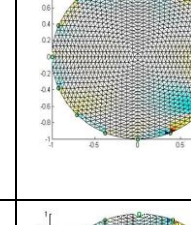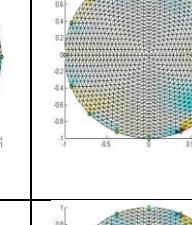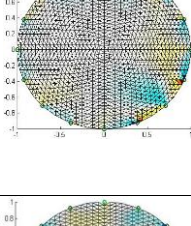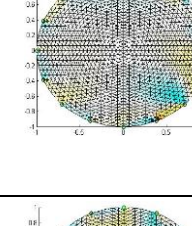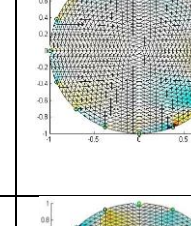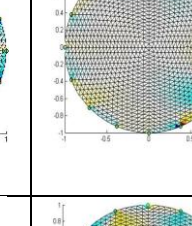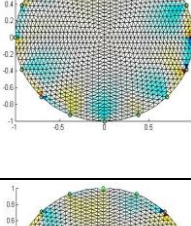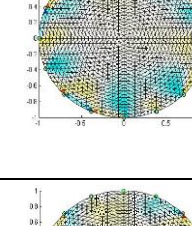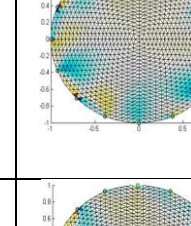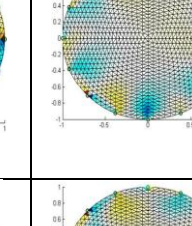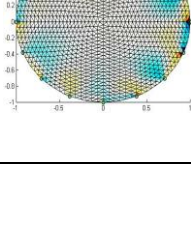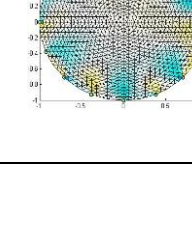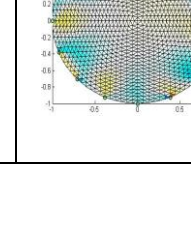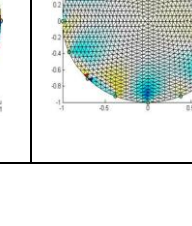
*Figure 51: Nonlinearity and hysteresis during loading and unloading*

| Mass (kg) | | | 1 kg | 2 kg | 3 kg | 4 kg |
|---|---|---|---|---|---|---|
| Freq. (kHz) | | |  |  |  |  |
| 5 | Real | Load |  |  |  |  |
| | | Unload |  |  |  |  |
| | Imaginary | Load |  |  |  |  |
| | | Unload |  |  |  |  |

| | | | | | | |
|---|---|---|---|---|---|---|
| 10 | Real | Load |  |  |  |  |
| | | Unload |  |  |  |  |
| | Imaginary | Load |  |  |  |  |
| | | Unload |  |  |  |  |
| 50 | Real | Load |  |  |  |  |
| | | Unload |  |  |  |  |
| | Imaginary | Load |  |  |  |  |

| 100 | | Unload |  |  |  |  |
|---|---|---|---|---|---|---|
| | Real | Load |  |  |  |  |
| | | Unload |  |  |  |  |
| | Imaginary | Load |  |  |  |  |
| | | Unload |  |  |  |  |
| 250 | Real | Load |  |  |  |  |
| | | Unload |  |  |  |  |

| | | Load |  |  |  |  |
|---|---|---|---|---|---|---|
| | Imaginary | Unload |  |  |  |  |
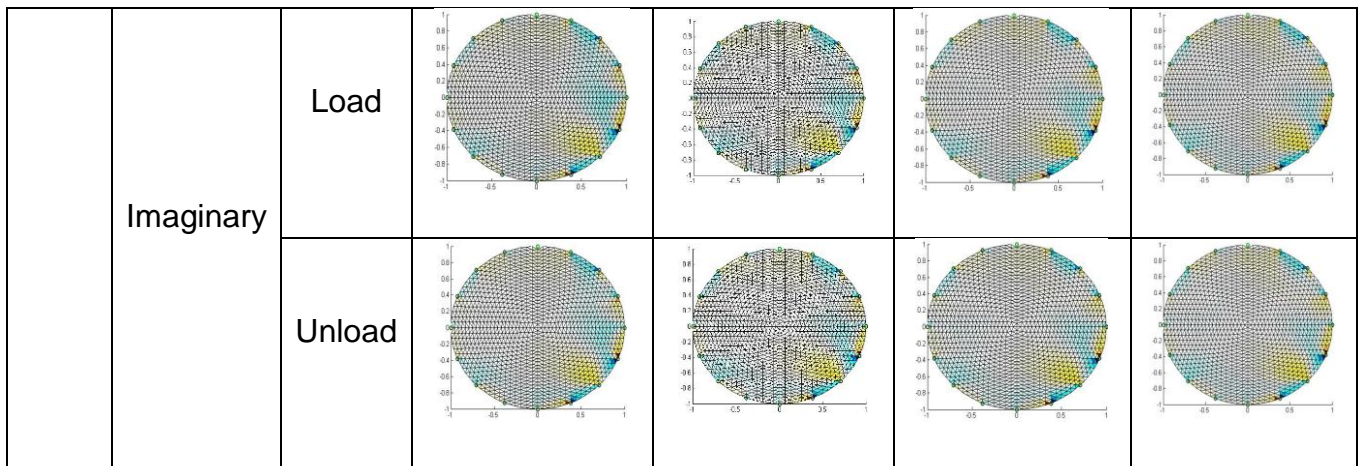
*Figure 52: Reconstructed real and imaginary part images for loading and unloading mode*

## 7.6.   Conclusions

The fabric structure exhibits both resistive and capacitive variations under mechanical loading conditions. For the first time images of capacitive changes due to pressure change were investigated. The imaginary part of conductivity changes becomes more reliable when a higher frequency is applied to the fabric. This means that the capacitive components are useful when fabric sensor tests are performed at high frequencies. Measured voltages for real and imaginary parts are showing hysteresis behaviour, essentially motivating future studies of nonlinear electromechanical behaviour of the fabric pressure mapping sensor. It is important to see that the results show cases when real or imaginary parts may not produce satisfactory results and this is important when evaluating the repeatability and reliability of pressure mapping imaging using complex impedance tomography. The results of the chapter are promising in terms of usefulness of the capacitive component of the complex impedance, in the same way as the resistive component. Future studies will focus on spectral reconstruction, including direct reconstruction of Cole-Cole parameters and frequency difference imaging. Further scientific work is needed to develop future applications of the pressure mapping EIT as a low cost alternative for pressure mapping imaging.

# Chapter.8 Frequency difference EIT

The previous chapter described a detailed study on a multiple frequency complex impedance reconstruction applied to a fabric pressure mapping sensor. While doing multiple frequency reconstruction helped to acquire useful image information of each different system's operating frequency, it is necessary to do extended work to implement an efficient, well-performed frequency difference solver in order to do a further analysis on the spectral behaviour of EIT samples.

This chapter presents a frequency difference EIT (fdEIT) algorithm for possibly lung tumour monitoring. A simulated fdEIT is used to provide tomographic images of lung tumours by assuming that the local area of the tumour is known. Further experimental phantom based tests are carried out to validate the proposed method.

## 8.1. Methods

A patient specific model can be developed using diagnostic CT images that can locate the tumour position. An FEM model of a 16 electrode EIT human chest model is created and a lung image is reconstructed. Figure 53 shows a simulation of lung tumour using a human lung mesh model. Reconstructions are done using adjacent current patterns. Background data includes thorax and two lungs with a tumour in one single frequency; secondary data includes the same tumour but assuming a different frequency response. Reconstruction shows tumour images under fdEIT and LRT assumptions.
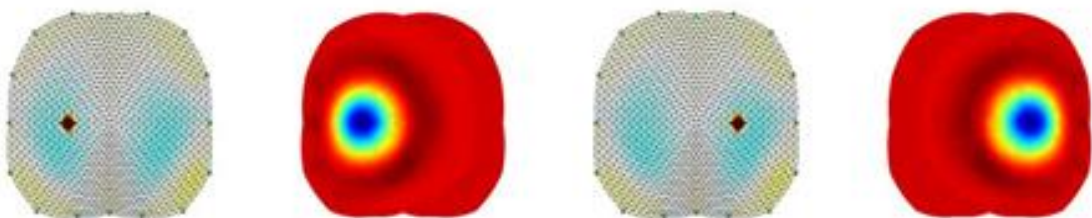


*Figure 53: True images of lung tumour and simulation results of reconstructing tumour in a human lung structure*

A reliable simulation of lung tumour monitoring will require both hardware and software to have a stable performance. Many experiments relating to the EIT imaging technique have been carried out. Based on the literature research, biological samples such as banana, carrot and potato are good materials to simulate an anomaly in an organ of the human body. Therefore, biological samples will be used with saline in this project to simulate a lung tumour monitoring study.

## 8.2. Choice of biological sample and frequencies

The selection of a biological sample to act as an anomaly in the phantom is based on the conductivity spectra with respect to the input frequency.
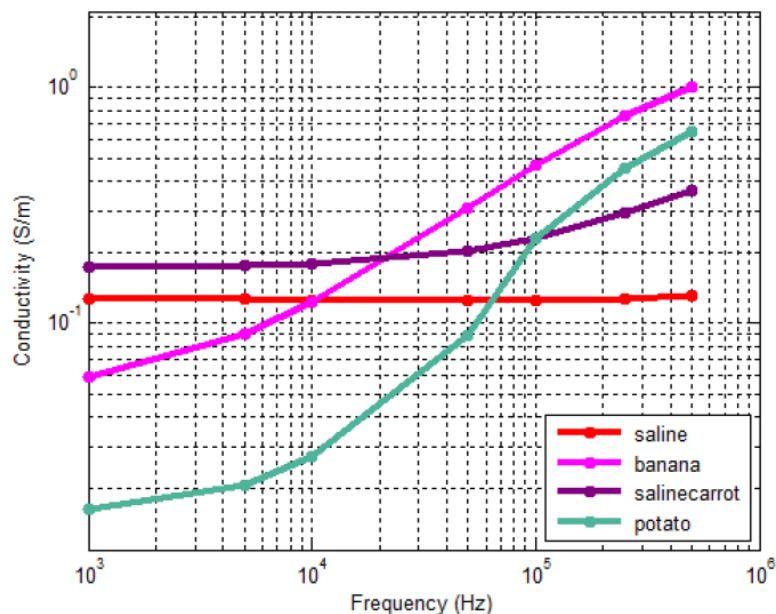


*Figure 54: Conductivity spectra with respect to frequency of saline, banana, carrot and potato*

From Figure 54, it can be seen that the conductivity of saline does not change at all within the frequency range 1kHz to 500kHz. Concerning banana, it has a relatively low conductivity at low frequency compared to saline. When the frequency increases, the conductivity of banana gradually increases and it reaches the same conductivity level as saline at 10kHz frequency and carrot at around 30kHz frequency. It has the highest conductivity at high frequency compared with the other samples in the conductivity spectra.

Looking at the potato, it has the lowest conductivity at low frequency. When the frequency increases, the conductivity of potato would also increase. It has a sharp conductivity difference in the frequency range 10kHz to 100kHz.

The mixture of saline and carrot behaves the same as saline at frequencies less than 100kHz. Then the conductivity of the mixture gradually increases after 100kHz.

Considering the frequency-difference EIT performance, potato and banana should be the best to act as an anomaly in the phantom. This is because both potato and banana have an apparent increment of conductivity when the frequency increases. It also means that the two biological samples have a frequency-dependent change in conductivity, which is known as frequency response. For the conductive region, saline is chosen as the conductivity medium in the phantom. The reason for this is that saline requires a very high frequency to have an effect on its conductivity. Therefore, when performing an fdEIT imaging technique, the measurement of voltage data at different frequencies would only affect the conductivity of the anomaly sample, not the saline background. Saline would be used as the conductivity background in the phantom. All three types of biological sample from the selection would be tested as an anomaly at frequencies of 1, 10 and 50kHz. Despite the fact that at 100kHz frequencies onwards the conductivity difference appeared to be much greater, according to Figure 54, the 100kHz frequency script has been tested numerous times and the boundary data appears to be fuzzy and unstable. Therefore, 50kHz is used instead of 100kHz to perform fdEIT imaging.

## 8.3.  Experimental results
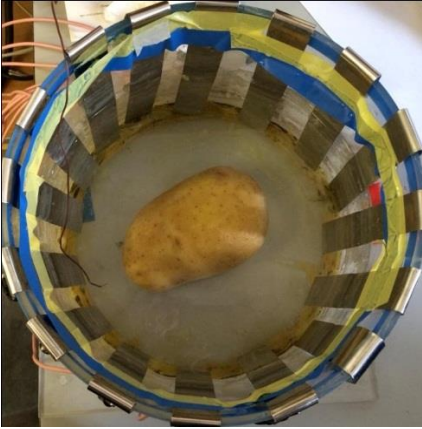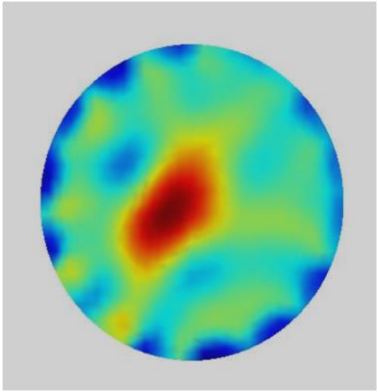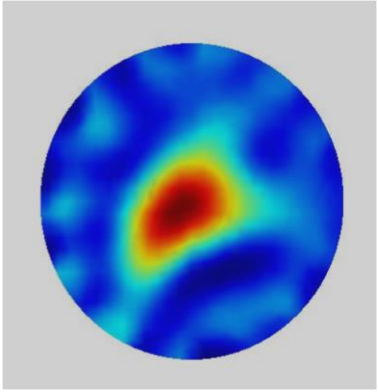
In this section, numerous experimental results are obtained and analysed. In each part of the experiment a different sample is used to simulate an anomaly in the reconstructed image in the phantom study.
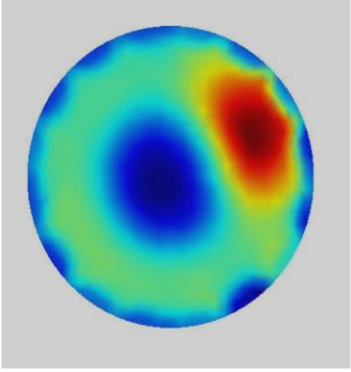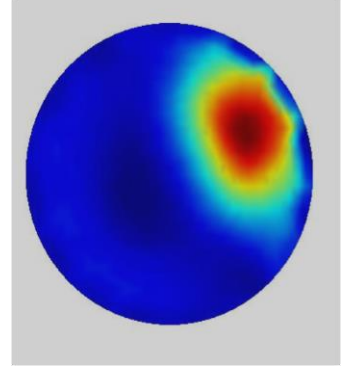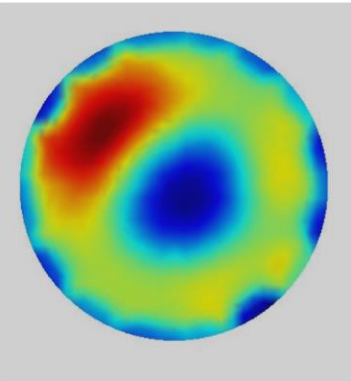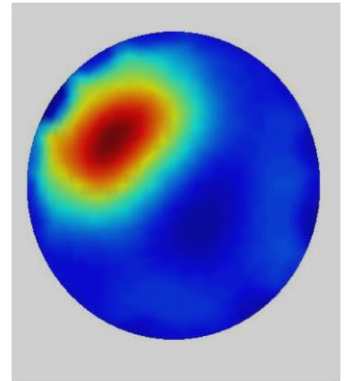
The setup, methodology and instruments used in the following experiments are explained in detailed in the hardware chapter of the thesis.

All of the experimental results regarding an EIT image reconstruction are recorded from a laboratory based phantom filled with saline as a conductive medium.

### 8.3.1. FdEIT image reconstruction of single sample

The first test is to evaluate the performance of this fdEIT programme on a simple large sample and determine the most convincing range of frequencies to acquire the best fdEIT image reconstruction. Results are shown in Figure 55.

| Position of sample | Frequency difference (kHz) | FdEIT image reconstruction |
|---|---|---|
|  A potato in the centre | 1-10 |  |
| | 1-50 |  |

| | | |
|---|---|---|
| <br>A potato by one side | 1-10 |  |
| | 1-50 |  |
| <br>A potato by one side | 1-10 |  |
| | 1-50 |  |

| | |  |
|---|---|---|
|  A carrot by one side | 1-10 | |
| | 1-50 |  |
|  A banana cross the phantom | 1-10 |  |
| | 1-50 |  |
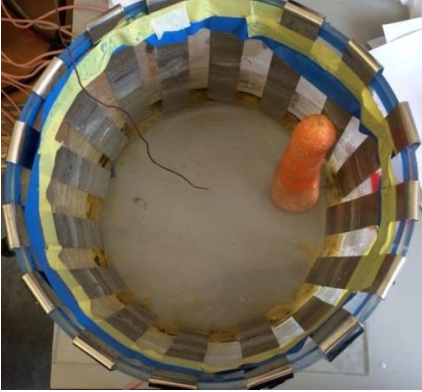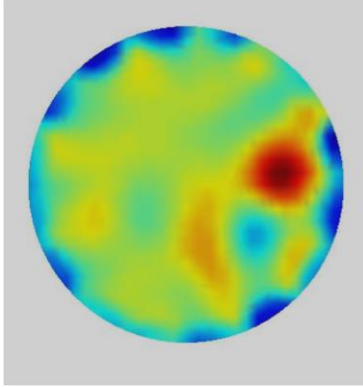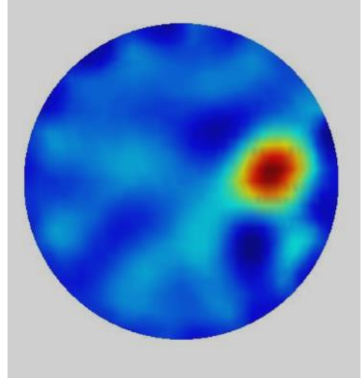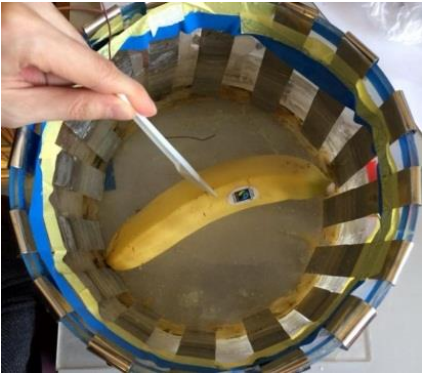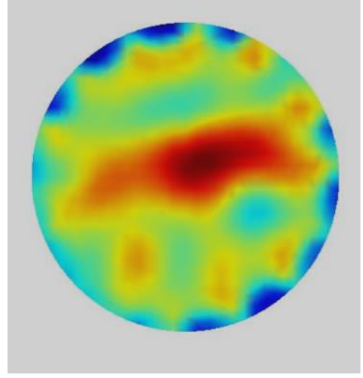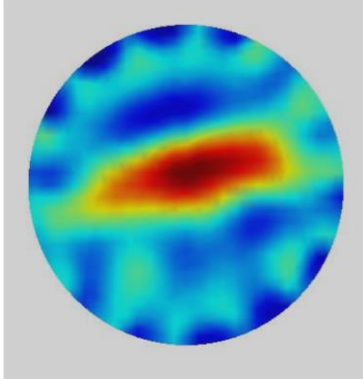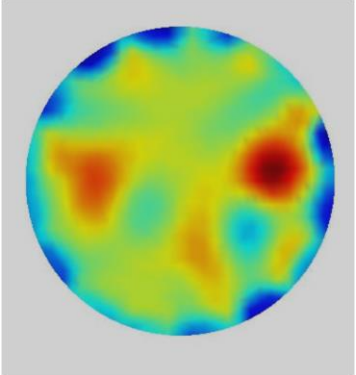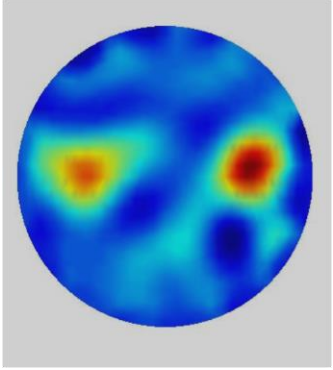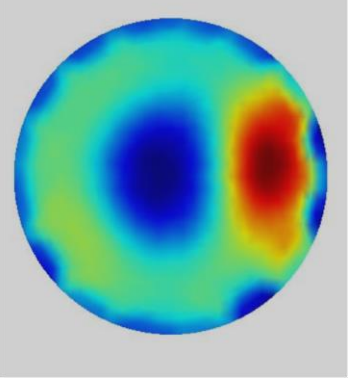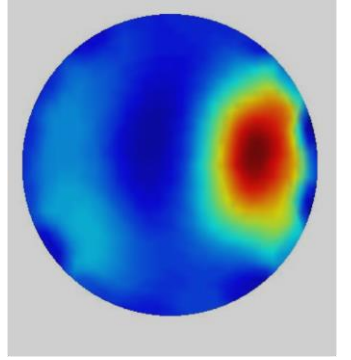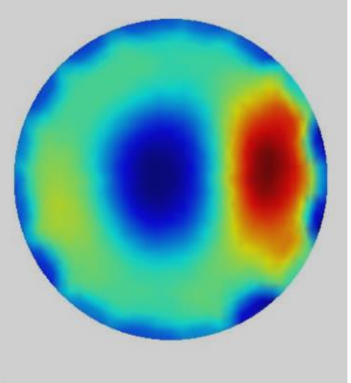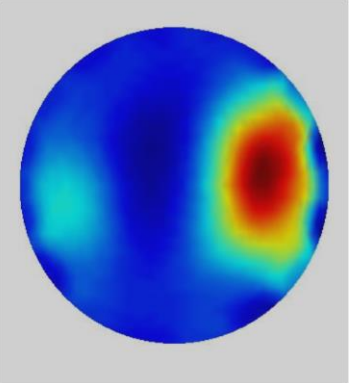
*Figure 55: Simple fdEIT image reconstruction of a single sample*

By comparing the results of frequency difference at 1 and 10kHz with 1 and 50kHz, a distinct difference can be clearly seen in the banana test. With a frequency difference at 1 and 50 kHz, the anomaly was reconstructed in the shape of a banana; whereas at 1 and 10kHz frequency difference the reconstructed images have a less dense anomaly simulated by a banana. It also shows less error due to the background noise of saline at 1 and 50kHz frequency difference.

### 8.3.2. Multiple samples reconstruction

The second experiment shows the image reconstruction of two biological samples placed in the phantom. The two biological samples tested are either of the same type, or a different type, and both situations are demonstrated in this section.

| Position of sample | Frequency difference (kHz) | FdEIT image reconstruction |
|---|---|---|
| Two carrots by sides | 1-10 |  |
| | 1-50 |  |

| | | |
|---|---|---|
|  Carrot and potato laid down | 1-10 |  |
| | 1-50 |  |
|  Carrot and potato by sides | 1-10 |  |
| | 1-50 |  |

| | |  |
|---|---|---|
| <br>Banana on top of potato | 1-10 | |
| | 1-50 |  |
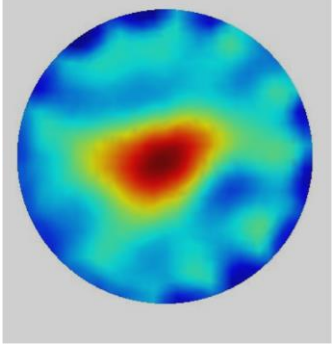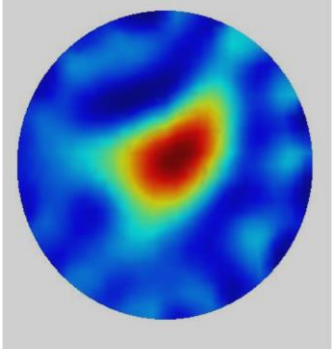
*Figure 56: FdEIT image reconstruction of multiple samples*

For the two carrots case, the reconstructed images have shown both samples correctly. However, there appears to be a significant conductivity contrast between the carrot and potato pair. It can be seen that regardless of the volume contact of the carrot with saline (no matter whether the carrot is standing or laid down in the phantom), the fdEIT image reconstruction could barely show the anomaly represented by a carrot when a potato is in place. The reason for this is due to the conductivity difference of potato and carrot, in which a potato has a higher frequency response than the carrot.

### 8.3.3. Distinguish low conductivity object using static imaging

In this section a set of tests is carried out to show images in a prior knowledge time difference EIT method. The same biological samples are used as in fdEIT images.

The aim of the tests is to show the small carrot sample placed near the potato. Assuming prior knowledge on the background data exists, data are acquired, one with and the other without carrot in one frequency domain. The boundary

data include: voltage measurements from a single potato and voltage measurements from a potato and a carrot.
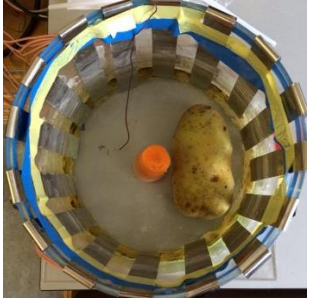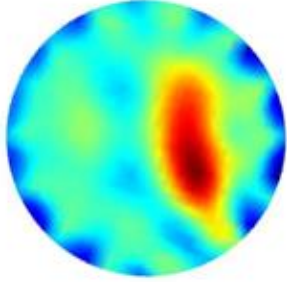
| Data acquisition (position of sample) | FdEIT image reconstruction using 1kHz and 10kHz |
|---|---|
|  |  |

*Figure 56: FdEIT image reconstruction with a piece of carrot and a potato together*

As seen from Figure 56, if only frequency difference reconstruction between 1 and 10kHz is done in this situation, the reconstruction area of potato would completely take over the reconstruction image of carrot. It failed to provide information for the position of carrot and this may due to the high conductivity contrast and large size difference between two objects. Figure 57 is a difference imaging method using two data, one with and one without the carrot piece.
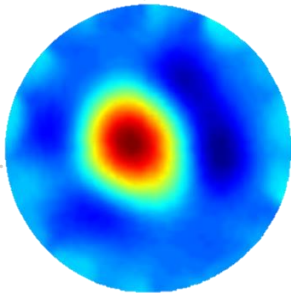
| Data acquisition (position of sample) | Image reconstruction( carrot only) |
|---|---|
|  |  |

*Figure 57: Reconstruction of a small piece of carrot from a high conductivity contrast background*

Figure 57 shows how the background and inclusion data are collected and the final reconstruction image of carrot.

The static imaging technique performs well in this case to provide correct information of the carrot. Localization shows perfectly an image of the carrot within the chosen area. Localization can act as a computational improvement in reducing the pixel size during the reconstruction.

As a result, with the data subtraction method from prior knowledge, a specific conductivity object could always be distinguished from another high conductivity background.

## 8.4.    Conclusions

This chapter proposes a frequency difference EIT technique for imaging of objects for which time difference may not work. Detailed phantom based experimental results are presented. This is a challenging imaging task, and it is hoped that it will take advantage of recent momentum in conventional EIT lung imaging in order to make progress.

# Chapter.9 Conclusion and future works

## 9.1. Conclusion

Electrical impedance tomography is a low-cost, portable and harmless medical imaging method. Being able to image the biological tissues and lesions of the body, this emerging technique has a broad application in the clinical area. Based on the fact that in the living body different tissues under different circumstances will present different conductivities, current is injected and voltages are measured to reconstruct the interior conductivity distribution. There are hundreds of people all over the world studying and trying to improve this technique in order to improve human life.

This thesis has provided a detailed explanation of the research into electrical impedance tomography, and has shown a list of achievements including hardware design and software development.

In EIT, the sensitivity of the measurements to conductivity changes far from the relevant electrodes is small. The values from the sensitivity map would appear to be very small or zero. When the EIT system has large number of electrodes, a large number of measurements and pixels would be included in the calculation. As a result of increasing the density of the sensitivity distribution, the problem might become similar to a CT problem, which would potentially increase the image quality. Limitations appear to the traditional back projection reconstruction algorithm when facing a large scale 3D EIT problem, as a great deal of information needs to be stored and calculation of the Jacobian matrix becomes unfeasible. In Chapter 4, a new reconstruction technique combining the Block-wise conjugate gradient method and sparse matrix simplification is developed to overcome these problems. The new combination reconstruction technique has significant advantages in computational time compared with large scale EIT reconstruction, without significantly decreasing the image quality.

The sparse matrix reduction technique has also shown great potential in the solving of the subsurface EIT imaging problem, as there would be a large number of low sensitivity values far away from the surface area. A subsurface EIT study has been made in Chapter 5 by constructing a plane array EIT sensor and carrying out a series of experimental validations. Simulation has shown promising results while experiments have given satisfactory images. This study will provide valuable information for people who are keen to investigate subsurface imaging in clinical applications.

EIT-based fabric pressure mapping has become a popular area of EIT study in recent years with various potential applications in mind. It can provide major improvements in cost and operation complexity for clinical facilities as the technology is very cheap and simple. Previous fabric pressure mapping sensor studies have shown a range of promising experimental results for different sensor structures. Most EIT experiments measure the resistivity information of the object, as the capacitive component is used in fewer applications. The resistive component can only provide information on the behaviour of the yarn. When the fabric patch has been stretched, the air gaps between yarns will change shape and this will be the capacitive information. If both resistance and capacitance are obtained, the reconstruction image of the fabric might become more accurate and reliable. By making a complex conductivity reconstruction one can obtain real and imaginary data for conductivity, where the permittivity change is mainly indicated by the imaginary part of voltage measurement and is highly related to the capacitive changes in the material. New experiments have been done to indicate the useful information provided by the imaginary part of the conductivity. The imaginary part of conductivity changes becomes more reliable when a higher frequency is applied to the fabric. This means that the capacitive components are useful when fabric sensor tests are performed at high frequencies. The multiple frequency complex reconstruction research gives a promising result in terms of usefulness of the capacitive component of the complex impedance, in the same way as the resistive component.

Because the fabric conductivity changes due to frequency selection, there is motivation to create a frequency difference EIT method to analyse the relationship between frequency and conductivity. Chapter 7 is a comprehensive

section that explained frequency difference EIT and showed the performance of whole range of biological sample tests. By making a reconstruction with prior knowledge of background, an object with specific frequency response can be located and monitored inside a chosen region of interest.

Overall the thesis has made a contribution to designing and fabricating different EIT sensors, as well as showing a new developed EIT programme for large scale EIT problems. It also provides results and analysis of many potential EIT applications, such as planar array EIT and a fabric pressure mapping sensor. Various experimental researches are done to evaluate the algorithm performance and provide valuable information before proceeding to the actual clinical applications. With these achievements and knowledge learned, they are expected to make a contribution to current EIT research and provide a foundation for the upcoming challenges.

## 9.2.   Future work

Enhancing computational improvements of EIT is vital in future EIT studies as the complexity of EIT for hardware and software development is increasing. For example, all of the following will increase the demand of personal computer memory: a large amount of data collection, a more accurate and denser mesh requirement, and non-linear image reconstruction. Sparse matrix reduction and a block-wise parallel reconstruction technique can be further modified and applied to solve other large scale EIT problems in many circumstances. Parallel reconstruction can be upgraded, not only for CPU usage but also GPU usage, which will further enhance the performance of generating meshing and images.

A planar array system is treated as an emerging measuring platform, which has multiple uses in clinical areas. This thesis has studied the fundamentals of planar array EIT and validated the basic sensor performance. Future work will include specific sensor model development, such as a planar array sensor for skin cancer detection, and improving algorithms. With future success in more clinical tests, this technique will make great contributions to long-term disease observation and cancer detection, like the bladder filling examination [38], breast tumour screening and skin cancer detection.

At the current stage of the fabric EIT sensor, only the simplest mathematical model is considered and is assumed to be a linear problem between change in voltage measurement and conductivity. However, the structure of fabric material is complex, and thinking of reconstructing images due to pressure, it is required to calculate and linearise the problem more precisely and in more detail. If a more accurate model can be created in the future, the reconstructed image is expected to be of much better quality. While useful information from the imaginary part of data is successfully extracted in the fabric based sensor research, it is believed that this can help to obtain and better analyse a reconstruction image by doing complex conductivity reconstruction. Frequency difference EIT can be applied to fabric sensors in a future study, and new fabric materials, such as nanoweb fabric [30], are also interesting discoveries. There will also be interest in fabric behaviour in a dynamic situation.

Frequency difference EIT is becoming a popular solution for non-static EIT imaging. In this thesis, fdEIT is tested and proposed to solve clinical EIT problems such as lung tumour detection. There are many other potential applications for which fdEIT can be implemented. In process tomography, there are biological sample applications for which fdEIT can be taken as a solution. The immediate application area would be the food industry.

# List of publications

## Journal papers:

[1] Yang, C., Wei, H., Adler, A. and Soleimani, M. (2013). Reducing computational costs in large scale 3D EIT by using a sparse Jacobian matrix with block-wise CGLS reconstruction. *Physiological measurement*, 34(6), p.645.

[2] Yao, A., Yang, C., Seo, J. and Soleimani, M. (2013). EIT-based fabric pressure sensing. *Computational and mathematical methods in medicine*, 2013. (The first two authors made equal contribution to the paper)

[3] Yang, C., Muhammad, A., Mohamadou, Y., Oh, T. and Soleimani, M. (2015). Complex conductivity reconstruction in multiple frequency electrical impedance tomography for fabric based pressure sensor. *Sensor Review*. Vol 35, No.1, pp 85-97.

## Conference paper:

[4] Yang, C. and Soleimani, M. (2014). Frequency difference electrical impedance tomography for imaging lung tumour. In: International Conference on Translational Research in Radiation Oncology, 1014, Geneva.

[5] Yang, C., Zhang, T., Seo, J. and Soleimani, M. (2014). Localized frequency difference EIT for lung tumour monitoring. In: The 15th International Conference on Biomedical Applications of Electrical Impedance Tomography (EIT 2014), Gananoque, Canada.

[6] Soleimani, M. and Yang, C. (2014). A combined electrical impedance tomography and cone beam CT for radiation therapy monitoring. In: International Conference on Translational Research in Radiation Oncology, Geneva.

[7] Yang, C., Oh, T., Woo, E., Seo, J. and Soleimani, M. (2013). EIT-based fabric pressure sensing using complex conductivity reconstruction. In: XV International Conference on Electrical Bio-Impedance (ICEBI) and the XIV

Conference on Electrical Impedance Tomography 2013 (EIT), 2013-04-22 - 2013-04-24, Heilbad Heiligenstadt.

[8] Yang, C., Adler, A. and Soleimani, M. (2013). Evaluation of 3D planar array EIT (PEIT). In: XV International Conference on Electrical Bio-Impedance (ICEBI) and the XIV Conference on Electrical Impedance Tomography 2013 (EIT), Heilbad Heiligenstadt.

[9] Yang, C., Grychtol, B., Adler, A. and Soleimani, M. (2013). Measuring electrode movement by an external sensor or electrode movement/conductivity reconstruction using EIT data. In: XV International Conference on Electrical Bio-Impedance (ICEBI) and the XIV Conference on Electrical Impedance Tomography 2013 (EIT), Heilbad Heiligenstadt.

[10] Yang, C. and Soleimani, M. (2013). Pressure imaging using EIT on conductive fabric. In: 7th World Congress in Industrial Process Tomography (WCIPT7), Krakow.

[11] Yang, C. and Soleimani, M. (2012). Minimizing computational costs in large scale 3D EIT by using sparse Jacobian matrix and parallel CGLS reconstruction. In: 13th International Conference in Electrical Impedance Tomography (EIT 2012), Tianjin University, Tianjin.

# References

1.  Brown, B.H., *Medical impedance tomography and process impedance tomography: a brief review.* Measurement Science and Technology, 2001. **12**(8): p. 991.

2.  Bayford, R., *Bioimpedance tomography (electrical impedance tomography).* Annu. Rev. Biomed. Eng., 2006. **8**: p. 63-91.

3.  Lionheart, W., N. Polydordes, and A. Borsic, *The reconstruction problem, Part 1 of Electrical Impedance Tomography: Methods, History and Applications,(ed) DS Holder.* Institute of Physics, p3-64, 2004. **20**: p. 1379-1386.

4.  Tawil, D.S., D. Rye, and M. Velonaki, *Interpretation of the modality of touch on an artificial arm covered with an EIT-based sensitive skin.* The International Journal of Robotics Research, 2012. **31**(13): p. 1627-1641.

5.  Geddes, L. and L. Baker, *The specific resistance of biological material—a compendium of data for the biomedical engineer and physiologist.* Medical and biological engineering, 1967. **5**(3): p. 271-293.

6.  Bagshaw, A.P., A.D. Liston, R.H. Bayford, A. Tizzard, A.P. Gibson, A.T. Tidswell, M.K. Sparkes, H. Dehghani, C.D. Binnie, and D.S. Holder, *Electrical impedance tomography of human brain function using reconstruction algorithms based on the finite element method.* NeuroImage, 2003. **20**(2): p. 752-764.

7.  Holder, D.S., *Electrical impedance tomography: methods, history and applications*. 2004: CRC Press.

8.  Henderson, R.P. and J.G. Webster, *An impedance camera for spatially specific measurements of the thorax.* Biomedical Engineering, IEEE Transactions on, 1978(3): p. 250-254.

9.  Plaskowski, A., M. Beck, R. Thorn, and T. Dyakowski, *Imaging industrial flows: Applications of electrical process tomography*. 1995: CRC Press.

10. Webster, J.G., *Electrical impedance tomography*. 1990: Taylor & Francis Group.

11. Bates, R., G. McKinnon, and A. Seagar, *A limitation on systems for imaging electrical conductivity distributions.* Biomedical Engineering, IEEE Transactions on, 1980(7): p. 418-420.

12. Benabid, A., L. Balme, J. Persat, M. Belleville, J. Chirossel, M. Buyle-Bodin, J. de Rougemont, and C. Poupot, *Electrical impedance brain scanner: principles and preliminary results of simulation.* T.-I.-T. journal of life sciences, 1977. **8**(1-2): p. 59-68.

13. Barber, D., B. Brown, and I. Freeston. *Imaging spatial distributions of resistivity using applied potential tomography—APT*. in *Information Processing in Medical Imaging*. 1984. Springer.

14. Barber, D. and B. Brown, *Applied potential tomography.* Journal of physics. E. Scientific instruments, 1984. **17**(9): p. 723-733.

15. Brown, B. and A. Seagar, *The Sheffield data collection system.* Clinical Physics and Physiological Measurement, 1987. **8**(4A): p. 91.

16. Wolf, G.K. and J.H. Arnold, *Noninvasive assessment of lung volume: respiratory inductance plethysmography and electrical impedance tomography.* Critical care medicine, 2005. **33**(3): p. S163-S169.

17. Teschner, E. and M. Imhoff, *Electrical Impedance Tomography: The realization of regional ventilation monitoring. Drager Medical GmbH, 2010*.

18. *ITS: http://www.itoms.com/.*

19. Isaacson, D. and P. Edic. *An algorithm for impedance imaging*. in *Engineering in Medicine and Biology Society, 1992 14th Annual International Conference of the IEEE*. 1992. IEEE.

20. Linderholm, P., L. Marescot, M.H. Loke, and P. Renaud, *Cell culture imaging using microimpedance tomography.* Biomedical Engineering, IEEE Transactions on, 2008. **55**(1): p. 138-146.

21. Haemmerich, D., D.J. Schutt, A.S. Wright, J.G. Webster, and D.M. Mahvi, *Electrical conductivity measurement of excised human metastatic liver tumours before and after thermal ablation.* Physiological measurement, 2009. **30**(5): p. 459.

22. http://www.nanoanalytics.com/en/hardwareproducts/cellzscope/howitworks /chapter03/index.php.

23. Markx, G.H. and C.L. Davey, *The dielectric properties of biological cells at radiofrequencies: applications in biotechnology.* Enzyme and Microbial Technology, 1999. **25**(3): p. 161-171.

24. Skierucha, W., A. Szypłowska, and A. Wilczek, *Aquametry in Agrophysics.* 2013.

25. Bayford, R. and A. Tizzard, *Bioimpedance imaging: an overview of potential clinical applications.* Analyst, 2012. **137**(20): p. 4635-4643.

26. Frerichs, I., J. Hinz, P. Herrmann, G. Weisser, G. Hahn, T. Dudykevych, M. Quintel, and G. Hellige, *Detection of local lung air content by electrical impedance tomography*

*compared with electron beam CT.* Journal of applied physiology, 2002. **93**(2): p. 660-666.

27.     Cherepenin, V., A. Karpov, A. Korjenevsky, V. Kornienko, Y. Kultiasov, A. Mazaletskaya, and D. Mazourov, *Preliminary static EIT images of the thorax in health and disease.* Physiological measurement, 2002. **23**(1): p. 33.

28.     Petrucci, N. and W. Iacovelli, *Lung protective ventilation strategy for the acute respiratory distress syndrome.* The Cochrane Library, 2007.

29.     Adler, A., M.B. Amato, J.H. Arnold, R. Bayford, M. Bodenstein, S.H. Böhm, B.H. Brown, I. Frerichs, O. Stenqvist, and N. Weiler, *Whither lung EIT: Where are we, where do we want to go and what do we need to get there?* Physiological measurement, 2012. **33**(5): p. 679.

30.     Mohamadou, Y., S.J. Lee, Y.E. Kim, T.I. Oh, E.J. Woo, and K.J. Kim, *Nanoweb fabric pressure sensor using complex impedance variation.*

31.     Soulsby, C.R., A; Yerworth, R; Horesh, L; Evans, D; Holder, D, *Extending the range of test meals for EIT of gastric emptying by optimisation of the applied frequency.* Conf. Biomed. Appl. Elec. Impedance Tomography, 6th, London, UK, 2005.

32.     Cherepenin, V., A. Karpov, A. Korjenevsky, V. Kornienko, A. Mazaletskaya, D. Mazourov, and D. Meister, *A 3D electrical impedance tomography (EIT) system for breast cancer detection.* Physiological measurement, 2001. **22**(1): p. 9.

33.     Soni, N.K., A. Hartov, C. Kogel, S.P. Poplack, and K.D. Paulsen, *Multi-frequency electrical impedance tomography of the breast: new clinical results.* Physiological measurement, 2004. **25**(1): p. 301.

34.     Halter, R.J., A. Hartov, and K.D. Paulsen, *A broadband high-frequency electrical impedance tomography system for breast imaging.* Biomedical Engineering, IEEE Transactions on, 2008. **55**(2): p. 650-659.

35.     Cherepenin, V.A., A.Y. Karpov, A.V. Korjenevsky, V.N. Kornienko, Y.S. Kultiasov, M.B. Ochapkin, O.V. Trochanova, and J.D. Meister, *Three-dimensional EIT imaging of breast tissues: system design and clinical testing.* Medical Imaging, IEEE Transactions on, 2002. **21**(6): p. 662-667.

36.     Holder, D.S., *Electrical impedance tomography with cortical or scalp electrodes during global cerebral schaemia in the anaesthetisd rat.* Physiological measurement, 1992. **13**: p. 87-98.

37.     Rao, A., A. Gibson, and D. Holder, *EIT images of electrically induced epileptic activity in anaesthetised rabbits.* Medical and Biological Engineering and Computing, 1997. **35**(1): p. 327.

38.     Holder, D., A. Rao, and Y. Hanquan, *Imaging of physiologically evoked responses by electrical impedance tomography with cortical electrodes in the anaesthetized rabbit.* Physiological measurement, 1996. **17**(4A): p. A179.

39.     Dickin, F. and M. Wang, *Electrical resistance tomography for process applications.* Measurement Science and Technology, 1996. **7**(3): p. 247.

40.     Wang, M., T. Jones, and R. Williams, *Visualization of asymmetric solids distribution in horizontal swirling flows using electrical resistance tomography.* Chemical Engineering Research and Design, 2003. **81**(8): p. 854-861.

41.     George, D., J. Torczynski, K. Shollenberger, T. O'Hern, and S. Ceccio, *Validation of electrical-impedance tomography for measurements of material distribution in two-phase flows.* International Journal of Multiphase Flow, 2000. **26**(4): p. 549-581.

42.     Wang, M., *Inverse solutions for electrical impedance tomography based on conjugate gradients methods.* Measurement Science and Technology, 2002. **13**(1): p. 101.

43.     Cho, K.-H., S. Kim, and Y.-J. Lee, *A fast EIT image reconstruction method for the two-phase flow visualization.* International communications in heat and mass transfer, 1999. **26**(5): p. 637-646.

44.     Knight, R.A. and R.T. Lipczynski. *The Use Of Eit Techniques To Measure Interface Pressure*. in *Engineering in Medicine and Biology Society, 1990., Proceedings of the Twelfth Annual International Conference of the IEEE*. 1990.

45.     Tawil, D.S., D. Rye, and M. Velonaki. *Improved EIT drive patterns for a robotics sensitive skin*. in *Proceeding of Australasian Conference on Robotics and Automation (ACRA)*. 2009. Citeseer.

46.     Kato, Y., T. Mukai, T. Hayakawa, and T. Shibata. *Tactile sensor without wire and sensing element in the tactile region based on EIT method*. in *Sensors, 2007 IEEE*. 2007. IEEE.

47.     Nagakubo, A., H. Alirezaei, and Y. Kuniyoshi. *A deformable and deformation sensitive tactile distribution sensor*. in *Robotics and Biomimetics, 2007. ROBIO 2007. IEEE International Conference on*. 2007. IEEE.

48.     Fulton, W. and R. Lipczynski. *Body-support pressure measurement using electrical impedance tomography*. in *Engineering in Medicine and Biology Society, 1993. Proceedings of the 15th Annual International Conference of the IEEE*. 1993. IEEE.

49.    Alirezaei, H., A. Nagakubo, and Y. Kuniyoshi. *A tactile distribution sensor which enables stable measurement under high and dynamic stretch*. in *3D User Interfaces, 2009. 3DUI 2009. IEEE Symposium on*. 2009. IEEE.

50.    Bertero, M. and P. Boccacci, *Introduction to inverse problems in imaging*. 1998: CRC press.

51.    Metherall, P., D. Barber, R. Smallwood, and B. Brown, *Three dimensional electrical impedance tomography.* Nature, 1996. **380**(6574): p. 509-512.

52.    Vauhkonen, P.J., M. Vauhkonen, T. Savolainen, and J.P. Kaipio, *Three-dimensional electrical impedance tomography based on the complete electrode model.* Biomedical Engineering, IEEE Transactions on, 1999. **46**(9): p. 1150-1160.

53.    Xu, G., H. Wu, S. Yang, S. Liu, Y. Li, Q. Yang, W. Yan, and M. Wang, *3-D electrical impedance tomography forward problem with finite element method.* Magnetics, IEEE Transactions on, 2005. **41**(5): p. 1832-1835.

54.    Brown, B., D. Barber, A. Leathard, L. Lu, W. Wang, R. Smallwood, and A. Wilson, *High frequency EIT data collection and parametric imaging.* Innovation et technologie en biologie et médecine, 1994. **15**: p. 1-8.

55.    Goharian, M., M. Soleimani, A. Jegatheesan, K. Chin, and G.R. Moran, *A DSP based multi-frequency 3D electrical impedance tomography system.* Annals of biomedical engineering, 2008. **36**(9): p. 1594-1603.

56.    Kulkarni, R., G. Boverman, D. Isaacson, G.J. Saulnier, T.-J. Kao, and J.C. Newell, *An analytical layered forward model for breasts in electrical impedance tomography.* Physiological measurement, 2008. **29**(6): p. S27.

57.    Trokhanova, O., M. Okhapkin, and A. Korjenevsky, *Dual-frequency electrical impedance mammography for the diagnosis of non-malignant breast disease.* Physiological measurement, 2008. **29**(6): p. S331.

58.    Romsauerova, A., A. McEwan, L. Horesh, R. Yerworth, R. Bayford, and D.S. Holder, *Multi-frequency electrical impedance tomography (EIT) of the adult human head: initial findings in brain tumours, arteriovenous malformations and chronic stroke, development of an analysis method and calibration.* Physiological measurement, 2006. **27**(5): p. S147.

59.    Jun, S.C., J. Kuen, J. Lee, E.J. Woo, D. Holder, and J.K. Seo, *Frequency-difference EIT (fdEIT) using weighted difference and equivalent homogeneous admittivity: validation by simulation and tank experiment.* Physiological measurement, 2009. **30**(10): p. 1087.

60. Ahn, S., T.I. Oh, S.C. Jun, J. Lee, J.K. Seo, and E.J. Woo. *Weighted frequency-difference EIT measurement of hemisphere phantom*. in *Journal of Physics: Conference Series*. 2010. IOP Publishing.

61. Seo, J.K., J. Lee, S.W. Kim, H. Zribi, and E.J. Woo, *Frequency-difference electrical impedance tomography (fdEIT): algorithm development and feasibility study.* Physiological measurement, 2008. **29**(8): p. 929.

62. Griffiths, H. and A. Ahmed, *A dual-frequency applied potential tomography technique: computer simulations.* Clinical Physics and Physiological Measurement, 1987. **8**(4A): p. 103.

63. Griffiths, H. and A. Ahmed, *Applied potential tomography for non-invasive temperature mapping in hyperthermia.* Clinical Physics and Physiological Measurement, 1987. **8**(4A): p. 147.

64. Griffiths, H. and Z. Zhang, *A dual-frequency electrical impedance tomography system.* Physics in medicine and biology, 1989. **34**(10): p. 1465.

65. Zolgharni, M., P. Ledger, D. Armitage, D. Holder, and H. Griffiths, *Imaging cerebral haemorrhage with magnetic induction tomography: numerical modelling.* Physiological measurement, 2009. **30**(6): p. S187.

66. Romsauerova, A., A. McEwan, L. Fabrizi, and D.S. Holder. *Evaluation of the performance of the Multifrequency Electrical Impedance Tomography (MFEIT) intended for imaging acute stroke*. in *13th International Conference on Electrical Bioimpedance and the 8th Conference on Electrical Impedance Tomography*. 2007. Springer.

67. Gabriel, S., R. Lau, and C. Gabriel, *The dielectric properties of biological tissues: II. Measurements in the frequency range 10 Hz to 20 GHz.* Physics in medicine and biology, 1996. **41**(11): p. 2251.

68. Martinsen, O.G. and S. Grimnes, *Bioimpedance and bioelectricity basics*. 2011: Academic press.

69. Gabriel, C., S. Gabriel, and E. Corthout, *The dielectric properties of biological tissues: I. Literature survey.* Physics in medicine and biology, 1996. **41**(11): p. 2231.

70. Hahn, G., F. Thiel, T. Dudykevych, I. Frerichs, E. Gersing, T. Schröder, C. Hartung, and G. Hellige, *Quantitative Evaluation of the Performance of Different Electrical Tomography Devices-Quantitative Evaluierung der Systemeigenschaften verschiedener Elektrotomographie-Geräte.* Biomedizinische Technik/Biomedical Engineering, 2001. **46**(4): p. 91-95.

71. Adler, A., J. Arnold, R. Bayford, A. Borsic, B. Brown, P. Dixon, T. Faes, I. Frerichs, H. Gagnon, and Y. Garber, *GREIT: towards a consensus EIT algorithm for lung images.* 2008.

72. Vauhkonen, M., W.R. Lionheart, L.M. Heikkinen, P.J. Vauhkonen, and J.P. Kaipio, *A MATLAB package for the EIDORS project to reconstruct two-dimensional EIT images.* Physiological Measurement, 2001. **22**(1): p. 107.

73. Scaife, J., R. Tozer, and I. Freeston, *Conductivity and permittivity images from an induced current electrical impedance tomography system.* IEE Proceedings-Science, Measurement and Technology, 1994. **141**(5): p. 356-362.

74. Schlappa, J., E. Annese, and H. Griffiths, *Systematic errors in multi-frequency EIT.* Physiological measurement, 2000. **21**(1): p. 111.

75. Yerworth, R.J., R. Bayford, B. Brown, P. Milnes, M. Conway, and D.S. Holder, *Electrical impedance tomography spectroscopy (EITS) for human head imaging.* Physiological measurement, 2003. **24**(2): p. 477.

76. Emre, M., *Electrical Impedance Tomography, Meng final year report, department of electrical and electronic engineering, University of Bath.* 2012.

77. Rigaud, B. and J. Morucci, *Bioelectrical impedance techniques in medicine. Part III: Impedance imaging. First section: general concepts and hardware.* Critical reviews in biomedical engineering, 1995. **24**(4-6): p. 467-597.

78. Yanru, W.H.N.G.W. and W. Chao, *EIT Data Acquisition System For Human Body [J].* Chinese Journal of Scientific Instrument, 2001. **4**: p. 023.

79. Oh, T.I., H. Wi, and E.J. Woo, *Electrical Impedance Tomography System for detecting fast physiological signal.* 한국산업응용수학회 학술대회 논문집 (Korean Journal), 2011. **6**(1): p. 35-38.

80. Wi, H., T. Kim, T. Oh, and E. Woo. *Expandable multi-frequency EIT system for clinical applications*. in *Progress In Electromagnetics Research Symposium Proceedings*.

81. *http://www.datasheetarchive.com/tms320lf2812-datasheet.html.*

82. Kim, D., H. Wi, P. Yoo, T. Oh, and E. Woo. *Performance evaluation of KHU Mark2 parallel multi-frequency EIT system*. in *Journal of Physics: Conference Series*. 2010. IOP Publishing.

83. Hua, P., J. Webster, and W. Tompkins, *A regularised electrical impedance tomography reconstruction algorithm.* Clinical Physics and Physiological Measurement, 1988. **9**(4A): p. 137.

84. Wang, Q. and H. Wang. *Image reconstruction based on 11 regularization for electrical impedance tomography (EIT)*. in *Instrumentation and Measurement Technology Conference (I2MTC), 2011 IEEE*. 2011. IEEE.

85. Adler, A., J.H. Arnold, R. Bayford, A. Borsic, B. Brown, P. Dixon, T.J. Faes, I. Frerichs, H. Gagnon, and Y. Gärber, *GREIT: a unified approach to 2D linear EIT reconstruction of lung images.* Physiological measurement, 2009. **30**(6): p. S35.

86. Somersalo, E., M. Cheney, and D. Isaacson, *Existence and uniqueness for electrode models for electric current computed tomography.* SIAM Journal on Applied Mathematics, 1992. **52**(4): p. 1023-1040.

87. Cheney, M., D. Isaacson, and J.C. Newell, *Electrical impedance tomography.* SIAM review, 1999. **41**(1): p. 85-101.

88. Bayford, R., A. Gibson, A. Tizzard, T. Tidswell, and D.S. Holder, *Solving the forward problem in electrical impedance tomography for the human head using IDEAS (integrated design engineering analysis software), a finite element modelling tool.* Physiological measurement, 2001. **22**(1): p. 55.

89. Polydorides, N., *Image reconstruction algorithms for soft-field tomography*. 2002, University of Manchester: UMIST.

90. Borcea, L., *Electrical impedance tomography.* Inverse problems, 2002. **18**(6): p. R99-R136.

91. Aster, R.C., B. Borchers, and C.H. Thurber, *Parameter estimation and inverse problems*. 2013: Academic Press.

92. Hansen, P.C., *Rank-deficient and discrete ill-posed problems: numerical aspects of linear inversion*. Vol. 4. 1998: Siam.

93. *Regularization Methods Inverse Problems in Image Processing. (2014). [ebook]https://[www.math.ethz.ch/education/bachelor/seminars/hs2010/ipip/slides.7.pdf](www.math.ethz.ch/education/bachelor/seminars/hs2010/ipip/slides.7.pdf)*. .

94. Borsic, A., *Regularisation methods for imaging from electrical measurements*. 2002, Oxford Brookes University.

95. Kalman, D., *A singularly valuable decomposition: the SVD of a matrix.* The college mathematics journal, 1996. **27**(1): p. 2-23.

96. David, A., *We recommend a Singular value decomposition. Grand Valley state Universtity. [http://www.ams.org/samplings/feature-column/fcarc-svd](http://www.ams.org/samplings/feature-column/fcarc-svd)*.

97. Griffiths, H., *A phantom for electrical impedance tomography.* Clinical Physics and Physiological Measurement, 1988. **9**(4A): p. 15.

98.     Bera, T.K. and J. Nagaraju. *A FEM-based forward solver for studying the forward problem of electrical impedance tomography (EIT) with a practical biological phantom*. in *Advance Computing Conference, 2009. IACC 2009. IEEE International*. 2009. IEEE.

99.     Boyle, A., A. Borsic, and A. Adler, *Addressing the computational cost of large EIT solutions.* Physiological measurement, 2012. **33**(5): p. 787.

100.    Eames, M.E., B.W. Pogue, P.K. Yalavarthy, and H. Dehghani, *An efficient Jacobian reduction method for diffuse optical image reconstruction.* Optics express, 2007. **15**(24): p. 15908-15919.

101.    Lionheart, W.R., *EIT reconstruction algorithms: pitfalls, challenges and recent developments.* arXiv preprint physics/0310151, 2003.

102.    Kleinermann, F., *Three dimensional modelling of electrical impedance tomography*. 2000, University of Salford.

103.    Dobson, D.C. and F. Santosa, *Resolution and stability analysis of an inverse problem in electrical impedance tomography: dependence on the input current patterns.* SIAM Journal on Applied Mathematics, 1994. **54**(6): p. 1542-1560.

104.    Tang, M., W. Wang, J. Wheeler, M. McCormick, and X. Dong, *The number of electrodes and basis functions in EIT image reconstruction.* Physiological measurement, 2002. **23**(1): p. 129.

105.    Adler, A., R. Youmaran, and W.R. Lionheart, *A measure of the information content of EIT data.* Physiological measurement, 2008. **29**(6): p. S101.

106.    Soleimani, M., O. Dorn, and W.R. Lionheart, *A narrow-band level set method applied to EIT in brain for cryosurgery monitoring.* Biomedical Engineering, IEEE Transactions on, 2006. **53**(11): p. 2257-2264.

107.    Goharian, M., M. Soleimani, and G.R. Moran, *A trust region subproblem for 3D electrical impedance tomography inverse problem using experimental data.* Progress in Electromagnetics Research-PIER, 2009. **94**: p. 19-32.

108.    Shewchuk, J.R., *An introduction to the conjugate gradient method without the agonizing pain*. 1994, Carnegie-Mellon University. Department of Computer Science.

109.    Qiu, W., D. Titley-Péloquin, and M. Soleimani, *Blockwise conjugate gradient methods for image reconstruction in volumetric CT.* Computer methods and programs in biomedicine, 2012. **108**(2): p. 669-678.

110.    Wei, H.-Y. and M. Soleimani, *Three-dimensional magnetic induction tomography imaging using a matrix free Krylov subspace inversion algorithm.* Progress In Electromagnetics Research, 2012. **122**: p. 29-45.

111.  Polydorides, N., W.R. Lionheart, and H. McCann, *Krylov subspace iterative techniques: on the detection of brain activity with electrical impedance tomography.* Medical Imaging, IEEE Transactions on, 2002. **21**(6): p. 596-603.

112.  Saad, Y., *Parallel iterative methods for sparse linear systems.* Studies in Computational Mathematics, 2001. **8**: p. 423-440.

113.  Mueller, J.L., D. Isaacson, and J.C. Newell, *A reconstruction algorithm for electrical impedance tomography data collected on rectangular electrode arrays.* Biomedical Engineering, IEEE Transactions on, 1999. **46**(11): p. 1379-1386.

114.  Yan, W. and S. Hong, *Breast Measurement of EIT with a Planar Electrode Array*, in *Recent Advances in Computer Science and Information Engineering*. 2012, Springer. p. 769-774.

115.  Aristovich, K.Y., G.S. dos Santos, B.C. Packham, and D.S. Holder, *A method for reconstructing tomographic images of evoked neural activity with electrical impedance tomography using intracranial planar arrays.* Physiological measurement, 2014. **35**(6): p. 1095.

116.  Zhang, X.-J., M.-Y. Chen, W. He, and C.-H. He, *Modeling and simulation of open electrical impedance tomography.* International Journal of Applied Electromagnetics and Mechanics, 2010. **33**(1): p. 713-720.

117.  Tizzard, A., L. Horesh, R.J. Yerworth, D.S. Holder, and R. Bayford, *Generating accurate finite element meshes for the forward model of the human head in EIT.* Physiological measurement, 2005. **26**(2): p. S251.

118.  Zhang, M., L. Ma, Z. Ye, C. Yang, H. Wei, R. Banasiak, and M. Soleimani. *Near subsurface 3D imaging using planar array: EIT, ECT, MIT*. in *7th World Congress in Industrial Process Tomography (WCIPT7)*. 2013. University of Bath.

119.  Kao, T.-J., J. Newell, G. Saulnier, and D. Isaacson, *Distinguishability of inhomogeneities using planar electrode arrays and different patterns of applied excitation.* Physiological measurement, 2003. **24**(2): p. 403.

120.  Ma, L., H.-Y. Wei, and M. Soleimani, *Planar magnetic induction tomography for 3D near subsurface imaging.* Progress In Electromagnetics Research, 2013. **138**: p. 65-82.

121.  Pudney, C., M. Robins, B. Robbins, and P. Kovesi, *Surface detection in 3 D confocal microscope images via local energy and ridge tracing.* Journal of Computer-Assisted Microscopy, 1996. **8**(1): p. 5-20.

122.  Oh, T.I., H. Koo, K.H. Lee, S.M. Kim, J. Lee, S.W. Kim, J.K. Seo, and E.J. Woo, *Validation of a multi-frequency electrical impedance tomography (mfEIT) system KHU Mark1:*

*impedance spectroscopy and time-difference imaging.* Physiological measurement, 2008. **29**(3): p. 295.

123.    Bujnowski, A. and J. Wtorek. *An excitation in differential EIT–selection of measurement frequencies*. in *13th International Conference on Electrical Bioimpedance and the 8th Conference on Electrical Impedance Tomography*. 2007. Springer.

124.    Edlich, R., K.L. Winters, C.R. Woodard, R.M. Buschbacher, W.B. Long III, J.H. Gebhart, and E.K. Ma, *Pressure ulcer prevention.* Journal of long-term effects of medical implants, 2004. **14**(4).

125.    Reddy, M., S.S. Gill, and P.A. Rochon, *Preventing pressure ulcers: a systematic review.* Jama, 2006. **296**(8): p. 974-984.

126.    Tawil, D.S., D. Rye, and M. Velonaki, *Improved image reconstruction for an EIT-based sensitive skin with multiple internal electrodes.* Robotics, IEEE Transactions on, 2011. **27**(3): p. 425-435.

127.    Loh, K.J., T.-C. Hou, J.P. Lynch, and N.A. Kotov, *Carbon nanotube sensing skins for spatial strain and impact damage identification.* Journal of Nondestructive Evaluation, 2009. **28**(1): p. 9-25.

128.    Tawil, D.S., D. Rye, and M. Velonaki. *Touch modality interpretation for an EIT-based sensitive skin*. in *Robotics and Automation (ICRA), 2011 IEEE International Conference on*. 2011. IEEE.

129.    Yao, A. and M. Soleimani, *A pressure mapping imaging device based on electrical impedance tomography of conductive fabrics.* Sensor Review, 2012. **32**(4): p. 310-317.

130.    Yao, A., C.L. Yang, J.K. Seo, and M. Soleimani, *EIT-based fabric pressure sensing.* Computational and mathematical methods in medicine, 2013. **2013**.

131.    Elsanadedy, A., Y. Mamatjan, M. Ahmadi, and A. Adler. *Characterisation of conductive polymer for EIT based sensor*. in *Proceedings of the International Conference on Electrical and Computer Systems (ICECS'12)*. 2012.

132.    Oh, T.I., H. Wi, D.Y. Kim, P.J. Yoo, and E.J. Woo, *A fully parallel multi-frequency EIT system with flexible electrode configuration: KHU Mark2.* Physiological measurement, 2011. **32**(7): p. 835.

133.    *NW170-SL-PA-1500, Eeontex Conductive Nonwoven Fabric, Eeonyx Corporation, 2009.*